Mississippi State University

Scholars Junction

Theses and Dissertations Theses and Dissertations

8-6-2021

Optical probing of spatial structural abnormalities in cells/tissues due to cancer, drug-effect, and brain abnormalities using mesoscopic physics-based spectroscopic techniques

Prakash Adhikari
prakashadhikari9706@gmail.com

Follow this and additional works at: https://scholarsjunction.msstate.edu/td

Recommended Citation

Adhikari, Prakash, "Optical probing of spatial structural abnormalities in cells/tissues due to cancer, drug-effect, and brain abnormalities using mesoscopic physics-based spectroscopic techniques" (2021). *Theses and Dissertations*. 5259.
https://scholarsjunction.msstate.edu/td/5259

This Dissertation - Open Access is brought to you for free and open access by the Theses and Dissertations at Scholars Junction. It has been accepted for inclusion in Theses and Dissertations by an authorized administrator of Scholars Junction. For more information, please contact scholcomm@msstate.libanswers.com.

Optical probing of spatial structural abnormalities in cells/tissues due to cancer, drug-effect, and brain abnormalities using mesoscopic physics-based spectroscopic techniques

By

Prakash Adhikari

Approved by:

Prabhakar Pradhan (Major Professor)
Chuji Wang (Committee Member)
Yaroslav Koshka (Committee Member)
Gombojav O. Ariunbold (Committee Member)
Henk F. Arnoldus (Committee Member/Graduate Coordinator)
Jason M. Keith (Dean, Bagley College of Engineering)

A Dissertation
Submitted to the Faculty of
Mississippi State University
in Partial Fulfillment of the Requirements
for the Degree of Doctor of Philosophy
in Applied Physics
in the Department of Physics and Astronomy

Mississippi State, Mississippi

August 2021

Copyright by

Prakash Adhikari

2021

Name: Prakash Adhikari

Date of Degree: August 6, 2021

Institution: Mississippi State University

Major Field: Applied Physics

Major Professor: Prabhakar Pradhan

Title of Study: Optical probing of spatial structural abnormalities in cells/tissues due to cancer, drug-effect, and brain abnormalities using mesoscopic physics-based spectroscopic techniques

Pages in Study: 128

Candidate for Degree of Doctor of Philosophy

The quantitative measurement of structural alterations at the nanoscale level is important for understanding the physical states of weakly disordered optical mediums such as cells/tissues. Progress in certain diseases, such as cancer or abnormalities in the brain, is associated with the nanoscale structural alterations at basic building blocks of the cells/tissues. Elastic light scattering, especially at visible wavelengths range provides non-invasive ways to probe the cells/tissues up to nanoscale level. Therefore, a mesoscopic physics-based open light scattering technique with added finer focusing, partial wave spectroscopy (PWS), is developed to probe nanoscale changes. Then, molecular-specific light localization technique, a close scattering approach called inverse participation ratio (IPR) is proposed that is sensitive to nano to microstructural cell/tissue alterations.

In this dissertation, we have introduced the further engineered PWS system with the finer focus for precise volume scattering and molecular-specific light localization IPR techniques. As an application of PWS, we first probe precise scattering volume in commercially available tissue microarrays (TMA) tissue samples to standardize the existing cancer diagnostic methods by distinguishing the cancer stages. We also apply the PWS technique to probe chemotherapy drug-treated metastasizing cancer patients by xenografting prostate cancer cells using a mouse model and identify drug-sensitive and drug-resistance treatment cases. On the other hand, as an illustration of another mesoscopic physics-based molecular specific light localization technique, Confocal-IPR, we study the effects of a probiotic on chronic alcoholic mice brains by targeting the molecular specific alteration in glial cells, astrocytes and microglia, and chromatin of the brain cells through staining with appropriate dyes/proteins. Using structural disorder of IPR as a biomarker, the results show that probiotics in the presence of alcohol are beneficial and help overall brain health. Finally, a TEM-IPR study was performed using nanoscale resolution TEM imaging to support the optical IPR method by studying the anti-cancerous drug effect in ovarian cancer cells. The result shows that we can quantitatively measure the effect of anti-cancerous drugs in cancer treatment and the level of tumorigenicity far below the diffraction limit, and it has a similar effect and supports the optical IPR method.

DEDICATION

To the living gods (parents),

Purushottam Adhiakri and *Saradha Devi Adhikari*

Whose blessings and encouragements have strengthened me every step of my life.

(मातृ देवो भवः! पितृ देवो भवः! आचार्य देवो भवः!)

To my wife

Sudha Neupane

For all her love, care, sacrifices, and support

ACKNOWLEDGEMENTS

I would like to express my gratitude and deepest appreciation to my adviser Dr. Prabhakar Pradhan, Department of Physics and Astronomy, MSU for paving my research pathway in Bionanophotonics. I am very much thankful for his persistent guidance and valuable advice to pursue my doctoral degree. Without his guidance and motivations, this degree would not have been accomplished.

I would like to thank Dr. Henk F. Arnoldus, Dr. Chuji Wang, Dr. Gombojav O. Ariunbold, and Dr. Yaroslav Koshka for being on my PhD committee despite their busy schedules. I would also like to acknowledge all the professors, colleagues, and staff of the Department of Physics and Astronomy, MSU who supported my research ventures. Special thanks to Dr. Radhakrishna Rao, and Dr. Pradeep Shukla from the University of Tennessee Health Science Centre (UTHSC) and Dr. Muralli M. Yallapu, and Dr. Prashanth K. B. Nagesh from the University of Texas-Rio Grande Valley (UTRGV) for their collaboration and preparing biological samples for spectroscopic study. Also, I must acknowledge Dr. Debarshi Roy for his collaboration on the TEM study of the anti-cancerous drug-treated cancer project.

I am also thankful to the staff of the Department of Physics and Astronomy for their assistance in various projects. Especial thanks to Mr. Ben Ardhal for his continuous support in the lab setup and moving lab equipment in the establishment of the Bionanophotonics laboratory. I am always grateful to Ms. Susan Galloway and Jo Mckenzie for their administrative assistance.

I am also thankful to our Physics Laboratory Coordinator Mr. Chase Boone for his help and support in the machine shop, and design.

I would like to remember all our lab members of the Bionanophotonics laboratory, MSU for their continuous effort and help in running my experiments. Especially I would like to thank Fatimah Alharthi, Liam Elkinton, Shrisendu Nanda, and Mehedi Hasan for their continuous support in conducting my research experiments and fruitful discussion.

Lastly, I must express my profound gratitude to my family, friends, and relatives for their unfailing supports and continuous encouragement and motivation throughout my life. I am immensely grateful to my wife Sudha Neupane and son Sabda Adhikari for their all love, sacrifice, and support throughout this journey. This accomplishment would not have been possible without these beautiful people in my life.

TABLE OF CONTENTS

CHAPTER

APPENDIX

LIST OF FIGURES

ABBREVIATIONS AND UNITS

ABBREVIATIONS

PWS	Partial Wave Spectroscopy
IPR	Inverse Participation Ratio
TEM	Transmission Electron Microscopy
SEM	Scanning Electron Microscopy
H	Hamiltonian
ECM	Extra Cellular Matrix
LCTF	Liquid Crystal Tunable Filter
TMA	Tissue Microarrays
CNS	Central Nervous System
CCD	Charge Couple Device
OC	Ovarian Cancer
PC	Prostate Cancer
BC	Breast Cancer
CC	Colon Cancer
ACS	American Cancer Society
NIST	National Institute of Standards and Technology

NA	Numerical Aperture
rms	Root Mean Square
1D	One Dimensional
2D	Two Dimensional
3D	Three Dimensional
L_d	Structural Disorder
Std	Standard Deviation
Xe	Xenon lamp

UNITS

cm	centimeter
mm	millimeter
mm^3	millimeter cube
μm	micrometer
μm^2	micrometer square
μg	microgram
nm	nanometer
ml	milliliter
A^0	Armstrong
W	watt
mM	millimole
^0C	degree Celsius
KeV	kilo electron volt
cfu	colony-forming unit

CHAPTER I

INTRODUCTION: MESOSCOPIC PHYSICS BASED SPECTROSCOPIC SYSTEMS

Optical probing of tissue microarchitecture and cell nanoarchitecture could provide tremendous information which is important for both diagnostic and therapeutic purposes especially for deadly diseases like cancer. This is because the structural alterations are associated with the progress of these diseases that result in the rearrangement of the basic macromolecules in cells/tissues. With the progress of time, different biomedical optical techniques such as optical coherence tomography (OCT), Mie scattering, fluorescence spectroscopy, diffusion spectroscopy, Raman spectroscopy, elastic light scattering spectroscopy, etc. are in use and have shown promising success to probe weakly disordered optical medium such as cells/tissue architectural properties, to study/quantify abnormalities by probing the structural alterations [1–10]. Among these techniques, elastic light scattering spectroscopy provides a non-invasive, prompt, and cost-effective tool that is sensitive enough to probe the cells/tissues structures. The photons scattered from any structure exhibits characteristics patterns based on scattering angle and wavelength to provide the signature properties of scatter’s shape, size, density, refractive index, etc. However, all these scattering methods: OCT, Mie scattering, fluorescence spectroscopy, diffusion spectroscopy are based on the bulk spatial structural changes in cells/tissues. Now, it is shown that probing the fluctuating part of the cells/tissues will provide more sensitive information of the physical state of the system relative to the bulk changes.

Furthermore, the existing literature showed that the elastic back-scattering signal is extensively sensitive to the refractive index fluctuations and their alterations [11]. Based on this sensitivity of the back-scattering light, we can probe the tissue nano to microarchitectures in a wide range of scales [3,5,12–14]. In the conventional elastic scattering experiments, before the light exits tissue samples, it undergoes multiple scattering resulting in decreased sensitivity to probe nanoscale cells/tissue architecture. At the same time, it is shown that progression of cancer or any other abnormalities results in nano to submicron scale structural alterations in cells/tissues due to the rearrangement of macromolecules [15–18]. However, the sensitivity of existing light scattering techniques to probe refractive index fluctuations reduces significantly when the size of the scattering structure falls below the scattering light wavelength (~500nm). The resolution of conventional microscopy is ranged around 0.5μm which is way below the size of macromolecules [11]. On the other hand, confocal microscopy and single-molecule localization microscopy which are sensitive up to 200nm to 10nm are highly dyed dependent. Likewise, we can probe samples up to 1 A^0 or a fraction of nm using a transmission electron microscope (TEM) which requires complicated sample preparation and has huge and expensive setups. Since the measurement of sub-wavelength refractive index fluctuation discloses the tremendous information useful in diagnosis and therapies and has a significant interest in recent days. Here, we apply mesoscopic light transport theory [19–21]. Using this, we can probe change in the refractive index fluctuations of any length scale below the wavelength within the diffraction limit if: (i) the object is weakly disordered and scattering medium, and (ii) analyze the multiple interferences of 1D reflected signal within the object [15,16]. Therefore, we combine mesoscopic physics with imaging techniques in order to increase the sensitivity of the existing imaging technique and probe change in the refractive index fluctuations that happen at a nanometer length scale.

In this dissertation, we have applied two different mesoscopic physics-based elastic scattering techniques: (i) partial wave spectroscopy (PWS)-an open scattering approach and (ii) inverse participation ratio (IPR)-a closed scattering approach. These techniques are capable of probing changes in cells/tissue nano to microarchitecture and quantifies the statistical properties of nanoscale refractive index fluctuations [15–17,22,23]. The recently developed and further engineering added finer focusing PWS can probe precise scattering volume in tissue and sensitive enough to detect the microarchitecture in tissue microarrays (TMA) and anti-cancerous drug-treated xenografted tumors. And, molecular specific light localization technique, IPR, using transmission electron microscopy (TEM) and confocal images enables us to detect of nano to submicron scales structural alterations in cell and their components to quantify cancer, drug-effect in cancer treatment, and probiotic effect in the treatment of alcoholic's brain.

In this introductory section, we will describe the instrumentation and mesoscopic formulations for the PWS and IPR techniques. Then we will describe the samples that we have probed using these techniques. Furthermore, to support the optical experiments, we have also performed experiments using nanoscale sensitive TEM imaging, describe in short.

1.1 Partial wave spectroscopy (PWS) optical technique

Elastic light scattering spectroscopy is a very powerful and commonly used technique to probe cells/tissue architecture [5,10]. The spatial variation of the concentration of intracellular components in cells such as DNA, RNA, lipids, etc. due to diseases or cancer results in changes in mass density fluctuations, in turn, spatial refractive index fluctuations. However, the size of these macromolecular components falls below the diffraction limit of the existing optical imaging technique which is 200nm. Therefore, in partial wave spectroscopy (PWS) we combine mesoscopic physics with the imaging technique to probe the spatial refractive index fluctuations in the weakly disordered medium, within the diffraction limit. PWS technique records 1D backscattered signal in the far-field from cells/tissues and quantifies the refractive index fluctuations at sub-diffraction length scale. According to the mesoscopic light transport theory [19,20,24–26], the 1D reflected signal is the multiple references of light waves reflected from reflective index fluctuations, which is non-self-averaging for all length scales in a weak refractive index fluctuation [24–27]. And the importance of a non-self-averaging system is the standard deviation and mean of a relative parameter increases with the increase in system size, with full interference prominence. That means the reflected signal is sensitive to refractive index fluctuations at any length scale even below the wavelength range [28–31]. This, therefore, provides an opportunity to probe cell nanoarchitecture by characterizing 1D backscattered light wave which is the most sensitive way. The experimental setup and theoretical details of the PWS setup are explained below.

1.1.1 Partial wave spectroscopy (PWS) instrumentation

The developed finer focusing experimental setup for the partial wave spectroscopy system in the Bionanophotonics laboratory in the Department of Physics and Astronomy at MSU is as shown in fig. 1.1. A spatially low coherence broadband white light source (Xenon lamp, 150W, Newport) is used to illuminate thin samples using Kohler Illumination. The white light is reflected by a silver coated mirror (2 inches, Thorlabs) towards the 4f combination of the converging lenses (2 inches, f=30cm, Thorlabs) and gets collimated. The 4f combination of

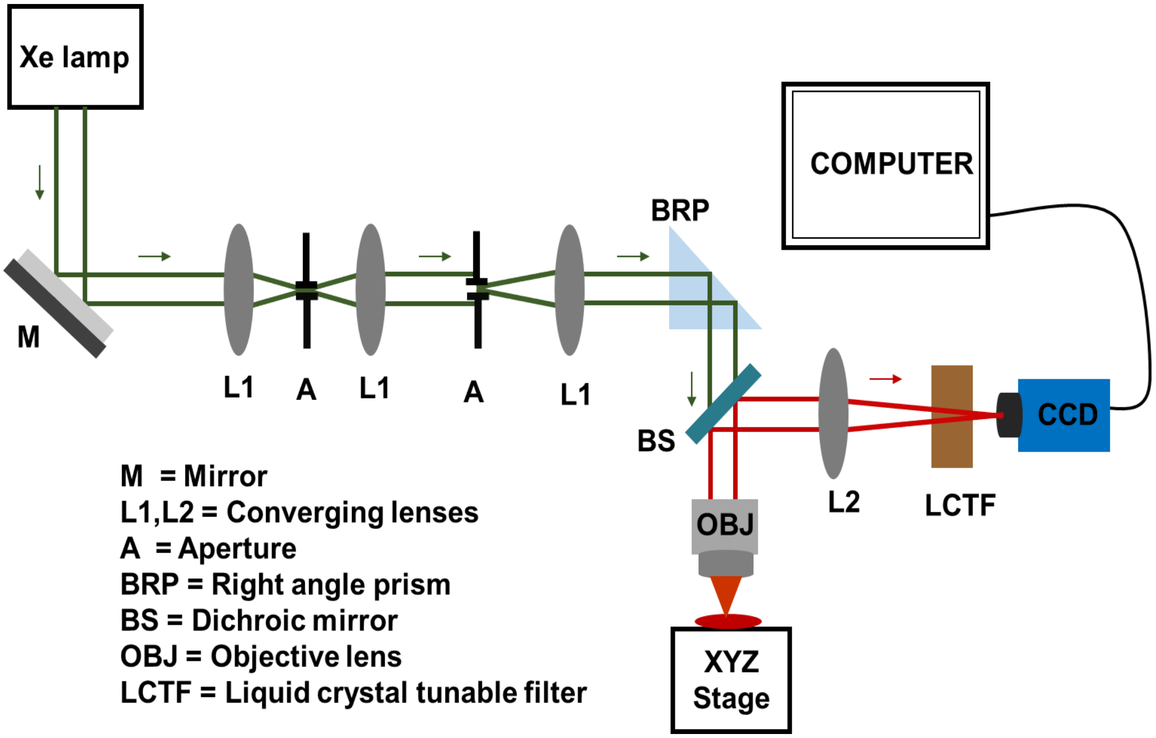

Figure 1.1 The schematic diagram of the finer focusing PWS system.

Experimental layout of the Partial Wave Spectroscopy (PWS) setup with nanoscale sensitivity. The green color represents broadband white light from the source and the red color after the dichroic mirror is the backscattered signal. The collimated beams from the 4f combination of lenses are focused on the sample using a highly sensitive motorized XYZ stage. Backscattered signals are recorded in CCD passing through the liquid crystal tunable filter.

converging lenses along with the apertures (2inches, Newport) helps to minimize the diffraction effect and preserve the high-frequency effect to enhances the sharpness of an image. The collimated light is reflected by a right-angle prism (1 inch, Thorlabs) towards 40X objectives (NA = 0.65, Newport) and focuses on the sample. A finer focusing is important to scatter the precise volume of the sample. A highly sensitive 3D electronic motorized stage (X-Y axis 40nm and Z-axis 100nm, Zebar Tech.) is used to focus the sample within the working distance of the low numerical aperture objective. This high-resolution motorized 3D stage is considered revolutionary to the microscopic setup for its extreme accuracy and finer focus. A finer focus is essential for correctly defining the effective scattering volume/length of a sample. The 1D backscattered signal from the sample is reflected towards the thick collecting lenses (3 inches, Thorlabs) by a 50:50 dichroic mirror (1 inch, Thorlabs). The collected backscattered signal is then recorded in a CCD camera (1460×1920, Retiga 3) after filtering the signal through a liquid crystal tunable filter i.e. LCTF (KURIOS-WB1, Thorlabs) in the visible range of light. The LCTF has a resolution of 1 nm in the wavelength range of 420 nm to 730 nm. Here, the CCD camera and LCTF are coupled together with the LCTF controller in such a way that for every wavelength signal filter by the LCTF in the visible range of light the backscattered signals are recorded by the CCD camera. Finally, all 1D backscattered signals from the sample are recorded in the CCD camera as a 3D data matrix $I(x,y,\lambda)$ for the PWS analysis.

1.1.2 Theoretical model using the mesoscopic physics-based approach

The recorded backscattered intensity $I(x,y,\lambda)$ are further analyzed to calculate the fluctuating component, $R(x,y,\lambda)$ of backscattered spectra arises from the interference of photons reflected from refractive index fluctuations of a scattering object. Unlike the conventional light scattering experiments where a scattering signal is formed by the interference of all waves propagating within scattering particles in the far-field, in PWS backscattered spectrum analyzed is formed by a subset of waves propagating in 1D. Low spatial coherence, high spectral resolution, weak refractive index fluctuations, and small radius of curvature within the medium are the conditions in which light propagates through a complex 3D structure and can be approximated as a combination of several spatially independent parallel 1D channels, with less mixing among the scattering channels. Here, the interference among different 1D channels is negligible and can be further prevented by low coherence illumination. The flow chart of how the PWS technique works is presented in the following figure.

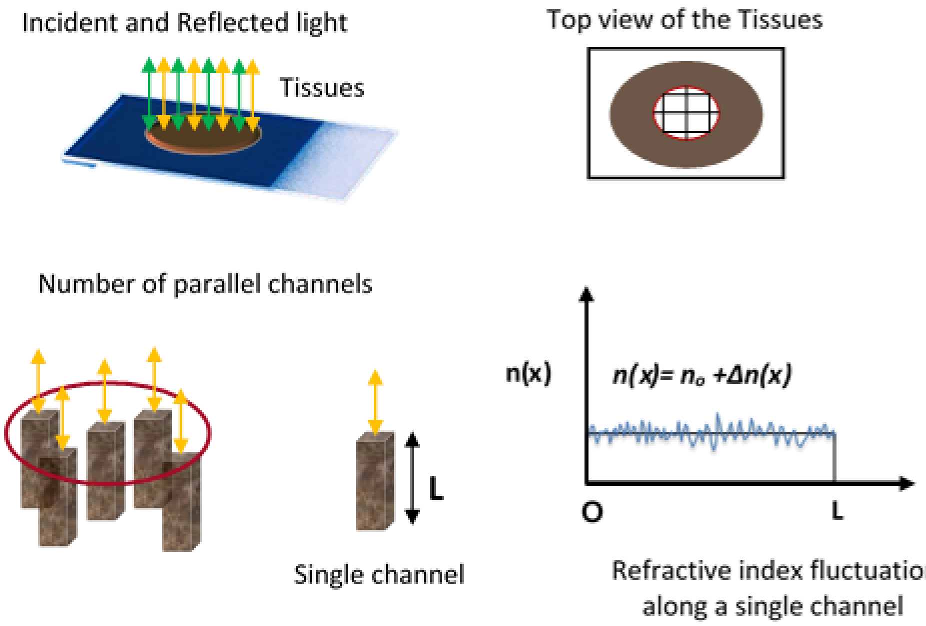

Figure 1.2 The schematic of PWS data acquisition from thin samples.

Each pixel of the image is treated as an individual channel and the refractive index fluctuations are recorded throughout the thickness of the sample (L). And hence, the degree of structural disorder is quantified for every pixel of the image.

As mentioned, PWS expresses a 3D disordered medium into different parallel and spatially independent 1D channels, acquiring the fluctuating components as $R(k)$, where k is obtained from the interference of light wave propagating in 1D backscattered channels ($k=2\pi/\lambda$). For each pixel (x,y), the variance of the refractive index fluctuation (Δn) is computed as sqrt(Δn^2). And k is computed from the intensity vs wavelength measurement of $I(k)$ at each pixel (x,y). From the signal $I(k)$ the high-frequency noise is filtered out using a low order Butterworth

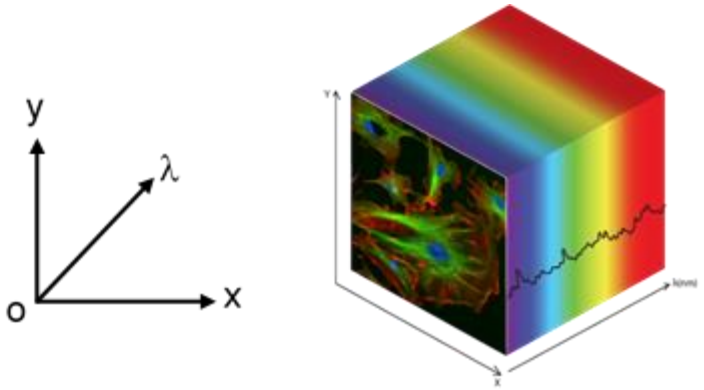

Figure 1.3 The 3D data acquired for PWS analysis.

Scanning the wavelength in the visible range of light from 430 to 720nm 3D spectroscopic data cube is recorded where XY represents the frame of the image(camera) and Z is the wavelength in the visible range using PWS microscopy.

filter to obtained $R(k)$. Further, variation in light source spectrum, instrumental artifact, sample roughness, etc. are filtered-out fitting with a low order polynomial $I_p(k)$ to $I(k)$. Finally, the fluctuating part of the reflection coefficient is obtained as $R(k)= I(k)- I_p(k)$. Now the question is how the fluctuating component $R(k)$ is related to the properties of samples like average refractive index (n_0), sample thickness or length of light penetration in the medium (L), the variance, and the correlation length of the refractive index fluctuation ($<\Delta n^2>$ and l_c).

In a weakly disorder scattering medium i.e. $R<<1$, for every length scale the probability density distribution of R follows a lognormal distribution. Thus, for length L the ensemble average of R distribution over the ensemble of 1D independent parallel disorder channels is given by:

$$\langle R\rangle = \frac{1}{2}\left[\exp\left(4k^2 L_d \, {}^{L}/_{n_0^2}\right) - 1\right] \tag{1.1}$$

Since average refractive index for biological cells/tissues is $n_0 = 1.38$ we assume that $4k^2L_dL/n_0^2 << 1$, in the above equation, therefore can be approximated as:

$$\langle R \rangle \cong \frac{1}{2}\left(\frac{4k^2 L_d L}{n_0^2}\right) \cong \frac{2k^2 L_d L}{n_0^2}, \tag{1.2}$$

In a regime with the valid 1D independent channel, $R(k)$ can be characterized using 1D mesoscopic light transport theory [19–21], and the root mean square average of $R(k)$ can be written as:

$$\langle R \rangle = L\xi^{-1}, \tag{1.3}$$

Where ξ^{-1} is the scattering coefficient of the 1D channel simplified for $kl_c << 1$: $\xi^{-1} \cong 2k^2 L_d L/n_0^2$ with $L_d = <\Delta n^2> l_c$. Therefore,

$$\xi^{-1} \cong \left(\frac{2k^2 \langle \Delta n^2 \rangle l_c}{n_0^2}\right). \tag{1.4}$$

To eliminate L, and only use intrinsic properties of the sample, we introduce an autocorrelation function $\langle C(\Delta k) \rangle$:

$$\langle C(\Delta k) \rangle = \frac{\langle R(k) R(k+\Delta k) \rangle}{\langle R(k) R(k) \rangle}, \tag{1.5}$$

Based on mesoscopic theory, $\langle C(\Delta k) \rangle$ can be expanded as [19]:

$$\langle C(\Delta k) \rangle \cong exp(-(\Delta k)^2 f(L_d)\alpha L). \tag{1.6}$$

Where $f(L_d)$ is a slowly varying function for realistic values of the disorder strength which may be considered as constant for a range of k, and α is a constant with a unit of length. Thus,

$$ln(\langle C(\Delta k) \rangle) = -(\Delta k)^2 f(L_d)\alpha L;\; L = -\frac{1}{\alpha f(L_d)} \frac{ln(\langle c(\Delta k) \rangle)}{(\Delta k)^2}. \tag{1.7}$$

Using the above equation, the mean reflectance fluctuation can be obtained as:

$$\langle R\rangle \cong -\frac{2k^2 L_d}{n_0^2}\frac{ln(\langle c(\Delta k)\rangle)}{\alpha f(L_d)(\Delta k)^2}. \tag{1.8}$$

Hence, for slowly varying functions knowing $\langle R\rangle$ and $C\langle \Delta k\rangle$ for each channel in the sample one can calculate disorder strength (L_d) as:

$$L_d = \frac{Bn_0^2\langle R\rangle}{2k^2}\frac{(\Delta k)^2}{-ln(\langle C(\Delta k)\rangle}. \tag{1.9}$$

Where B is a calibration constant determined experimentally, k is the wavenumber ($k=2\pi/\lambda$)and $(\Delta k)^2/ln\langle C(\Delta k)\rangle$ is obtained by performing a linear fit of $ln\langle C(\Delta k)\rangle$ vs $(\Delta k)^2$.

For the Gaussian color noise of the refractive index at position r and r', then spatial correlation is defined as: $<dn(r)dn'(r')> = dn^2 exp(-|r-r'|/l_c)$, it can be shown that $L_d=<\Delta n^2>l_c$. Thus, the disorder strength quantifies the variability of the local density of intracellular material within the samples, and hence the average and standard deviation of the L_d is calculated to characterize the structural abnormalities of the system.

1.1.3 Applications of the finer focusing PWS technique on cancer tissue samples

As applications of the developed nanoscale sensitive PWS system, we first quantify the nanoscale changes in mass density or refractive index fluctuations using commercially available TMA tissue samples in progressive cancer. Then we employ this sensitive technique to probe the refractive index fluctuations in 3D tumor structure grown from 2D drug-sensitive and drug-resistant prostate cancer cells using a xenograft model, to differentiate the difference in structural changes in 2D and 3D growths. Following are the details.

In chapter II, we use the developed highly sensitive PWS technique to quantify the nanoscale refractive index fluctuations using commercially available paraffin-embedded tissue microarrays (TMA) samples with the goal to standardized early to late cancer stages detection and possible application in the future to study drug effect in cancer treatment. Recently the use of these scientific TMA tissue samples has gained research interest in diagnosing different diseases and drug-effect in treatment since they allow high throughput analysis and are easily accessible. Fractal dimension study of TMA sample shows that fractal dimension increases with the increase in cancer stages. Also, cancer is an epidemic worldwide, early, and accurate detection, as well as the study of drug effects in cancer treatment, are always in demand. Therefore, in this study, we mainly focused on deadly cancer tissue samples such as pancreatic, prostate, breast, and colon cancer TMAs containing multiple cores of different stages for each cancer. These are analyzed using the PWS technique and the degree of disorder strengths L_d were quantified and distinguished the stages of cancer successfully. The promising application of the TMA-PWS technique will be explored in detail.

In chapter III, we are mainly interested to study the structural properties of the tumor tissues that are developed from drug-sensitive and drug-resistive prostate cancer cells inside the body using the PWS technique. Other than cancer detection, the effects of cancer drug treatment are also an important field in cancer study. One of the questions addressed here is to see the difference between the 2D and 3D growth structures in cancerous cells for detection/estimation of cancer by cell/tissue cultures. At this point, a PWS study of the drug-sensitive and drug-resistive prostate cancer cell lines 2D model showed that drug-resistive cancer cells have higher structural disorders relative to drug-sensitive cancer cells, at the single-cell level. In this chapter, using a further engineered PWS, we characterize tumor 3D structure developed from the docetaxel chemotherapy drug-sensitive and drug-resistant different prostate cancer cells by a xenografted model, to study the structural properties of these cancer single cells grown in 2D slides to 3D tissues in xenografting technique. The result obtained is important and hence, the potential applications of the technique to access chemo drug effectiveness in the treatment of human cancer patients will be discussed.

1.2 Inverse participation ratio (IPR) photonics technique

Light localization arises due to the interference of light waves within the optical disordered medium. In condensed matter physics, the light localization method which we defined as the inverse participation ratio (IPR) technique has been well studied for characterizing the degree of disorder of homogeneous and heterogeneous media in a single parameter [32–34]. Further, quantification of light localization in weakly disordered optical disorder mediums such as polymers, thin dielectric films, cells, and tissues, etc. is a major interest of research to characterize the degree of structural disorder of that medium. The characterization of these optical disordered mediums using standard methods is more complicated if the system involves spatial heterogeneity involving many kinds of spatial correlation decay length scales within the sample like cells/tissues [35,36]. In the present day, significant research has been performed in quantifying structural disorders of cells/tissues by analyzing the light transportation and localization properties [15–17,22,23,37]. This research has shown that analysis of light localization properties of cells/tissue is a useful technique to understand the intramolecular tumorigenicity levels, by probing their structural disorder. The light localization technique was explored to study nano to submicron scale structural disorder in cells/tissues with a potential application in cancer diagnostics [22]. Consequently, this novel approach of using mesoscopic physics-based optical localization analysis [28,32,33], to understand disease processes in cells/tissues has created a new avenue in medical diagnostic technologies. In ref [22], it is shown that the degree of structural disorder in heterogeneous biological samples can be quantified as a single mixed parameter via IPR analysis of the light wavefunctions of these systems. In a weakly disorder system, the degree of structural disorder relates to the mass density or refractive index fluctuation which is linearly proportional to the IPR value of the system [32,33]. In this technique, transmission electron microscopy (TEM) or confocal fluorescence microscopy micrographs are used to construct optical lattices from the sample which represents 2D refractive index map corresponding to the spatial mass density distribution of specific molecule within the cell; subsequently light localization properties were analyzed [22,23,38]. Last few decades the disorder analysis of the optical media has been well studied using light localization properties [28–30,32,33,39]. In a closed disordered optical medium, the light wave eigenfunctions are localized due to the multiple interference effects within the disordered sample. The main length scale associated with the problem, in IPR technique is the localization length or the scattering mean free path, which is related to the physical properties of the system, refractive index fluctuations and its correlation. Light localization effect is strong in 1D and 2D systems and the average IPR value of uniform lattice in 2D is universal number ~2.5, but the value increases with an increase in degree of disorder of the lattices [32].

1.2.1 Confocal microscopy imaging

Confocal laser scanning microscopy is a powerful optical imaging technique that offers significant advantages over conventional microscopy to view the biological samples with high optical resolution and contrast of a micrograph [40–42]. In laser scanning microscopy the specimen is scanned by the diffraction-limited spot of laser and the light reflected by the in-focus illuminated volume element of the specimen is focused onto a photoreceptor. It uses a spatial pinhole to block out-of-focus light to form an image, on the image plane. Confocal microscopy enables capturing of multiple 2D backscattered photons at different depths of a sample and constructs a 3D structure. Therefore, the ability to control the depth of field, eliminate or reduce information from the focal plane, and collect serial optical sections of thick samples has enhanced advantages in optical microscopy. The fluorescence emitted by the molecule from a small volume around the excitation center is collected by the objective into the photodetector using a spatial pinhole. The schematic of how the confocal microscopy work is presented in the following Fig. 1.4.

As shown in Fig 1.4, confocal microscopy consists of the laser source, scanning mirror or dichroic mirror, objective lens, pinholes, and a detector. The backscattered signals from the samples are collected by the objectives and recorded into a detector through a confocal pinhole that blocks the out-of-focus light. Thus, confocal pinhole rejects out-of-focus light resulting in high optical resolution and contrast image and have made confocal microscope a powerful technique in obtaining 3D optical resolution.

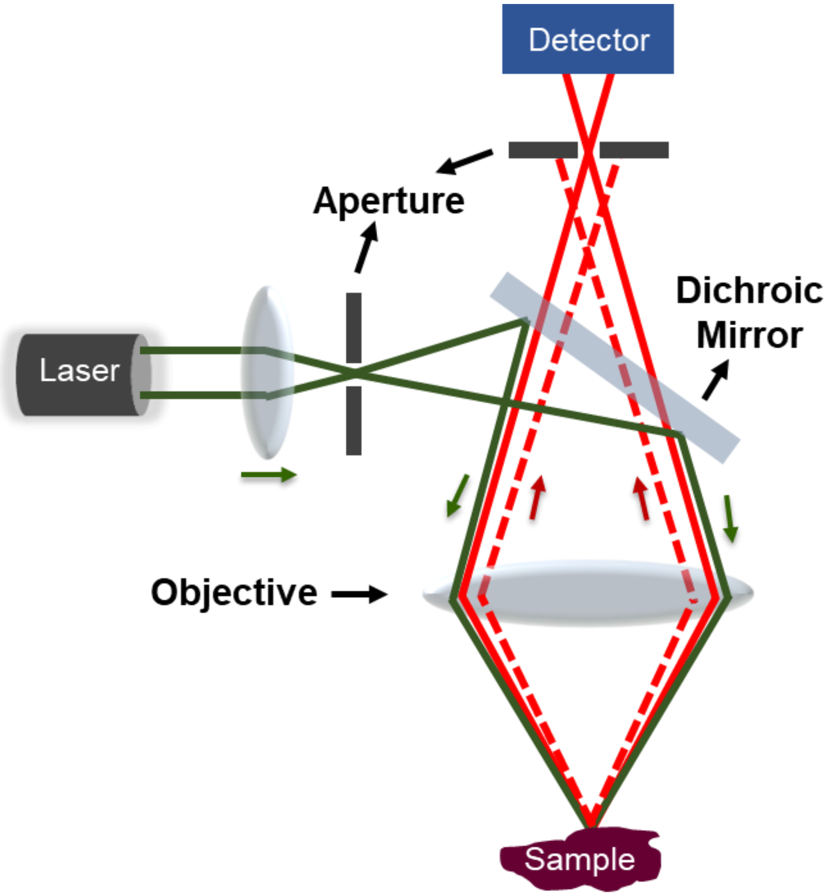

Figure 1.4 A schematic ray diagram of confocal microscopy.

Schematic ray diagram based on the principle of recently developed laser scanning confocal microscopy. In confocal imaging, samples are treated with different dyes/proteins targeting different cells/components of the cells using different excitation sources.

1.2.2 Transmission electron microscopy (TEM) imaging

Transmission electron microscopy uses de Broglie wavelength of electrons from a micrograph that has a significantly higher resolution than any existing fluorescence microscopy. In TEM microscopy high-energy electrons (80-200kev) are transmitted through electron transparent samples (~100nm thickness) and probe up to ~1nm to identify the nanoscale architectural alterations inside the cells due to progressive cancer or any other abnormalities. That means a beam of the electron is transmitted through the ultrathin specimen to form a TEM image. The image is magnified and focused onto an imaging device known as a fluorescent screen. Hence, TEM and scanning TEM techniques can provide imaging, diffraction, and spectroscopic information with an atomic or sub-nanometer spatial resolution and contribute a major analytical tool in the physical, biological, and chemical sciences [43–45].

The schematic diagram for the TEM micrograph formation is shown in Fig. 1.5. In brief, TEM components include electron source, condenser lenses, objective lens system, intermediate or projector lenses, and a detector. They produced high energy and coherence electron source necessary for diffraction pattern is passed through condenser lenses which control the spot size and illumination area of the specimen. An objective lens system is used to images the specimen and intermediate or projector lenses change the modes from diffraction to imaging. Finally, highly sensitive and low quantum efficiency detectors of various configurations are used to collect the secondary signals produced by the high-energy electron beam.

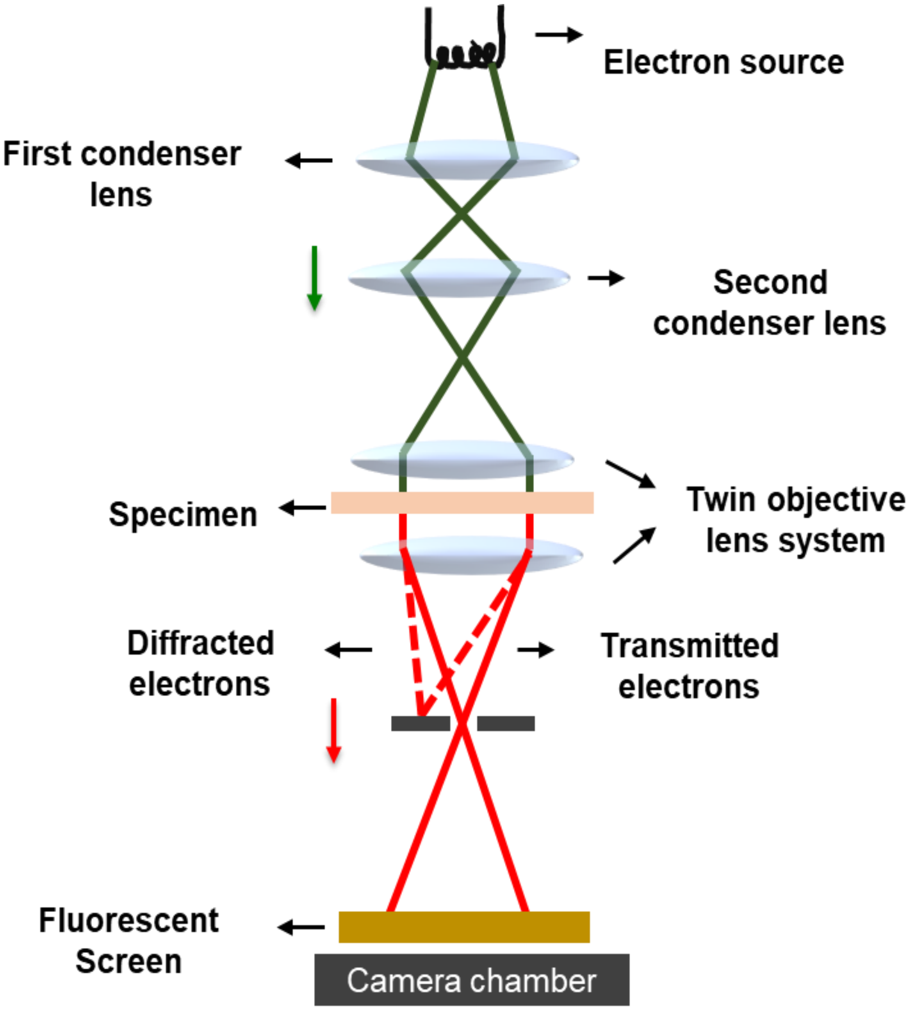

Figure 1.5 A schematic ray diagram of transmission electron microscopy (TEM).

Schematic ray diagram of TEM in image mode where electron beam passes through the thin sample to produce micrograph in fluorescent screen. Therefore, a TEM micrograph can represent the mass density of the thin cell sample.

1.2.3 The theoretical model for analysis of confocal/TEM micrograph using mesoscopic light localization approach

The optical lattices of cells/tissues are constructed using TEM or Confocal micrograph to study the molecular specific light localization properties. It is found that optical refractive index *n(x,y)* is linearly proportional to the local density *ρ(x,y*) of intercellular macromolecules such as DNA, RNA, lipids, or protein present in cells. The refractive index of a cell can be expressed as

$n(x,y)=n_0 + dn(x,y)$, where n_0 is the average and $dn(x,y)$ is the fluctuation of refractive index at (x,y) [22,23]. In the case of the thin sample, a voxel of area $dxdy$ the transmission or scattered intensity: $I(x,y) = I_0 exp(-\alpha dz/z_0)$; or $I(x,y) \approx I_0(1-\alpha dz/z_0)= I_0 - I_0 \alpha d(z)$, where α is a constant depends on the mass of voxel. That means, image intensity at any voxel point (x,y) for a thin sample $dxdy$ defined as $I(x,y)$ given by $I(x,y) = I_0+ dI(x,y)$, where I_0 is the average pixel intensity and $dI(x,y)$ is the fluctuation part of the pixel intensity. The fluctuation of intensity $dI(x,y)$ is less than the average intensity I_0: $I_0=<I(x,y)>_{(x,y)}$ and $dI(x,y)=I(x,y) - <I(x,y)>_{(x,y)}$. Similarly, the fluctuation of refractive index $dn(x,y)$ is less than the average refractive index n_0.

We assume that image intensity is linearly proportional to the total mass present in the thin cell voxel. Therefore, it is observed that (i) image intensity $I(x,y)$ is linearly proportional to the mass density of the voxel $M(x,y)$, and (ii) the refractive index of the voxel $n(x,y)$ is proportional to the mass density $M(x,y)$, then we can write:

$$I(x,y) \propto M(x,y) \propto n(x,y), \tag{1.10}$$

$$I_0 + dI(x,y) \propto M_0 + dM(x,y) \propto n_0 + dn(x,y). \tag{1.11}$$

Consequently, it can be shown that the effective(average) optical potential or optical lattice, ε_i, for the voxel around the point (x,y) is

$$\varepsilon_i \propto \frac{dn(x,y)}{n_0} = \frac{dI(x,y)}{I_0}. \tag{1.12}$$

The schematic of the disorder optical lattices of size $L \times L$ of TEM/Confocal image where each dot in the optical lattice is determined from the pixel intensity values in recorded images as shown in the figure below.

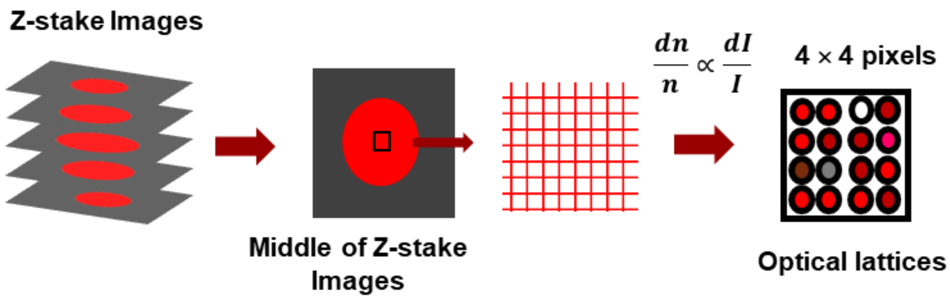

Figure 1.6 Construction of a disorder optical lattices from TEM/Confocal micrograph.

A typical example of z-stack confocal micrographs from which one micrograph is selected and optical/refractive lattices are constructed for a small close region.

Tight-binding model: To quantify the disorder properties of TEM or Confocal images, Anderson disorder tight-binding model (TBM) calculation was employed. The TBM is a good model for describing single-optical states of the system of any geometry and disorder [28–30], where the Hamiltonian is defined as:

$$H = \sum_i |i><i| + t\sum_{\langle ij\rangle}(|i><j| + |j><i|)\ , \tag{1.13}$$

where $|i>$ and $|j>$ are the optical wave function or eigenvectors at i-th and j-th lattice sites, $<ij>$ indicates the nearest neighbors, $\varepsilon_i(x,y)$ or simply ε_i is the i-th lattice site optical potential energy and t is the overlap integral between sites i and j. The eigenfunctions (E_i's) can be obtained by diagonalizing above the Hamiltonian. For a sample length L in the image, we have $L\times L$ sample area. The average IPR at sample length L is calculated where $L=N_L\times dx$ ($dx=dy$). Since there are $N=N_L\times N_L$ numbers of lattice points, thus, there will be N eigenvalues and the same number of eigenvectors. Now substituting the value of ε_i in Hamiltonian and solving for average IPR value of the sample of length L defined as [22,23,32,33,46,47]:

$$< IPR(L) >_{L\times L} = \frac{1}{N}\sum_{i=1}^{N}\int_0^L\int_0^L E_i^4(x,y)dxdy, \tag{1.15}$$

Where E_i is the *i*-th eigenfunction of the above Hamiltonian equation of optical lattices of size $L\times L$, and N is the total number of potential points on the refractive index matrix (i.e., $N=(L/dx)^2$). That means if there is $L\times L$ sample length or N number of image pixels, this will provide one pixel of the IPR image of length L, as $<IPR(L)>_{L\times L}$.

It has been shown that the ensemble average of IPR value i.e. averaged of similar type of cells: $<<IPR(L)>>=<<IPR(L)>_{L\times L}>$ *or* $\sigma(<IPR(L)>$, is proportional to the degree of structural disorder $L_d=dn\times l_c$, where *dn* is the *std* of all *n(x,y)* point of cell samples/ensemble and l_c is the spatial correlation decay length of the average *n(x,y)* over the sample [22,23]. Thus,

$$\langle\langle IPR(L)\rangle\rangle = \langle\langle IPR(L)\rangle_{L\times L}\rangle_{cell} \sim L_d = dn\times l_c, \tag{1.16}$$

$$\sigma(\langle IPR(L)\rangle) = \sigma(\langle IPR(L)\rangle_{L\times L})_{cell} \sim L_d = dn\times l_c. \tag{1.17}$$

The $< IPR(L) >_{L\times L}$is the average value of one IPR pixel of length (L) constructed from the $L\times L$ area of the TEM or Confocal image. After this, statistical analysis involves calculating the average and standard deviation of the disorder strength of IPR values, i.e. L_d values over the cell for the length of a given sample. Using this structural disorder strength $<<IPR(L)>>$ *or* $\sigma(<IPR(L)>)$ or L_d as a biomarker, we quantify the nanoscale structural abnormalities in cells/tissues due to cancer or any other abnormalities. A typical schematic of the steps involved in the quantification of structural disorder to study the drug effect in cancer treatment using a TEM micrograph is shown in figure 1.7.

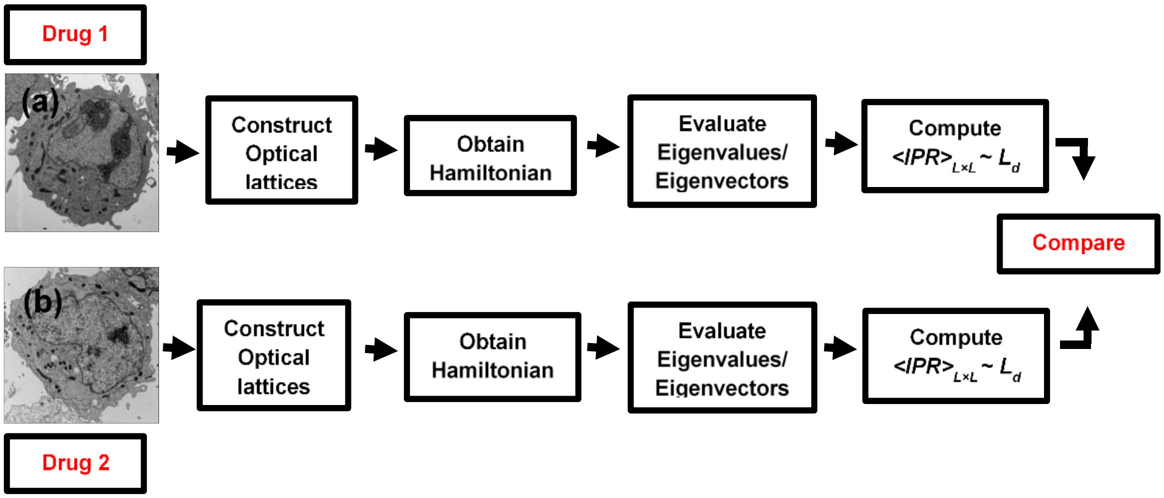

Figure 1.7 Schematic flowchart for calculating and comparing the $<IPR>$ using TEM images.

In summary, the main steps involved in the calculation of $<IPR>$ using a TEM micrograph are presented in the schematic flowchart.

1.2.4 Steps involved in the IPR calculation

In brief, we want to summarize the steps involved in the calculation of IPR explained in above Section 1.2.3. Fig. 1.7 roughly shows the steps involved in the calculation of the average or std of IPR and IPR images from the confocal or TEM micrograph. However, the steps involved in the IPR calculation can help you better understand how we quantify disorder strength (L_d) using the IPR technique and confocal or TEM micrograph:

Step I: Confocal or TEM micrographs are collected from the cells/tissues.

Step II: Using the pixel intensity values of the micrographs, a pixel intensity was obtained in the form of a matrix as: $I(x,y) = <I_0> + dI(x,y)$.

Step III: Based on pixel intensity matrix of micrograph optical refractive index lattices/matrix is obtained which correspond to the one-to-one micrograph pixel intensity expressed as: $dn(x,y)/n_0 \propto dn(x,y)/<I_0>$. And hence the optical lattice system of the micrograph is obtained such that every point in the optical lattice is defined as optical potential represented by $\varepsilon(x,y) = dn(x,y)/ n_0$. Now the micrograph intensities are replaced by the optical potential matrix which in turn represents the refractive index or mass density fluctuation of the sample. Hence the optical lattice depicts the refractive index variation of the 2D plane to calculate the disorder strength inside the sample.

Step IV: Now if 2D lattices have $M \times M$ pixels with the pixel size a, then the total pixel size of the 2D micrograph is $Ma \times Ma$. For instance, we choose a small sample size $L \times L$, with $m \times m$ optical lattice points with $L = ma$ $(M>m)$. Applying Anderson Tight Binding Model on this sample size using optical lattice we will calculate the eigenfunction E_i of the small close system.

Step V: Once the eigenfunction of the close system $L \times L$ is obtained we calculate the $<IPR>_{L \times L}$ using the equation (1.15). Here it represents the unit block or the IPR pixel of the IPR image. That means we repeat this process throughout the micrograph and the distribution of $<IPR>_{L \times L}$ is obtained, which is represented in the IPR image. For $Ma \times Ma$ confocal 2D micrograph $Ma/m \times Ma/m$ IPR pixels are constructed.

Lastly, the ensembled average or standard deviation of $<IPR>_{L \times L}$ is obtained from $<IPR>$ distribution of IPR image at $L \times L$ by averaging or calculating std of all micrographs of the cells/tissues for the particular case study as $<IPR(L)> = <<IPR>_{L \times L}>$ or $\sigma(<IPR>) = \sigma(<IPR>_{L \times L})$.

1.2.5 Applications of confocal-IPR and TEM-IPR techniques

IPR is a very powerful technique to quantify the molecular-specific disorder present in the weakly disorder optical medium based on the light localization on the closed system and has numerous applications. Mainly in this dissertation, we will apply IPR techniques combined with confocal and TEM imaging to quantify nano to submicron scale mass density or refractive index fluctuations to study probiotic effects in chronic alcoholic brain cells and anti-cancerous drug effect in ovarian cancer cells using a mouse model.

In chapter IV, using a confocal-IPR technique we will quantify the molecular specific structural alteration in glial cells and chromatin of the alcoholic brain cells and study the probiotic, *Lactobacillus Plantarum* treatment on chronic alcoholic brain cells/tissues at the submicron level. Previously, confocal imaging using IPR has shown tremendous success in distinguishing cancer stages now we want to explore its applications in determining brain abnormalities. Based on the close scattering technique, we probe overexpression of astrocyte and microglial cells, and chromatin structures of brain cells, and quantify the molecular-specific overexpression by staining the cells with appropriate dye/proteins and calculating the degree of spatial molecular mass density structural disorder (L_d). Our technique has successfully detected the effect of the probiotic in alcoholic brain cells and components. The potential application of this novel approach to diagnosing the alcohol effect and probiotic treatment in the alcoholic brain is explored.

In chapter V, combing the IPR technique with TEM images we quantify the efficacy of the anti-cancerous drug treatment in ovarian cancer treatment using a mouse model. Here, we also want to know how the IPR technique is useful with nanoscale resolution, especially in cancerous cells. The TEM imaging on thin cell, sections are performed to obtain their nanoscale structures up to 1 nm. Therefore, using TEM-IPR we can probe up to a few nanometers to quantify the structural alterations of tumorigenic cells and anti-cancerous drug-treated tumorigenic ovarian cancer cells which are initially effective at the nanoscale level. Results are interesting and support that the effect of anti-cancerous drugs in cancer treatment can be quantified by using the degree of nanoscale fluctuations of the cells via TEM imaging. Potential applications of the TEM-IPR technique for cancer treatment are also discussed.

Lastly, in chapter VI, conclusions of the close and open scattering spectroscopic techniques PWS and IPR, respectively are presented and their near-future applications are explored in detail.

1.2.6 Advantages of PWS and IPR techniques over the existing other spectroscopic scattering technique

Despite the tremendous achievement in the development of different biomedical optical techniques such as optical coherence tomography (OCT), fluorescence spectroscopy, diffusion spectroscopy, coherence enhanced backscattering, etc. [1–10,48] the optical sensing of the nanoscale structure remains an open problem due to the fundamental principles of diffraction-limited resolution. These techniques are mainly based on the change in the scattering signal when the bulk properties of a sample are changed ($n(x)=n_0+dn(x)$, $<n(x)>=n_0$). In the case of cancer detection, these methods are useful in the later stages of cancer when there is a prominent change in the bulk properties. But it is recently proven that fluctuations ($dn(x)$) part of the refractive index are more sensitive and vital information about the system even when the bulk properties do not change. By using nonlinear techniques, spatial-frequency evanescent waves, metamaterial-based lenses, and grating assisted tomography have enhanced a resolving power beyond the diffraction of a light [49,50]; however, the super-resolution is confined to the transverse plane which limits its ability to characterize sub-diffraction structure in 3D [51,52] and allows only the spatial distribution of particular molecular species. This demands the exploration of non-invasive, label-free, cost-effective, and elastic scattering spectroscopic microscopy techniques to characterize the endogenous properties of the medium based on the spectral content of diffraction-limited microscopic images such as PWS. The PWS and IPR technique is pioneering in probing the fluctuation part of the RI to probe the physical state of cells or tissues. The theory behind the PWS technique involves strong assumptions that 1D backscattered signals are sensitive to refractive index fluctuations at any length scale including far below the wavelength range [11]. Using both open (PWS) and close (IPR) scattering we probe the particular structure in a weakly disordered medium in terms of the refractive index fluctuations where 1D scattered signals are sensitive to any length scale. The important aspect of these mesoscopic physics-based PWS and IPR techniques is a quantification of the L_d parameter which linearly depends on l_c for $kl_c < 1$. Thus, in principle, there is no limitation on the minimum correlation length that can be assessed by the means of spectral analysis of 1D propagating photon. In practice, the sensitivity of l_c is limited by the signal-to-noise ratio and other technical parameters. That means the sensitivity of these spectroscopic techniques is not limited by fundamental physical limits. Besides this advantage, PWS is simple, cost-effective, fast, and portable, on the other hand, the IPR technique is simple, effective, and robust to probe inner fluctuations at the nano to submicron level using confocal and TEM imaging.

CHAPTER II

OPTICAL DETECTION OF CANCER STAGES VIA PWS USING TISSUE MICROARRAYS (TMA) SAMPLES

This chapter is adapted from the author's published article with copyright permission from the publishers. Ref [61] P.Adhikari, F. Alharthi, and P. Pradhan, "Partial Wave Spectroscopy Detection of Cancer Stages using Tissue Microarrays (TMA) Samples," in ***Frontiers in Optics + Laser Science APS/DLS (2019), Paper JW4A.89, OSA 2019***; and Ref [94] P. Adhikari, and P. Pradhan, "Optical detection of cancer stages via partial wave spectroscopy using tissue microarrays (TMA) samples". ***arXive 2012.14194, 2020***.

The developed finer focusing added mesoscopic physics-based imaging technique, PWS can probe the precise scattering volume in cells/tissue to detect changes in refractive index fluctuation with the progression of cancer. Here, we employ this highly sensitive PWS technique to quantify the nanoscale refractive index fluctuations using commercially available paraffin-embedded TMA samples with the goal of the standardized early and accurate detection of stages of different cancers. The uses of scientific TMA samples have gained research interest in diagnosing different diseases and drug treatment since they are commercially accessible. Mainly, deadly cancer such as pancreatic, prostate, breast, and colon cancer TMAs containing multiple cores of different stages for each cancer are analyzed using the PWS technique and the degree of disorder strength (L_d) was quantified. The potential application of the developed TMA-PWS technique to enhance and standardize early and accurate cancer diagnosis modalities are discussed.

2.1 Introduction

The optical detection of structural changes in biopsy samples due to progressive cancer has achieved tremendous success in detecting the stages of cancer when developed into a tumor [53]. The standard pathological method of detection of cancer stages includes microscopic examination of the morphological changes using stained biopsy samples. However, due to the diffraction-limited resolution of conventional microscopy, the structural alterations in healthy tissue before the development of a tumor or early stages are still a mystery. These structural alterations of healthy cells/tissue are due to the rearranging of macromolecules such as DNA, RNA, lipids, etc. whose size ranges from 100-200 nm. It is recognized that genetic and epigenetic alterations occur not only at the neoplastic focus but more diffusely in the field of cancerization. The abnormalities are present in the tissue surrounding the cancerous region or transformed cell primary tumor due to field cancerization [54,55], which are initially at the nanoscale level before tumor formation and migration. This effect is observed in almost every type of cancer that is diagnosed in the later stages with less survival rates. Therefore, a highly sensitive optical method to detect such structural abnormalities before the development of a tumor for all cancer is paramount for decreasing lethality [56]. With the progress of time, several microscopic imaging techniques were employed, and regardless of their drawbacks, significant success was achieved [57]. Unfortunately, most of these methods are still not sensitive enough to probe the nanoscale structural changes. In light of this scenario, the versatile approach of using recently developed PWS to probe change in the refractive index fluctuations in commercially available tissue microarray (TMA) samples could standardize the cancer diagnostic modalities. The recently developed finer focusing PWS technique is sensitive enough to probe nanoscale refractive index fluctuation in paraffin-embedded TMA samples. The PWS combines interdisciplinary approaches of mesoscopic physics and optical imaging techniques to quantify the degree of disorder strength (L_d) based on the change in refractive index fluctuations within the cells/tissue [15–17,58]. The backscattered signal at any point within a weakly disordered medium contains the spectral fluctuations which are proportional to the local density of macromolecules or refractive index fluctuations, in fact, independent of chemical composition. Thus, once the refractive index fluctuations of the medium are known, the spatial variations of macromolecular density can be measured using the disorder strength (L_d) measure as $L_d = <dn^2> l_c$, where $<dn^2>$ is the square of *rms* and l_c is the correlation length of the refractive index fluctuations [16,17]. This potential biomarker, the L_d parameter has shown tremendous success in distinguishing stages of cancer, drug-effect in cancer treatment, and quantifying any other type of abnormalities in the brain [17,58–61]. In addition to this, structural alterations in biological cells/tissue due to cancer or any other abnormalities are quantified using mesoscopic physics-based molecular specific light localization technique in terms of the degree of disorder strength [23,38,62–64].

With the availability of such a powerful approach to quantify the nanoscale structural alterations in cancerous tissue, the next challenge was in the use of an almost identical tissue sample that allows high-throughput analysis to standardize diagnostic techniques. For this, the recently developed commercially available TMAs have been used which significantly facilitate and accelerates tissue analyses using a highly sensitive PWS technique. The TMA is a scientific form of condensed histopathology where the tissues are kept in a single glass slide to provide a miniature multiplex platform for the analysis of ~10 to ~200 tissue samples [65]. Multiple cores of paraffin-embedded tissue in a TMA allow high-throughput assessment of macromolecules in PWS analysis that standardize the diagnostic technique reducing the variability seen on the assay of individual samples. This uniformity of assay has reduced the drawbacks in specimen handling and their impact on data acquisition [66]. Besides these facts, TMA samples are easily accessible to perform any scientific experiments which require more than one similar sample. Also, we believe the use of the PWS technique in the TMA sample could be a new direction to explore to study the drug effect in cancer or any other abnormalities that are in demand. This can be noted that we want to probe change in RI fluctuations in tissue samples that are embedded in paraffin.

In this chapter, we will analyze four different deadly cancer TMA samples: *pancreatic, breast, colon,* and *prostate,* and generalize the efficacy of developed finer focusing PWS to detect the cancer stages. Cancer is a common disease and with no surprise, these four different cancers are the major cause of death in the U.S. Because of lethality, prevalence, and almost no prominent physical change or symptoms until the later stages. We focus on studying the nanoscale structural changes in these cancerous tissues by quantifying the degree of structural disorder (L_d) as a potential biomarker. In this sense, we explored the potential possibilities of the PWS technique in TMAs for the early stage of cancer detection.

2.2 Methods

2.2.1 Experimental development of the PWS

The engineered finer focusing PWS system used to probe the precise scattering volume developed in the Bionanophonics laboratory is as shown in Fig. 2.1. The experimental details of the PWS setup are presented in Chapter I Section 1.1.2 [58–60,67]. We will present a 3D view of the PWS system presented in Chapter I. In brief, the developed PWS system consists of a low coherence broadband stable white light source Xenon lamp which is reflected toward the 4f combination of lenses by a mirror and gets collimated. Collimated beams are reflected towards the objectives and focus on the sample with the help of a highly sensitive XYZ motorized scanning stage (XY-axis 40nm and Z-axis 100nm). Then, the backscattered signal from the sample is directed towards the CCD camera through the liquid crystal tunable filter (LCTF) with the help of a dichroic mirror. Here, LCTF is coupled with a CCD camera in a way that for every wavelength in the visible range, images are recorded in the CCD camera for the PWS analysis.

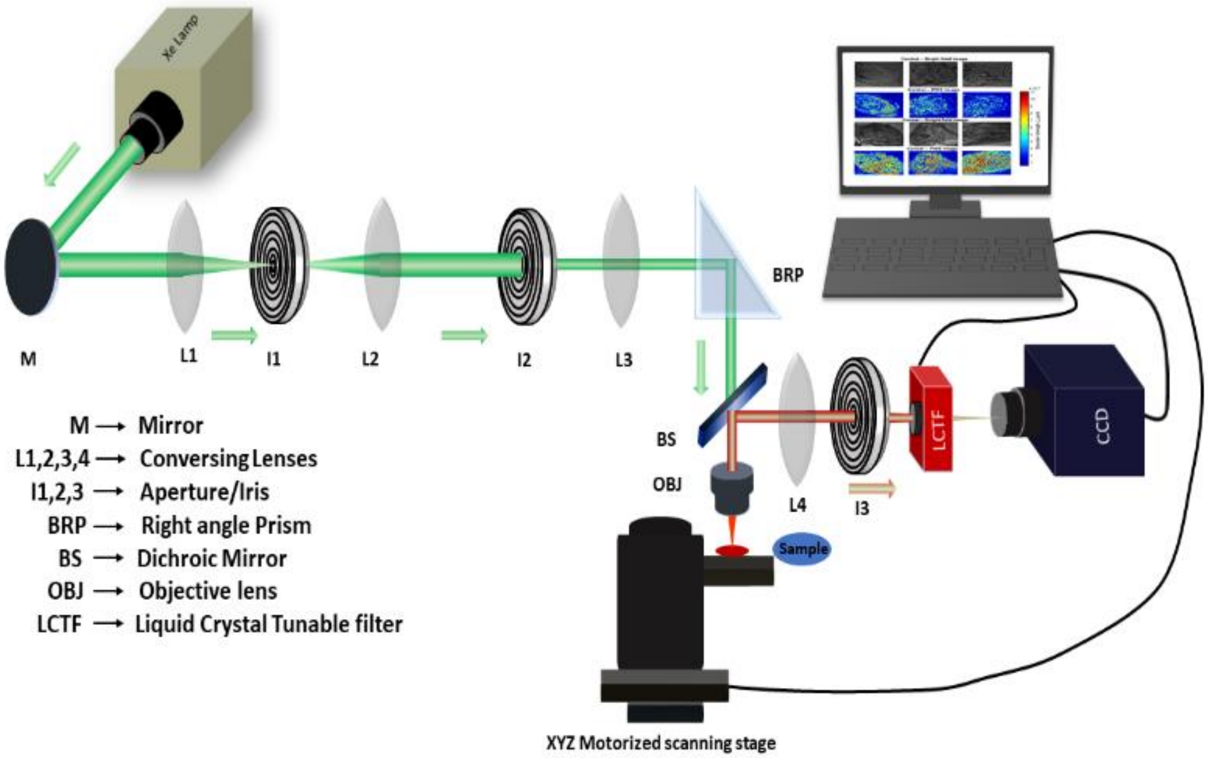

Figure 2.1 The 3D schematic of further engineered finer focusing PWS system.

The schematic 3D layout of the finer focusing partial wave spectroscopy (PWS) system was developed in the Bionanophotonic laboratory. The collimated beam (green color) from the broadband stable white light source (Xe lamp) is focused on the sample and the backscattered signal (red color) from the sample is collected using the CCD camera for PWS analysis.

2.2.2 Calculation of the disorder strength (L_d)

In the PWS technique, the backscattered spectrum of a weakly disorder medium is recorded in the visible range of light to quantify the degree of disorder strength (L_d) based on the refractive index fluctuations (Δn) within the cells/tissue. It is shown that at each pixel position (x,y) within the cell, the refractive index (n) is proportional to the local mass density and practically independent of chemical composition at that point. Therefore, the spatial variation of macromolecular mass density at every pixel position can be expressed in terms of refractive index fluctuations, assuming that these random fluctuations are within a correlation length (l_c). The recorded backscattered spectrum $R(x, y; \lambda)$, is the interference between the intercellular volume scattering and reflection from the surface of the sample. That means the measured spectra from each pixel of an image is a 1D weakly disordered medium that acts as a subset of the scattered waves.

The step-wise quantification of backscattered signals using the PWS technique is shown in Chapter I Section 1.1.2. In 1D weakly disorder medium, the probability density distribution of reflectance fluctuations R, follows a log-normal distribution for all the sample length scale L, reflected from the scattering medium. As mentioned, PWS collects the backscattered signals propagating along the 1D trajectories since in a quasi-1D approximation the sample is virtually divided into many parallel channels within the diffraction-limited transverse size. Then, by applying mesoscopic light transport theory and making use of refractive index fluctuations, the degree of disorder strength is calculated. In particular, the *rms* value of the reflection intensity $<R(k)>_{rms}$ and the spectral auto-correlation of the reflection intensity $C(\Delta k)$ for a given pixel at position (x,y), are combined to define the degree of disorder strength as [16,17,68] discussed in Chapter I Section 1.1.2:

$$L_d = \frac{B\, n_0^2\, \langle R \rangle_{rms}}{2k^2} \frac{(\Delta k)^2}{-\, ln\big(C(\Delta k)\big)}\Bigg|_{\Delta k \to 0} \qquad (2.1)$$

Where B is the normalization constant, n_0 is the average refractive index of the weakly disordered medium, k is the wavenumber $(k = 2\pi/\lambda)$, and $(\Delta k)^2/ln(C(\Delta k))$ is obtained by performing a linear fit of $ln(C(\Delta k))$ vs $(\Delta k)^2$.

2.2.3 Tissue microarrays (TMA) samples

TMA is a rapidly growing commercially available tissue sample that consists of generally numerous different cases of 5µm thick tissue cores in diameter 1.5mm placed on the same glass slide for simultaneous analysis. These paraffin-embedded TMA samples allow the high-throughput analysis of tissue samples since different cases of samples have exact experimental conditions and batches of reagents. TMAs are therefore scientific, cost-efficient, and offer an unprecedented degree of standardization for the conduction of an experiment such as optical imaging [69].

Here, using the PWS, we quantify the structural properties of paraffin-embedded TMAs from US Biomax of the pancreas (T142b), breast (BR248a), colon (T054c), and prostate (T191a) cancer samples, due to progressive carcinogenesis. Each TMA consists of different cores of normal, stage I, stage II, and stage III cancer tissue samples. Different cores of each TMAs are from individual patients of varying ages and sex. However, for each stage of each cancer, at least two different cores of the same age and sex were analyzed to calculate the degree of structural disorder.

2.3 PWS result of structural disorder and discussions

To develop a standardized diagnostic clinical research test for early and effective detection of cancer stages of varying types of the deadliest cancers, the structural alterations were quantified using a finer focusing PWS technique of TMAs. Here, the degree of disorder strength (L_d) for different stages of pancreatic, breast, colon, and prostate cancer TMAs were computed and compared. The results show that structural alterations increase with the progression of cancer stages in each type of progressive cancer. Since the disorder strength (L_d) is the product of the variance and spatial correlation length of the refractive index fluctuations, these results indicate that the progression of cancer increases more mass rearrangement/accumulations in the tissue results in increasing the refractive index spatial fluctuations increasing the L_d. In addition to the earlier findings, this work explores the application of the developed, highly sensitive PWS technique to detect the nanoscale fluctuations in paraffin-embedded TMA tissue samples of four different deadly cancers.

For each type of cancer TMAs: *pancreatic, breast, colon,* and *prostate* tissue spectroscopic images were recorded in the visible range (450-700nm) of light from three different cores of the same type. From each core tissue sample, at least 5 different realizations were made for the PWS analysis. Using this powerful spectroscopic technique, the pixel-wise refractive index fluctuations of tissue were computed and first represented in the 2D L_d map/image, averaged over the depth of the sample. Then, the ensemble average and standard deviation (*std*) of the disorder strength (L_d) were computed and presented in a bar graph for all cancerous TMAs studied.

2.3.1 Pancreatic cancer (PC) TMA samples

Pancreatic cancer is a lethal condition worldwide due to poor outcomes and a rising incidence rate. It is the 3rd leading cause of cancer deaths in the US common in both men and women and often presents at an advanced stage which contributes to a poor five-year survival rate [70]. Because of its physical orientation and lack of early symptoms, a better understanding of the symptoms associated with PC and its risk factor is essential to both health professionals and individuals. Therefore, we focus our research with added finer focusing on the existing PWS technique for the early diagnosis and to understand the structural properties of pancreatic tissue with progressive carcinogenesis using TMA tissue samples. The results show that mass density or refractive index fluctuations increase with the increase in the PC stage. Fig 2.2. (a)-(b) and (a')-(b') are the representative bright-field and their corresponding L_d images of normal and stage III PC tissue. The L_d map, which is a 2D image average along the z-axis represents the refractive index fluctuations at that point. The L_d map shows stage III pancreatic cancer sample has more red spots which indicate higher refractive index fluctuations in the color map. Further, the average and *std* of the degree of disorder strength were calculated and represented in the bar graph, Fig. 2.2. (c)-(d). Both the average and *std* of L_d value increase from normal, to stage I, stage II, stage III with a significant difference (Students t-test $p\text{-values} < 0.001$). This result, therefore, suggests that the developed finer focusing PWS technique is sensitive enough to detect nanoscale changes in refractive index fluctuation and to distinguish the different stages of cancer in paraffin-embedded pancreatic TMA samples.

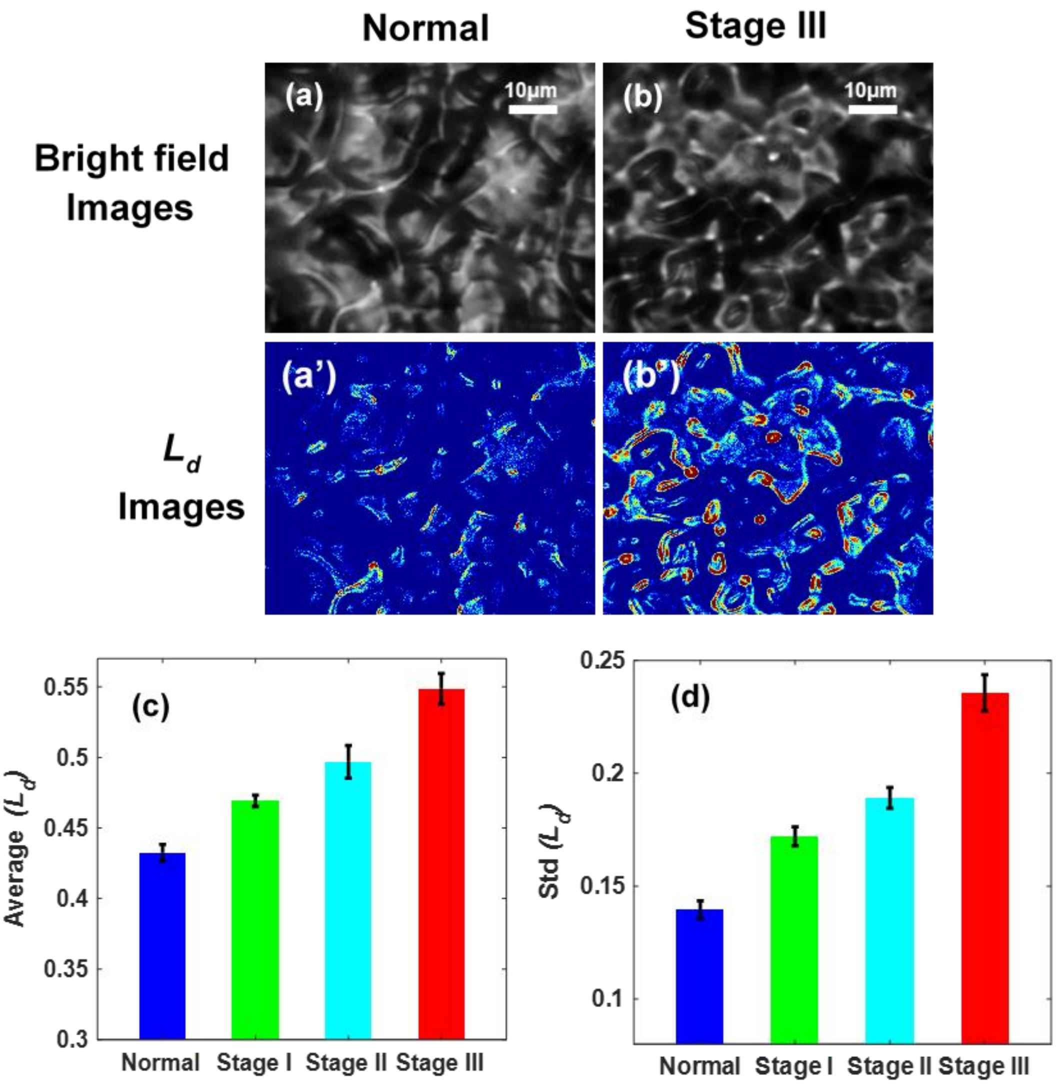

Figure 2.2 PWS study of pancreatic cancer TMA samples.

(a) and (b) are the representative bright-field images of normal and stage III PC TMA tissue while (a') and (b') are their corresponding L_d images. (c) and (d) are the bar graph representation of the average and *std* of disorder strength (L_d) for normal and different stages of PC TMA. The PWS analysis of TMA tissues shows that both the average and *std* of L_d value increase from the normal to higher stages of PC. In reference to the normal, the std of L_d value of cancer stage I is 23%, stage II is 36%, stage III is 69% higher (Student's t-test $p\text{-}values < 0.001$, n=15).

2.3.2 Breast cancer (BC) TMA samples

Breast cancer is the most common cancer in women and a challenging cause of cancer death in the world. This metastatic cancer is transferable to different organs such as the bones, lungs, liver, and brain with almost incurability. Early diagnosis of BC is only the best method of prevention. Although the five-year relative survival rate of an early detected BC patient is more than 80% nowadays, oncologists and scientists are still struggling to develop a technique that can identify early symptoms and distinguish the nanoscale structural changes in breast cancer cells/tissue [71]. BC is the second leading cause of cancer death in women in the US. In the existing scenario, the finer focusing PWS technique was applied to characterize the structural properties of BC TMAs tissue at the nanoscale level due to progressive carcinogenesis. The result shows that the structural disorder (L_d) increases from the normal to stage III significantly as shown in Fig. 2.3. The representative L_d images Fig. 2.3. (a')-(b') for normal and stage III cancer were presented which shows that the refractive index or mass density fluctuations are higher in stage III BC. Also, the average and *std* of L_d value increase significantly from stage I, stage II, to stage III about the normal with Student's t-test $p\text{-}values < 0.001$ as represented in Fig. 2.3 (c)-(d). This increase in the degree of disordered strength due to progressive carcinogenesis indicates that the refractive index fluctuations increase with the stages of cancer which was successfully detected by finer focusing PWS using TMAs.

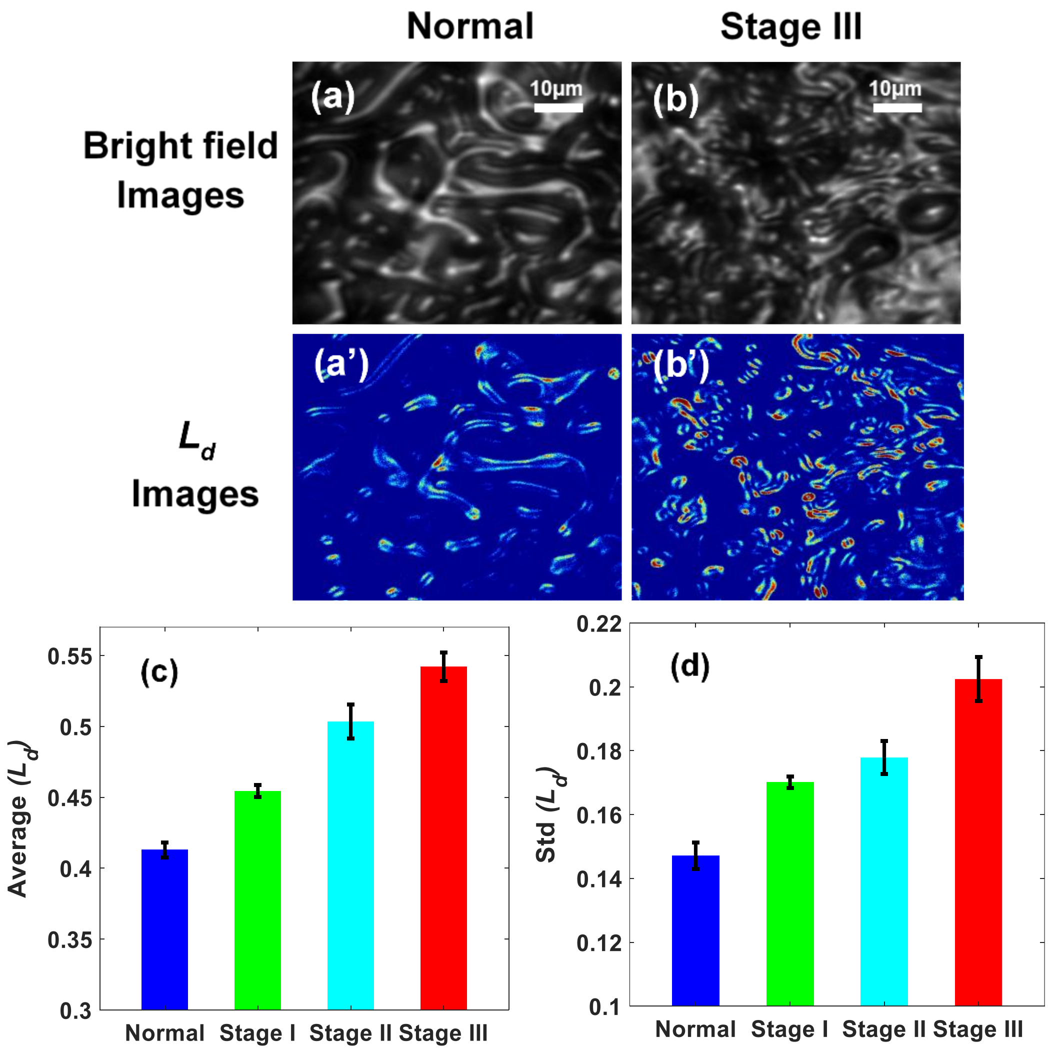

Figure 2.3 PWS study of breast cancer TMA samples.

(a) and (b) are the bright-field images while (a') and (b') are the L_d images of the normal and stage III BC of TMA tissue, respectively. (c) and (d) are the bar graphs of average and *std* of disorder strength (L_d)for the normal and different stages of BC TMA samples. The PWS result using TMA tissue shows that both the average and *std* of L_d value increases from normal to higher stages of cancer tissue. In reference to the normal, the std of L_d value of cancer stage I is 16%, stage II is 21%, stage III is 38% higher (Student's t-test *p-values* < 0.001, n=15).

2.3.3 Colon cancer (CC) TMA samples

Colorectal cancer is predominant cancer accounting for approximately 10% of all cancer mortality in the world. Colorectal cancer is the 3rd leading cause of cancer-related death in men and women in the US. Population aging, improper dietary habits, smoking, low physical activity, and obesity are the main reasons for annually increasing metastatic CC cases [72,73]. Until modern times, laparoscopy surgery has played a vital role in controlling or treatment for primary and metastatic colorectal cancer. Despite advances in surgical and medical therapies, the long survival rate of colorectal patients has changed very little in recent times. This demands standardization in screening or imaging techniques to detect the early stages of CC. Therefore, to understand the structural changes in cells/tissue at the nanoscale level due to progressive CC we apply the PWS technique to distinguish different stages of CC TMAs tissues. The averages and *std* of the degree of disorder strength (L_d) increase from the normal to stage III with a significant difference (Student's t-test $p\text{-values} < 0.005$). As cancer increases, mass density accumulation increases which in turn increases the change in refractive index fluctuations resulting in increased L_d value for higher cancer stages. In addition to this, the L_d images were also constructed to visualize how the refractive index fluctuations increase with the increase in cancer stages in colon TMAs as shown in Fig. 2.4. (a')-(b'). The bar graphs show that the average and *std* of L_d value increases in stage I, stage II, and stage III cancer tissues compared to normal, and this result is presented in Fig. 2.4 (c)-(d).

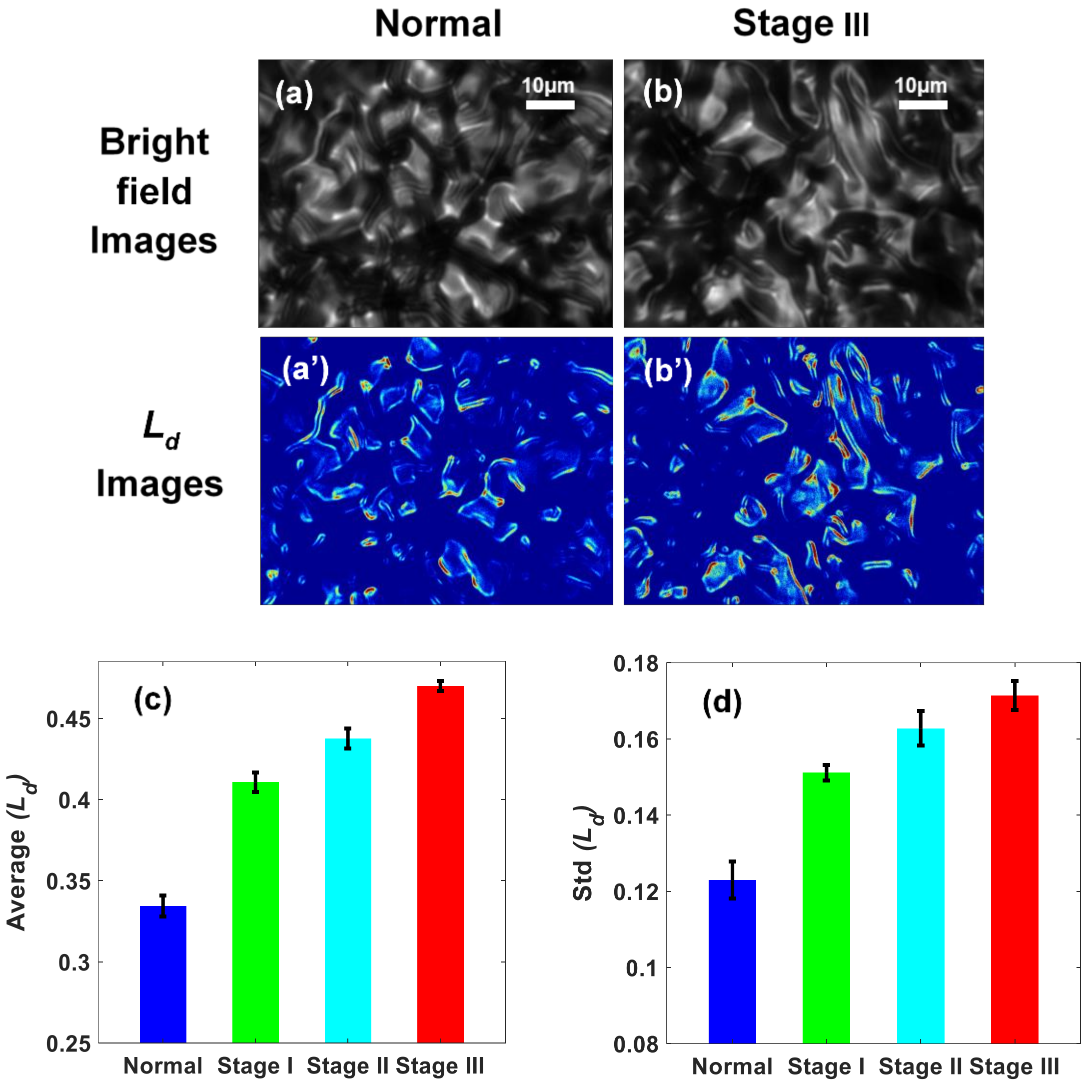

Figure 2.4 PWS study of colon cancer TMA samples.

(a) and (b) are the bright-field images of the normal and stage III CC TMA tissue and (a') and (b') are their respective L_d Images. (c) and (d) bar graphs of the average and *std* of disorder strength (L_d) for the normal and different stages of CC TMA samples. The PWS result of TMA tissue shows that the average and *std* of L_d value increases from normal to higher stages of colon cancer. In reference to the normal, the std of L_d value of cancer stage I is 23%, stage II is 32%, stage III is 40% higher (Student's t-test *p-values* < 0.001, n=15).

2.3.4 Prostate cancer (PC) TMA samples

Prostate cancer is common cancer among men, especially elderly ones, and 1 in 9 men will have prostate cancer during their lifespan. Ceasing to smoke, proper exercise, and weight control are good health practices that may reduce the risk of developing PC. Although remarkable progress has been achieved on characterizing risk factors and identifying therapeutic options. Screening for and diagnosing the early stages of PC is still one of the most challenging issues across the globe in medicine [74,75]. At this point, the study of structural properties of PC tissue at the nanoscale level using a precise volume scattering technique, PWS of TMA tissue could help to characterize the structural change in their stage. The results obtained using the PWS technique to study the commercially available prostate TMA is presented in Fig 2.5. The representative L_d images i.e. Fig. 2.5 (a')-(b') show that stage III Prostate cancer has more red spots in the color map because it has higher mass density or refractive index fluctuations than normal. To quantify the structural abnormalities, the average and *std* of the degree of disorder strength (L_d) were computed and represented in the bar graph, as shown in Fig. 2.5 (c)-(d). As can be seen from the figure, both the average and *std* of L_d value increase in stage I, stage II, and stage III compared to normal. This increase in the L_d is due to the increase in refractive index fluctuations with the increase in the stages of PC.

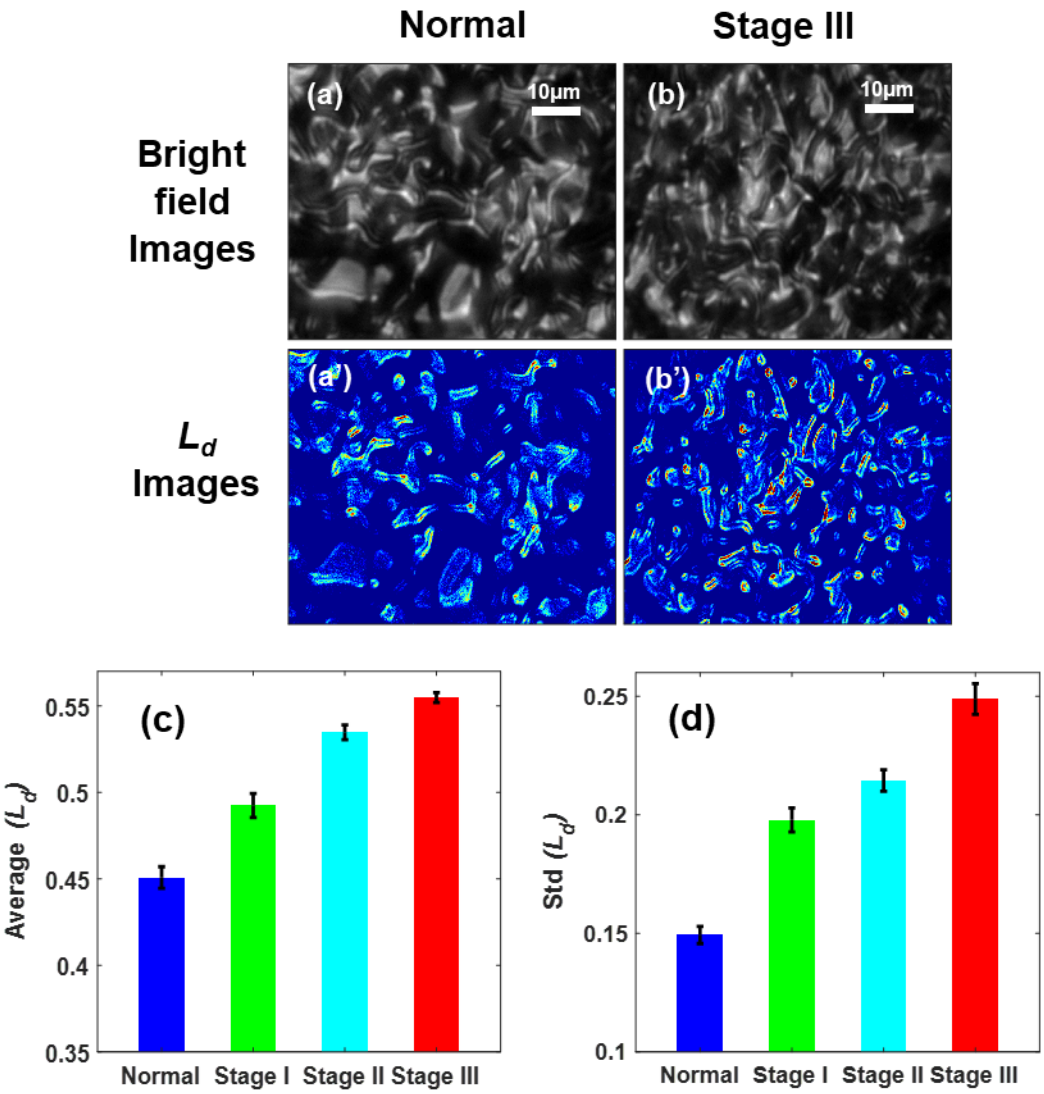

Figure 2.5 PWS study of prostate cancer TMA samples.

(a) and (b) are the representative bright-field images of the normal and stage III PC TMA tissue while (a') and (b') are their corresponding L_d images. (c) and (d) are bar graphs of the average and *std* of disorder strength (L_d) for the normal and different stages of PC TMA samples. The PWS analysis of TMA tissue show both the average and *std* L_d value increases from the normal to higher stages of cancer tissue. In reference to the normal, the std L_d value of cancer stage I is 32%, stage II is 46%, and stage III is 65% higher (Student's t-test $p\text{-values} < 0.001$, n=15).

2.4 Conclusions

In summary, as an alternative method in cancer diagnostic research of applying the mesoscopic physics-based PWS technique using commercially available TMAs has been reported. This technique makes the use of the recently developed finer focusing PWS technique which can scatter precise volume to detect the nanoscale structural changes in paraffin-embedded tissue and distinguishes the stages of four different cancer cases. To validate the purpose method, the degree of disorder strength (L_d) of different tissue with the progression of cancer stages of different TMAs are quantified. The PWS results obtained for some of the deadliest cancer TMAs: *pancreatic*, *breast*, *colon*, and *prostate* show that the average and *std* disorder strength (L_d) increases significantly as cancer progresses through the different stages. However, the more prominent changes were found in the *std* of the degree of L_d value for all case studies. The results obtained by the purposed method were following the earlier studies [17,59] and therefore, the L_d parameter acts as a potential biomarker to distinguish and standardize the cancer stages which seems almost impractical. In addition to this, the use of the PWS technique and commercially available TMAs could provide easy and clinically accessible samples to study the drug effect in cancer treatment. In particular, this finding invites the research communities to work with a common goal to standardize early and accurate detection of the cancer stages of different types of deadly cancer cases. Further validation in distinguishing the stages of cancer of TMA tissue can be performed using other quantitative approaches such as fractal, IPR, etc. [62,76,77]. Lastly, the flexibility provided using the spectroscopic technique such as PWS in commercially available TMA samples to distinguish the early to late stages of cancer cases opens a broad way to explore and generalize the structural changes in progressive cancer for effective diagnosis and drug treatment in the future.

CHAPTER III

OPTICAL QUANTIFICATION OF STRUCTURAL PROPERTIES OF TUMOR TISSUES GENERATED BY XENOGRAFTING OF CANCER CELLS USING PWS

This chapter is adapted from the author’s published article with copyright permission from the publisher. Ref. [53] P. Adhikari et. al., “Optical detection of the structural properties of tumor tissue generated by xenografting of drug-sensitive and drug-resistant cancer cells using partial wave spectroscopy (PWS)”. ***Biomedical Optics Express***, BOE. 2019 Dec 1;10(12):6422–31. The PWS technique has been successfully used for the detection of cancer stages by probing nanoscale structural alterations in cells/tissues as discussed in Chapter II. However, the development of drug-resistant cancer cells/tissues during chemotherapy is a major challenge in cancer treatment, especially to know the drug is working or not. In this chapter, using a mouse model and developed PWS technique, the structural properties of tumor tissues grown in 3D structures by xenografting drug-resistant and drug-sensitive human prostate cancer cells having 2D structures are studied. In particular, we probe the difference in the structural disorder of cells grows on 2D slides or cells grown in a 3D environment inside the body. This may provide us an indirect way to study the effects of drugs on the cancer cells/tissues. The promising aspect of the proposed study to establish insight into advancing the understanding of the physical state and drug effectiveness on cancerous cells/tissues at the nanoscale level is explored.

3.1 Introduction

Elastic light scattering, especially in the visible range of light, is an important method for probing structural morphologies of the biological cells/tissues. It is now shown that probing the structural alteration at the nano to submicron scales enables the prediction of several properties of the physical conditions of cells/tissues in normal and disease/abnormal states. Recent studies have shown that the progression of carcinogenesis results in nanoscale structural alterations due to the rearrangement of the basic building blocks, in particular, macromolecular components inside the cells. These nanoscale structural alterations, in terms of the degree of disorder strength, have been shown as an important biomarker in the determination of cancer stages [22,23]. However, the histopathological examinations of cells/tissues, conventionally, are based on a large degree of changes in the cellular architecture, mainly nuclear size, during the disease process [78–81]. Also, the sensitivity of the existing pathological optical microscopic techniques used to detect such nanoscale alterations is restricted by the diffraction-limited resolution (>~200nm).

A recently introduced spectroscopic microscopy technique, partial wave spectroscopy (PWS), combines the interdisciplinary approaches of mesoscopic condensed matter physics and microscopic imaging, to quantify the degree of change of the nanoscale structural disorder of weakly disorder medium like biological cells/tissues [15–17,59,60,67]. The statistical quantifications of the reflected intensities due to the nanoscale refractive index fluctuations of the biological cells/tissues are carried out using the PWS analysis. In the PWS technique, the backscattering signals from thin weakly disordered cell/tissue samples are divided into many parallel scattering quasi-one-dimensional reflections to calculate the structural disorder strength of the samples. Further, the spatial variation of the intracellular components such as DNA, RNA, lipids, and extracellular matrices (ECM) gives rise to spatial mass density fluctuations in terms of the refractive index fluctuations of the cells/tissues. This spatial refractive index fluctuations can be quantified in terms of the degree of structural disorder. The degree of structural disorder parameter L_d, called the disorder strength, can quantify nanoscale alterations and distinguish different cancer stages with higher accuracy. For a quasi-1D approximation, the disorder strength can be expressed as $L_d = dn^2 \times l_c$, where dn is the standard deviation (*std*) of the onsite refractive index fluctuations $dn(r)$ and l_c is its spatial correlation length. The efficiency and application of the PWS technique in measuring nanoscale alterations, i.e. the L_d parameter, to diagnose diseases like cancer has been developed and explored [15,17,59,60,67,82]. The detection of molecular-specific structural disorder in submicron scales of control and cancer/abnormal cell nuclei are also studied by the light localization technique using confocal microscopy, which supports the increase in the molecular-specific structural disorder in progressive cancer [38,83–85].

After the diagnosis of cancer, the cancer patient generally goes through chemotherapy drug treatment. Resistance to cancer cells/tissues to chemotherapy drugs is one of the obstacles in cancer treatment. Recently, the PWS technique was successfully used to study the effect of chemotherapy drugs on prostate cancer cell lines and to quantitatively measure the structural disorder strength of drug-sensitive and drug-resistant prostate cancerous cells [59]. The results show that the chemo-resistant cells have a higher degree of structural disorder than that of the chemo-sensitive cells. Drug-resistant cancerous cells are able to survive chemotherapy drug treatment, as the different mechanisms responsible for drug resistance and the development of different morphological structures. These different morphological structures in drug-resistant cancer cells may be due to the rearrangements of macromolecules, increase in the sizes of membrane pores, architectural differences of the cytoskeletal network, etc., which result in increasing aggressiveness and the disorder strength.

Prostate cancer is one of the most prevalent types of cancer with one of the highest male mortality rates in the USA. The American Cancer Society (ACS) estimates about 174,650 new cases of prostate cancer will appear and account for a total of 31,620 deaths for 2019. Across the globe, the statistical data on prostate cancer suggests that among every 9 men, one individual will develop this cancer during his lifespan. Therefore, it is necessary to explore early and effective diagnosis and treatment methods for prostate cancer. At present, chemotherapy is the only way to treat metastasized prostate cancer, however, it is often found ineffective due to an individual patient's chemo-resistance that leads to tumor progression [59,86–90]. The PWS studies of cancer cell lines have shown some promising success in distinguishing the hierarchy and drug effectiveness based on the measurement of the biomarker, the structural disorder strength L_d [59].

These PWS studies of drug resistance cells for different cell lines were mainly focused on cancer cells that were grown in 2D on glass slides. However, in reality, a metastasizing cancer cell grows into a tumor with a 3D structure when grown within the body, and these tumor cells may have different structural properties due to their grown 3D tissue structures. This leads to a demand for the development and quantitative characterization of 3D tumor tissues that are grown from drug-sensitive and drug-resistant cancer cells. This could establish a correlation between isolated cells of 2D structure which is grown into tissue in 3D structure, based on the structural disorder. In particular, we want to verify the structural properties of 3D tissues generated by xenografting of cancer cells, and to understand any relationship between the 3D tissue structures with their original 2D cell structures, using the L_d parameter. Human cancer cases have been studied by innumerable murine methods and the determinants responsible for malignant transformation, invasion, and metastasis, as well as the examination of the response to therapy, is investigated with the aid of these murine models. Xenografting of human cancer cells in a mouse model is one of the most extensively used models to study the development of tumors from cells [91,92]. Cancerous human cells were subcutaneously injected in immunocompromised mice. Based on the number of cells injected, the tumors will develop over 1-8 weeks and reaction to the proper therapeutic regimes can be studied *in vivo* [91,93] or *ex vivo*. At the same time, the structural properties of growing xenografted cancer cells are not well studied.

In this work, using a further engineered PWS technique, we explore the structural properties of the 3D tumor tissues obtained by xenografting drug-sensitive and drug-resistant human prostate cancer cells' 2D structure using a mouse model. We study structural properties of tissues obtained by xenografting two types of human prostate cancer (PC) cell lines, namely DU145 and PC3, whose drug-resistant and drug-sensitive structural properties were studied earlier by the PWS technique [59]. From the results, a correlation between the 3D structural disorder of tissues originally grown from chemotherapy drug-sensitive and drug-resistance cells and the original cells will be performed. Finally, we will also discuss the potential applications of the technique in cancer diagnostics.

3.2 Method

3.2.1 PWS experimental setup

We perform the structural disorder measurement using a recently developed partial wave spectroscopy (PWS) experimental technique, with added engineering of finer focusing as mentioned in Chapter I Section 2.1.1 [59,60,67]. The actual experimental PWS setup developed in the Bionophotonics laboratory is as shown in Fig.3.1. It consists of a Xenon Lamp, a source of stable broadband white light to illuminate tissue samples of micron thickness using Kohler Illumination. This collimated light from the 4f combination is focused on the sample through the objective. The use of a highly sensitive 3D electronic motorized stage (100nm on Z-axis and 40nm on the X-Y axis) provides the finer focusing of the sample within the working distance of the objective. Then the backscattered signal gets reflected by a dichroic mirror towards the detector through a liquid crystal tunable filter (LCTF) coupled with CCD.

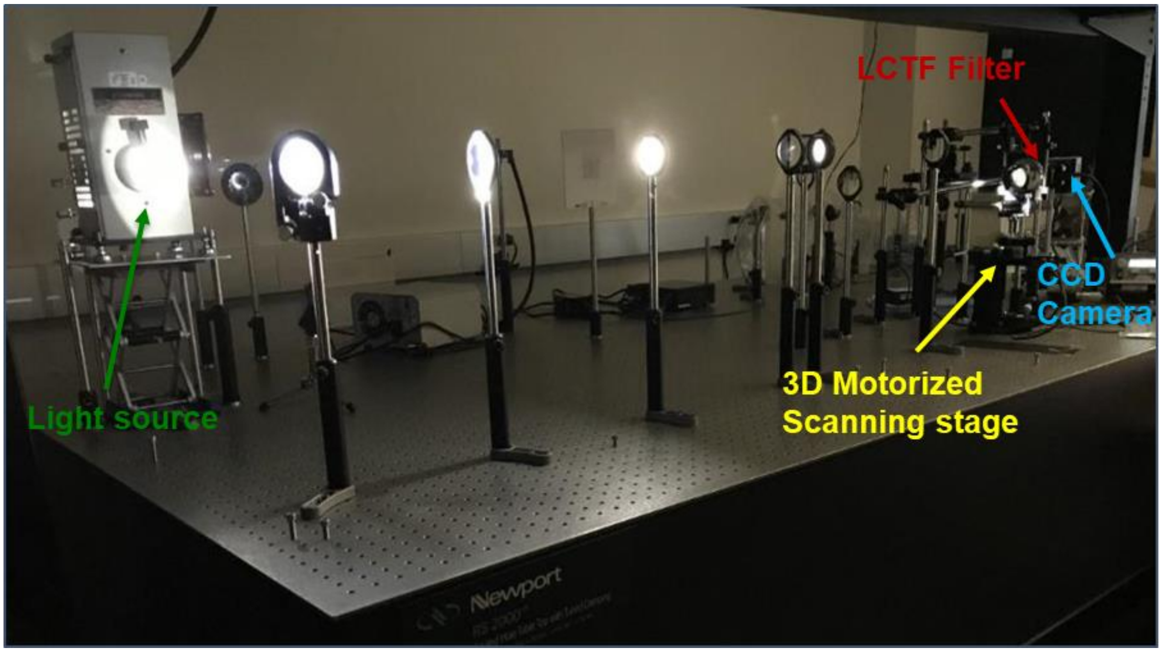

Figure 3.1 Actual PWS experimental setup developed in Bionanophotonics laboratory, MSU.

The table-top optical instrumentation of PWS setup. It consists of a board band white light source collimated through the 4f combination of the lenses. The nanoscale sensitive 3D motorized scanning stage is used for the precise focusing of the sample to capture the spectroscopic image using CCD.

3.2.2 Calculation of the structural disorder or disorder strength (L_d)

The backscattered images are recorded in the CCD camera at every wavelength *(λ)* at the spatial pixel position *(x,y)* in the wavelength range *450-700nm,* and the reflected data cube, *R(x,* *y;* λ*)*, is acquired by the PWS system. In a quasi-1D approximation, the collected backscattered data at each *(x,y)* from *R(x,y;*λ*)* is fitted with a polynomial of the 5th order. The fitted polynomial is then extracted from the signal to remove the systematic errors. In the next step, the *R(k)* signal for each pixel position *(x,y)* is obtained after applying a 5th order low-pass Butterworth filter with a suitable normalized cutoff frequency to remove the high-frequency noise components from the reflected signals of micron size samples. Here, calibration of the system is done by matching the reflected intensity pattern using a non-disordered system, NIST-traceable microspheres with the reflected signal from a thin film slab model.

The fluctuating part of reflection signals *R(x,y;*λ*)* arises due to the multiple interferences of the photons reflected from the disordered medium. Since in a quasi-1D approximation, the sample is virtually divided into many parallel channels within the diffraction-limited transverse size, and the backscattered signals propagating along the 1D trajectories are collected. The statistical properties of nanoarchitecture are quantified at the nanoscale level by analyzing the fluctuating part of the reflected intensities. The refractive index fluctuation information is collected from these spectral fluctuations originated from the multiple scattering of the sample at any length scale below the diffraction limit. The degree of structural disorder L_d can be derived from the *rms* value of the reflection intensity $<R(k)>_{rms}$ and the spectral auto-correlation decay of the reflection intensity $C(\Delta k)$ ratio. That means, for a given pixel at position *(x,y)*, the degree of structural disorder is expressed as shown in Chapter I Section 1.1.2 [16,17,59,60,67]:

$$L_d = \frac{Bn_0^2\langle R\rangle_{rms}}{2k^2}\frac{(\Delta k)^2}{-\ln\big(C(\Delta k)\big)}\Big|_{\Delta k\to 0} \tag{3.1}$$

where B is the normalization constant, n_0 average refractive index of the biological cells, and k is the wavenumber ($k = 2\pi/\lambda$).

Therefore, the disorder strength quantifies the variability of the local density of intracellular material within the samples, and hence the average and standard deviation of the L_d values are calculated to characterize the structure of the system.

3.2.3 Sample preparation

Freshly collected prostate cancer (PC) cells from two different cell lines were used to develop a prostate xenograft, mouse model. For the generation of tumor xenograft mouse models, 6–8 weeks old male nude mice were implanted with PC3 (docetaxel-sensitive and docetaxel-resistant) and DU145 (docetaxel-sensitive and docetaxel-resistant) human PC cell samples (2×10^6 cells per mice), by subcutaneously injections. After tumors reached beyond the critical size of 1000 mm^3, they were excised from euthanized mice. The excised tumors were further paraffin-embedded and sectioned using microtome in 4μm thickness and placed on glass slides. Further, these slides were processed for the antigen retrieval process as described previously [94]. The resultant tumor sections were subject to imaging studies.

3.3 Results

PWS detects the nanoscale structural alterations in the cells/tissues and can distinguish the different levels and effects of the drug in the tumorous cells/tissues [16]. Among the different types of cancer, prostate cancer is a major concern of public health at present because of its low survival rate. Further, drug-resistant cancer cells are a prominent problem currently in cancer treatment. Therefore, we focus our research to characterize the structure of tumor tissues generated by the xenografting of chemotherapy drug-sensitive and drug-resistant prostate cell lines, DU145, and PC3. For this, human drug-sensitive and drug-resistant prostate cancer cells were subcutaneously injected into mice and allowed to grow and achieve a tumor size of

~1000mm^3. After that, mice were euthanized, and tumors were excised then subsequently processed to 4 µm thick tumor sections on slides for PWS imaging analyses.

PWS experiments, as described earlier, were performed on xenografted prostate tumor tissues for each category on at least 3 different mice. All tumor tissue was obtained from different prostate cancer cell lines xenografted into mouse models. For each tissue sample, PWS experiments were performed on 7 different spots. In particular, for each category of a tumor, ~60 different spots are experimented with PWS and analyzed. The spectroscopic PWS experiments are performed in the wavelength range 450-700nm. The backscattered data matrix $R(x, y; \lambda)$ are imported and the disorder strength for each tissue is calculated using the PWS technique as described in section 3.2. The disorder strength is calculated as the product of the variance and the spatial correlation length of the refractive index fluctuations. The average and standard deviation of the disorder strength for each category are calculated in order to understand the physical properties of a tumor developed as a 3D structure from a cell. The detailed PWS analysis of a tumor obtained from a xenografted model of drug-sensitive and drug-resistant cell lines DU145 and PC3 are explained below:

3.3.1 Structural disorder in the xenografted DU145 tumor tissue type

In Fig. 3.2, the PWS analysis of tumor tissues obtained from xenografting drug-sensitive and drug-resistant prostate human cancer cell lines of DU145 type are shown. From the PWS experiment $R(x,y,\lambda)$ data matrixes were obtained. At every pixel point (x,y), $R(k)_{rms}$ value and corresponding $C(\Delta k)$ were obtained, and from these two values, and the L_d value was calculated using Eq.(2.1). The bright-field images, as shown in Fig. 3.2(a)-(b), the thin tissue samples developed from drug-sensitive and drug-resistant cancer cell lines appear indistinguishable, whereas the L_d images are noticeably distinguishable. The red spots in the L_d image represent a higher disorder strength, i.e. the L_d value of that pixel. It can be seen in the bar graphs that there is an increase in the degree of structural disorder of tumor tissue generated from xenografting drug-resistant cancer cells, compared to the tissues obtained from xenografting drug-sensitive cancer cells. The average L_d value of a tumor obtained from a drug-resistant cancer cell line is 9% higher than the tumor obtained from a drug-sensitive cancer cell line and the standard deviation $std(L_d)$ is 8% higher. This result is in strong agreement with the disorder strength calculated for drug-resistant and drug-sensitive cell lines earlier [59]. The disorder strength of the prostate cancer cell line calculated using PWS has shown that the average and standard deviation of L_d value is higher in drug-resistant cells compared to the drug-sensitive for DU145 type cells. The results confirm that the xenografted tissue structures also have similar trends to original cell structures.

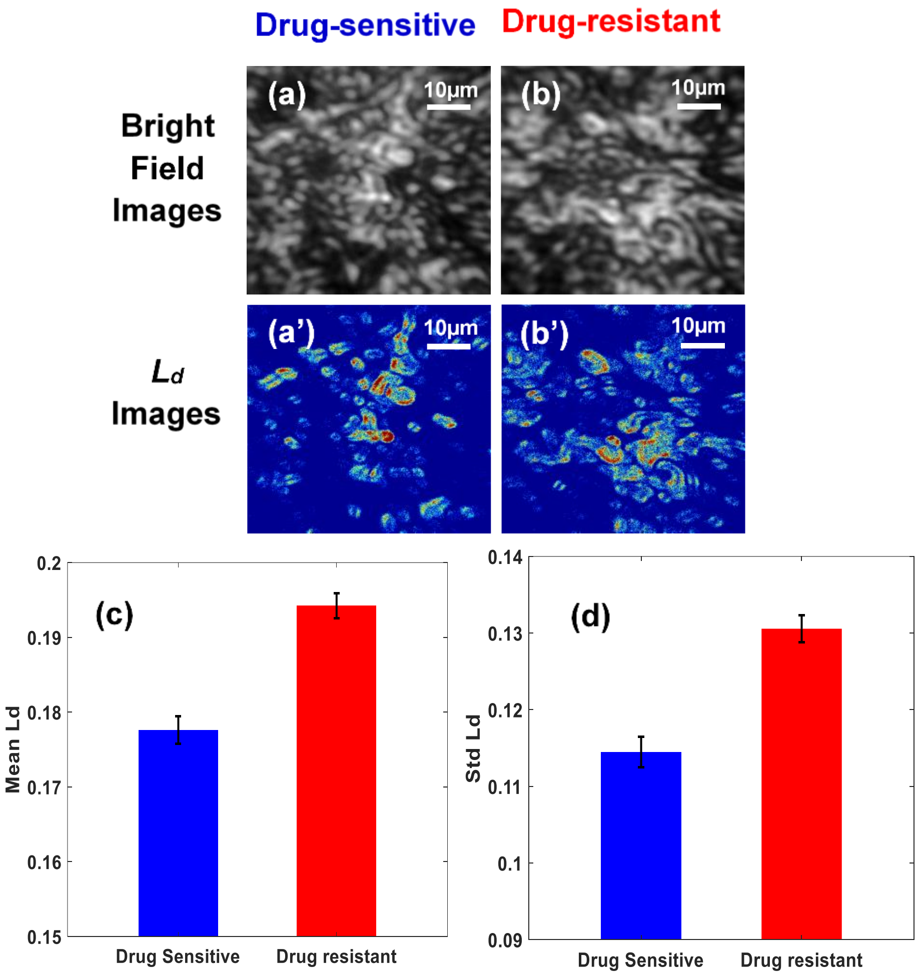

Figure 3.2 The structural abnormalities in tumor xenografted from DU145 cells lines.

(a) and (b) are the bright-field images while (a') and (b') are the disorder strength or L_d images of tissue obtained by xenografting drug-sensitive and drug-resistant PC cells line of DU145 type respectively. (c) and (d) are the graphical representation of the mean and standard deviation of L_d of the xenografted tumor, respectively. Result shows a 9% higher mean L_d and 8% increase in the *std* L_d in a tumor developed from drug-resistant PC DU145 type cells line than the drug-sensitive cells. P-values < 0.05.

3.3.2 Structural disorder in the xenografted PC3 tumor tissue type

Fig 3.3 (a)-(b) shows the bright field and L_d images of tumor tissues originated from drug-sensitive and drug-resistant PC PC3 type cells. Based on the intrinsic properties of the tissue, the disorder strength L_d at each pixel of the individual tissue image is calculated and represented by 2D color maps. In the color map, red spots correspond to the higher structural disorder strength present in the thin tissue structure (averaged along the z-direction of the sample). The bar graphs, 3.3(c) and (d) are the representation of the average and standard deviation of L_d values with the standard error bars. The result shows a 12% difference in the average local disorder strength L_d and a 15% difference in the *std* (L_d), between tumors obtained from drug-sensitive and drug-resistant cell lines. The increment in the mean and standard deviation of L_d for tissues collected by the xenografting of drug-resistant PC PC3 cells compared to the drug-sensitive PC PC3 cells are consistent with the original cell structures. It is clear from the plots that the disorder strength increases from drug-sensitive to drug-resistant xenografted tumor tissues. Earlier results using PWS analysis show that PC PC3 cells are more aggressive than other cell lines and in the same way drug-resistant PC cell lines have higher disorder strength than drug-sensitive cells. Figs. 3.2 and 3.3 show the results obtained using xenografted tissue samples also have the same kind of disorder strength hierarchy as that of the original PC cells. In particular, a comparatively higher structural disorder strength L_d for tumors obtained from drug-resistant PC PC3 cell lines than PC DU145 cell lines are in strong agreement with their original PC cell line disorder strength. This confirms that the degree of disorder strength L_d can be used as a marker to detect the cancer stages or drug effects using 3D cancer tissue structure, similar to that of a cell line that is easy to study.

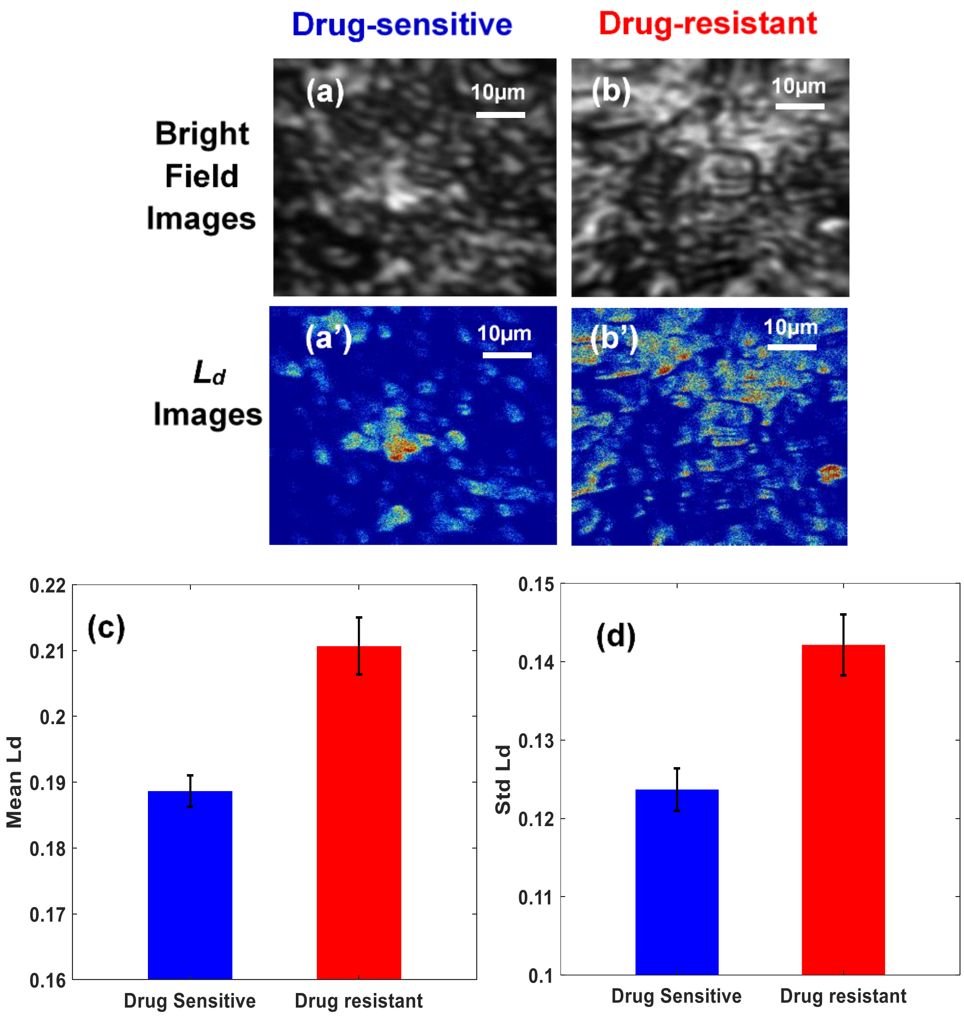

Figure 3.3 Structural abnormalities in tumor xenografted from PC3 cells lines.

(a) and (b) are the bright-field images and (a') and (b') are the disorder strength or L_d images of tissues obtained by xenografting of drug-sensitive and drug-resistant PC cells line of PC3 type respectively. (c) and (d) are the bar graph representation of the mean and standard deviation of L_d of a tumor, respectively. Result shows a 12% higher mean L_d and 15% increase in the *std* L_d in tumors developed from drug-resistant PC PC3 type cells line-than the drug-sensitive cells. P-values < 0.05.

3.4 Conclusions

The results indicate that tumor tissues grown by xenografting of PC cells resistant to docetaxel have a higher disorder strength L_d than the same tissues from drug-sensitive PC cells. Since the disorder strength increases with the increase in the level of tumorigenicity, which implies chemotherapy-resistant cells are more aggressive than drug-sensitive cancerous cells. Cells from the prostate or any other cancerous region that survived through drug exposure are more aggressive and develop with the cell line's hierarchy as PC3 > DU145 [59]. As an application of the developed finer focusing PWS technique, we have studied the structural alteration in the xenografted tissue morphology that is grown in a 3D environment from single cells that mainly have 2D structures. The results show metastasize isolated 2D cancer cells grown to 3D tumors in the body have similar structures and characteristics. The PWS analysis of 3D tissue slices confirm xenografted tissues from drug-resistant tumors have a higher average and standard deviation of disorder strength (L_d) than the drug-sensitive counterparts. Also, the obtained results follow a similar hierarchy of the cell lines that are studied earlier, reported in ref [59].

Probable cause of structural properties of drug resistance cells/tissues and higher structural disorder (L_d): Studies have shown that the progress of cancer disturbs the regular growth as well as the structure of cells/tissues. Further, cells/tissues that survive through the chemotherapy adapt themselves to the situation and develop different morphological structures resulting in higher mass density fluctuation due to the rearrangement of macromolecules, larger pore sizes, changes in cytoskeleton nanoarchitecture, etc. This results in a higher structural alteration in drug-resistant PC cells than drug-sensitive ones. The different mechanisms such as tumor-derived exosomes biogenesis and composition, DNA and histone damage/repair, anti-cancerous multidrug inactivation, alteration in drug targets treatment, heterogeneity in cancerous cells/tissues, death inhibition of cells/tissue, epithelial-mesenchymal transition, and metastasis, etc. [95–99] are making the cancerous cells/tissues drug-resistant [59]. Xenografted tumor tissues that are obtained using cells from drug-resistant and drug-sensitive PC cell lines, main the same types of structural hierarchy properties when they are grown into 3D structures. This supports a strong correlation in structural properties in 2D and 3D structures.

Applications of the developed technique for cancer treatment: The PWS study of xenografted tissues obtained from drug-sensitive and drug-resistant PC cells line could establish a new insight into advancing the understanding of the physical state and drug effectiveness on cancerous cells/tissues at the nanoscale level, by knowing their structural properties. The xenografted tissue structure replicating the structural properties of cancer cells explained statistically in terms of the disorder strength L_d parameter could be a reliable, easy, and quantitative approach to diagnose chemoresistance. This result seeks the potential application to monitor the effect of chemotherapy drugs on cancerous tissues and to study the different levels of tumorigenicity which can be obtained both, *in-vitro* and *in-vivo* methods. In summary, this method will help in understanding the drug-resistant and drug-sensitive cells/tissues and their different stages in the body, by examining their structural disorder properties.

CHAPTER IV

PHOTONICS TECHNIQUE TO QUANTIFY PROBIOTICS EFFECT ON CHRONIC ALCOHOLIC BRAIN CELLS VIA MOLECULAR-SPECIFIC CONFOCAL-IPR

This chapter is adapted from the author's published article with copyright permission from the publisher. Ref [58] P. Adhikari et al., "Photonics study of probiotics treatment on brain cells exposed to chronic alcoholism using molecular specific light localization properties via confocal imaging". ***arXive. 1912.11777, 2019.*** And Ref [59] P. Adhikari, et al., "Quantification of light localization properties to study the effect of probiotic on chronic alcoholic brain cells via confocal imaging," in ***Imaging, Manipulation, and Analysis of Biomolecules, Cells, and Tissues XIX (SPIE), 2021, Vol. 11647, p. 1164716.***

Recently IPR technique using confocal images has shown success in distinguishing molecular-specific structural alterations targeting DNA to quantify cancer, radiation effect, or any other abnormalities in cells/tissues [38,100]. The advantage of the IPR technique relative to the PWS technique is that we can probe structures of an isolated cell within the tissue without disturbing them by confocal imaging, which is not possible using the PWS technique. PWS technique provides statistical properties of the region averaged over light propagation direction and it cannot probe separately a cell that is situated inside the tissue. It was found that chronic alcoholism introduces abnormalities in brain cells/tissue that result in behavioral and psychological disorders. On the other hand, probiotics such as *Lactobacillus Plantarum* enhances brain functions in chronic alcoholism. Therefore, in this chapter, using the close scattering based on light localization technique, IPR combined with confocal imaging we probe the molecular specific structural alterations present in chronic alcoholic brain cells with or without probiotic treatments in a mouse model. The potential application of this novel approach to diagnose the alcohol effect and probiotic treatment in the alcoholic brain is explored.

4.1 Introduction

Photons/light are an important probe for the characterization of the structural properties of biological cells. It is known that the structural properties of cells and tissues change with the progress of disease or abnormalities such as cancer, stress, drugs, etc. Cells and tissue are weakly disordered dielectric media; therefore, their structure and any change in the structural properties can be characterized using light, which happens at the length scale of micron size. The light probing is generally done by measuring the scattering signals and quantifying the optical parameters of the samples. Different types of structural changes can happen in a cell with the progression of diseases such as carcinogenesis or due to the effect of drugs [23,22,58]. These changes in a cell may range from bulk structural change to nanoscale molecular-specific structural alterations. The nanoscale structural changes in cells and tissues due to diseases or abnormalities are associated with the molecular-specific structural alteration and, in turn, its mass density fluctuations. Recently, the refractive index fluctuations are experimentally measured to quantify the structural abnormalities in cells and tissues using the recently introduced mesoscopic physics-based sensitive imaging technique called, the PWS [16,17,58,60,67,68,101]. Although the microscopic changes in a cell/nucleus have been studied for a long time by probing structural properties, however, these changes appear almost at the advanced stages of diseases or abnormalities, which would be too late for treatment. At the same point, the PWS technique can probe full structural changes of a cell or tissue, and it was recognized that minuscule changes occur at the early stages of the diseases or abnormalities where the molecular specific nanoscale structural changes occur due to the rearrangements of the macromolecules present in a cell. Therefore, probing molecular-specific structural changes will be more efficient and important for the detection of abnormalities or disease progression in a cell. This is the primary interest of the present study. Therefore, we hypothesize that probing the molecular-specific structural changes can measure the physical state of cells/tissues and the organs. The concept of characterizing the molecular-specific structural alterations was introduced recently to quantify the nano to microscale changes in cells in abnormalities and has shown success in several studies [22,23,61,83]. The initial case studies ranging from cancer to abnormalities in brain cells due to chronic alcoholism have shown promising results in the characterization of the physical state of the cell [38,61,83,102].

Alcohol-related disorders and organ-specific damage are significant global concerns. Alcohol and its metabolites play a significant role in neuroinflammation, however, the existing evidence indicates that interactions at the Gut-Microbiome-Brain axis are a crucial part of the alcohol-related behavioral disorder [103,104]. Among the multidirectional alcohol interactions with the human body, initially, chronic alcoholism affects the brain from the cellular to the molecular level. It has been shown by TEM imaging that structural properties of the cells change in chronic alcoholism at the nanoscale level, and alterations are prominent at the length scales of ~100nm, which is around the length scales of the building blocks of cells [18]. Glial cells such as astrocytes and microglia, as well as the chromatin of the cell nuclei present in the cerebral cortex of the brain, which totals the vital portion of the central nervous system (CNS), are profoundly affected by chronic alcoholism. Chronic alcoholism can produce sustainable damage in the brain on different length scales. This structural damage can bring neuropathological disorders such as memory loss and dysfunction of the brain resulting in cognitive and behavioral deficits [105–107].

In the brain cells, the star-shaped astrocytes and microglia are the most abundant glial cells present in the CNS and mostly serve as a regulator of the CNS's immunity and tissue transplantation. In the same way, chromatin in all brain cells plays an important role in genetic inheritance. In humans, it is reported that a single astrocyte interacts with two million neurons at a time [108]. These astrocytes perform various tasks such as axon guidance, synoptic support, controlling blood flow, and blood-brain-barrier function. Along with regulating behavior, they play a vital role in neuroinflammation in both beneficial and detrimental ways depending on the stimuli they receive from their inflamed environment. Similarly, microglia act as the role of tissue macrophages which are involved in immune response, removing damaged neurons, tissue transplant, and other neurological mechanisms and diseases. However, alcohol is one of the most well-known adverse incentives for neuroinflammation. Pathogenesis of many CNS disorders and several neurodegenerative diseases are crucially caused by brain inflammation [109]. This inflammation activates the glial cells, specifically the microglia and astrocyte, and liberates the free radicals, cytokines, and inflammatory mediators that can damage normal brain function [110]. A recent study showed that alcohol treatment in the microglial cells and chromatin altered their morphology [111].

In some cases, these structural alterations may be reversible to a good degree through different types of treatments. It was reported that probiotic treatment has a good effect on brain health. In particular, it can soothe human brains and reduce structural abnormalities in brain cells/tissue to a certain extent [112,113]. Immunofluorescence results also show that probiotic treatment such as *Lactobacillus Plantarum,* when administered after a chronic alcohol-induced injury can rescue the alcohol-induced systemic inflammation and neuroinflammation resulting in improving the physical state of human brains [114]. *L. Plantarum* is a Gram-positive lactic acid bacterium present in fermented food and anaerobic plant matter which has ample applications in the medical and biomedical fields. In particular, *L. Plantarum* blocked alcohol-induced gut barrier dysfunction, endotoxemia, and liver damage which are directly associated with the well-functioning of the brain [115]. Therefore, we are using the recently developed mesoscopic physics-based light localization technique, IPR, which can quantify the molecular specific mass density fluctuations in cells/tissue as the degree of structural disorder due to diseases or any other abnormalities [22,23,38,102]. In the IPR technique, an optical disordered refractive index matrix is constructed based on the pixel intensities via confocal imaging and solved for optical eigenvalues and the eigenfunctions using the closed boundary conditions. Based on the mesoscopic theory, these eigenfunctions are used to quantify the molecular specific light localization properties of samples, that can be represented by the average of IPR, $<<IPR>>$, and the standard deviation (*std*) of IPR, $\sigma(<IPR>)$, of these eigenfunctions. The earlier IPR study results show that the degree of disorder strength i.e., $L_d = <dn> \times l_c$ is proportional to $<<IPR>>$ or $\sigma(<IPR>)$ [38,83]. This technique has been used to quantify the extent of aggressive cancer in biological cells, especially to detect the progress of carcinogenesis in drug treatment [38,62,83]. Here, we want to extend this method to probe the molecular-specific spatial structural changes in brain cells and organelles to study the effect of probiotics in chronic alcoholism.

In this work, using the IPR technique via confocal imaging, we report the effects of alcohol in glial cells, and molecular DNA/chromatin structure in nuclei of mice brain cells in the cortex region by probing molecular specific structural changes. Then, the effect of probiotic treatment in the glial cells and nuclei of the brain cells for the following cases: control, only alcohol fed, only probiotic fed, and simultaneously alcohol and probiotic fed were studied to see the effect of probiotics on the chronic alcoholic brain, using a mouse model.

4.2 Methods

4.2.1 Molecular specific structural disorder via confocal imaging and IPR technique

Confocal imaging is a technique that captures images with high optical contrast and resolution ranging in the submicron length scales. The confocal microscopy and its schematic are briefly explained in Chapter I Section 1.2.2. In confocal microscopy imaging, a spatial pinhole is used which blocks out-of-focus light to acquire a controlled depth of field and reduce background lights in images. For a confocal image, the amount of fluorophore dye that binds a molecular mass is proportional to the molecular mass density at any point or a small voxel. In general, dyes are independent of each other, and treating a cell with different molecular binding dyes at the same time and probing them with appropriate wavelengths can provide us the various molecular specific spatial structural mass density fluctuations in a cell using the IPR technique.

The submicron scale mass density fluctuations are quantified by calculating the degree of structural disorders in confocal images using the IPR technique. In the IPR technique, an optical lattice is formed using the pixel intensities of the confocal images which represent the ‘mass density fluctuations’ that were scanned voxel-wise. Based on the light localization strength, the average IPR or the disorder strength is computed. A higher value of the $<IPR>$ represents an increase in the mass density fluctuation in the cell or molecule. Henceforth, the average of $<<IPR>>$ or $\sigma(<IPR>)$ ultimately quantifies the degree of structural disorder in the medium. The theoretical model of the IPR technique has been reported earlier in Chapter I Section 1.2.3 [22,23,38,62,83] in detail; however, in this chapter, we will describe the technique in short.

As mentioned in [38,83], let us consider a pixel intensity $I(x,y)$ of the confocal image at position $r=(x,y)$ and ρ is the density of the molecule at voxel dV of the image is $I(r)=dV(\rho)$. It was shown in [38,116] that the local refractive index of the cell slice is directly proportional to the local mass density of the cell at that point (x,y) which is directly proportional to the confocal image intensity at any voxel that point.

The refractive index $n(x,y)$ of thin scattering substances such as biological cells has a linear relation to the mass density [116,117], and are correlated with the confocal image's intensity, $I(x,y)$, which is linearly proportional to the mass density, $M(x,y)$, and refractive index, $n(x,y)$, at the voxel as obtained in Section 1.2.3 equations (1.10, 1.11).

From this, we obtain the optical potential as $\varepsilon_i(x,y)$ and construct a representative refractive index matrix using the pixel intensity value [30] given as Section 1.2.3 equation (1.12). The optical potential, $\varepsilon_i(x,y)$ which is a representation of the spatial refractive index fluctuation relative to the average of the fluorescent molecules inside the sample [33,116].

Then the Hamiltonian of Anderson's Tight Binding model [28,30,118] is obtained as explained in Section 1.2.3 equation (1.13) of the closed system. We can generate the eigenfunctions (E_i's) from the Hamiltonian (H) of the system by diagonalization. Using these eigenfunctions (E_i's) we calculate the average IPR value, $<IPR>$, of the entire sample images as defined in [22,23,32,46,47]:

$$< IPR(L) >_{L\times L} = \frac{1}{N}\sum_{i=1}^{N}\int_0^L\int_0^L E_i^4(x,y)dxdy, \tag{4.1}$$

Where E_i is the i^{th} eigenfunction of the Hamiltonian H of the optical lattice size $L\times L$, and N is the total number of lattice points on the refractive index matrix.

It can be shown [38,83] that the average IPR value $<IPR>=<IPR(L)>$ is directly proportional to the structural disorder strength, and can be expressed as:

$$\langle\langle IPR(L)\rangle\rangle = \langle\langle IPR(L)\rangle_{L\times L}\rangle_{ensemble} \sim L_d = dn \times l_c, \tag{4.2}$$

$$\sigma(\langle IPR(L)\rangle) = \sigma(\langle IPR(L)\rangle_{L\times L})_{ensemble} \sim L_d = dn \times l_{c.} \tag{4.3}$$

Lastly, the $<<IPR(L)>_{L\times L}>_{ensemble} = <<IPR>>$ and $\sigma(<IPR(L)>_{L\times L})_{ensemble} = \sigma(<IPR>)$ which is directly proportional to the disorder strength (L_d) of the sample and acts as potential biomarkers of the of biological cells to quantify any types of abnormalities in glial cells and chromatin of the brain cells.

4.2.2 Brain tissue sample preparation using an alcoholic mouse model

We study the effects of probiotics on chronic alcoholic brain cortical cells and nuclei using a mouse model. In particular, we will study the glial cells: astrocytes and microglia, and the DNA/chromatin of the nuclei from cells of the cerebral cortex region of the brain which includes the major portion of the CNS. The brain sections were incubated with glial fibrillary acidic protein (GFAP) antibody, the microglia cells with anti-TMEM119 transmembrane protein antibody, and the chromatin in the nuclei of brain cells with DAPI for confocal imaging [114].

The effects of alcohol and probiotics in the brain cells were studied using 8-10 weeks old mice (C57BL/6, Harlan, Houston, TX) divided into 4 different groups of 6 mice per group. All mice were housed in an institutional animal care facility with 12/12 of the light-dark cycle which have easy access to regular laboratory chow and water until the start of the experiment. To be more specific, for (1) Control (PF), (2) Ethanol Fed (EF), (3) Probiotic Fed (PF+LP), (4) Probiotic and Ethanol Fed (EF+LP), we observed glial cells and nuclei of the brain cells, namely: (I) Astrocytes, (II) Microglia, (III) Chromatin.

A recent study based on immunofluorescence confocal microscopy showed that alcohol elevates the expression of different proteins or dyes as an activation marker in different brain cells and components to explain the alcohol effect [114]. The rationale for choosing the glial cells and chromatin to probe the abnormalities in alcohol and probiotic treatment are: **(I) Astrocytes and anti-GFAP antibody staining:** These cells represent a significant portion of the CNS and can interact with millions of neurons at a time. They get exposed to external simulators such as alcohol and probiotics. For confocal imaging, these cells can be easily tagged by the glial fibrillary acidic protein (GFAP) antibody marker. GFAP protein is encoded by the GFAP gene in humans. GFAP antibody targets type-III intermediate filaments. Intermediate filaments are overactive/expressed in astrocytes in the CNS when the brain is exposed to a chemical such as alcohol. Therefore, the molecular-specific type-III intermediate filament can be probed by GFAP for confocal imaging to probe the activeness of astrocytes. **(II) Microglia and anti-TMEM119 transmembrane protein antibody staining:** Microglia cells are also considered as the macrophages of the CNS and include a major portion of the CNS system, which clean up the cellular debris and participate in neuroinflammation. These glial also easily get exposed to alcohol or drug treatment similar to astrocytes. It is now known that overexpression or upregulation of transmembrane protein TMEM119 in microglia due to the presence of stimulators like alcohol/probiotic can be tagged by anti-TMEM119 transmembrane protein antibody for the molecular specific confocal imaging. **(III) Chromatin and DAPI staining:** In all brain cell nuclei, chromatin is highly abundant. Chromatin is the primary DNA molecular component of the cell nucleus. It has been shown that chromatin spatial structures altered with the progress of diseases and abnormalities. The chromatin can be easily stained by the standard DAPI dye. The nanoscale changes in these types of cells are shown well for the detection of cancer stages. We want to probe the molecular-specific structural alteration of DNA mass density in chromatin in nuclei by DAPI staining and confocal imaging tissue sections of the cortex region.

***Bio-Marker**:* The primary marker is to probe the confocal images using the IPR technique and to quantify the molecular-specific nanoscale spatial mass density fluctuations as the degree of structural disorder, mentioned in Section 4.2.1.

As described above, mice were randomly divided into 4 categories with 6 mice per group and fed with ethanol following a standard protocol in Leiber DiCarli liquid diet (ethanol: 0% for 2 days, 1% for 2 days, 2% for 3 days, 4% for 1 week, 5% for 1 week, and followed by 6% for 1 week) with or without *L. Plantarum* (strain 256, 10^6 cfu/ml) or isocaloric maltodextrin for 4 weeks. Control and only probiotic fed animals were pair-fed with isocaloric substitution of ethanol with maltodextrin. Animals were pair-fed to maintain a similar diet intake in all groups. In the last week of experiments, the average diet intake per mouse per day was 0.7 ml which means the *L. Plantarum* intake by a mouse was about 0.7×10^6 cfu/day and grouped as (1) The first group was pair-fed with maltose dextrin in a liquid diet, (2) the second group was fed with ethanol liquid diet, (3) the third group was fed with the probiotic in a liquid diet, and (4) the fourth group was fed with probiotics in the presence of ethanol liquid diet.

Brain tissues: When the mice were treated for 4 weeks, they were sacrificed following the protocol approved by the University of Tennessee Health Science Center (UTHSC) Institutional Animal Care and Use Committee, and their brain sections were removed. The brain tissue sections from the cerebral cortex region were then cryo-freeze and sectioned into $10\mu m$ slices by using a cryostat.

Staining for fluorescence confocal imaging: The different sections of the brain were incubated with three different fluorescence agents: anti-GFAP antibody, anti-TMEM119 antibody, and DAPI according to standard protocols.

Confocal imaging: Brain cryosections (*10μm* thick) were fixed in acetone: methanol (1:1) at −*20°C* for 2 min and the sections were rehydrated in PBS (*137mM* sodium chloride, *2.7mM* potassium chloride, *10mM* disodium hydrogen phosphate, and *1.8mM* potassium dihydrogen phosphate). The tissue sections were permeabilized with 0.2% Triton X-100 in PBS for 10 min and blocked in 4% nonfat milk in Triton-Tris buffer (*150mM* sodium chloride containing 10% Tween *20mM* and *20mM* Tris, pH 7.4). It was then incubated for 1 hour with the primary antibodies (mouse monoclonal anti-Alexa Fluor 488-conjugated anti-GFAP and rabbit polyclonal anti-TMEM119 antibodies), followed by incubation for 1 hour with secondary antibodies Cy3-conjugated anti-rabbit IgG antibodies) and 10 min incubation with DAPI (Hoechst 33342 dye). The fluorescence was examined using a Zeiss 710 confocal microscope (Carl Zeiss GmbH, Jena, Germany) and images from *x–y* sections (*1μm*) were collected by LSM 5 Pascal software (Carl Zeiss Microscopy). Images were stacked by *ImageJ* software (Image Processing and Analysis in Java; National Institutes of Health, USA) and processed by Adobe Photoshop (Adobe Systems, USA). All the images for tissues from the different groups were collected and processed under identical conditions.

IPR analyses: The IPR analyses were performed using a confocal image to quantify the molecular-specific nano to microscale mass density fluctuations in the cells and nuclei, as discussed above.

4.3 Results

Confocal images of the mice's brain cortex tissues stained with different proteins/dyes were obtained to study the effect of probiotics in chronic alcoholic glial cells and the chromatin of the nuclei. Then the IPR analyses were performed on individual confocal images at $0.8 \times 0.8\mu m^2$ area, as described. The degree of disorder strength or $<IPR>$ at each point at length scales, $L=0.8\mu m$ of cells, and molecular components of the mice brain cells were computed. On average, 6 mice per group were considered, and at least 30 confocal micrographs for each category: astrocytes, microglia, and the chromatin of mice brain cell nuclei were analyzed separately. From these, the *std* of the ensemble average IPR values were calculated as obtained in equations (4.2, 4.3). Finally, the computed $\sigma(<IPR>)$ of astrocytes, microglia, and chromatin of the mice's brain cells for ethanol-fed (EF), probiotics fed (PF+LP), and probiotics fed with ethanol (EF+LP) were compared, relative to the control fed (PF) mice separately.

The intensity variation in the *IPR* images represents mass density fluctuations which indicate the structural abnormalities present in different glial cells and the chromatin of mice brain cell nuclei. In the *IPR* images, a higher mass density fluctuation is represented by the red color, while the lower is represented by the blue color. As can be seen from the *IPR* images (Figs. 4.1,4.3,4.5), the mass density or refractive index fluctuations increase in astrocytes and microglia, and the chromatin of the brain cell nuclei when mice were treated with ethanol indicates that alcohol altered the brain cells at the submicron scale. However, the slight increase in the $\sigma(<IPR>)$ value of the glial cells for mice fed with only probiotics might be due to the interaction of probiotics with the gut cells/tissues blocking barrier dysfunction and endotoxemia to some extent indirectly resulting in structural abnormalities in the brain. On the other hand, when the mice were treated with both probiotics and ethanol simultaneously, the $\sigma(<IPR>)$

reduced approximately back to normal or less than the normal in both cells and chromatin, which suggest that probiotics function well in the presence of alcohol, preventing gut barrier dysfunction and endotoxemia and results in an increase in the efficiency of brain functioning. Therefore, probiotics such as *L. Plantarum* are considered good for brain health and help to soothe and improve the cognitive function of the chronic alcoholic brain. The results are systematically described below.

4.3.1 Structural alterations in astrocytes

Fig.4.1. (a)-(d) show the confocal image of astrocytes incubated with anti-GFAP antibodies, while Fig.4.1 (a')-(d') are their corresponding *IPR* images, respectively. In Fig 4.2, the bar graphs of relative change in the disorder strength (L_d) or $\sigma(<IPR>)$ of brain astrocytes cells of ethanol-fed (EF), probiotic fed (LP), and ethanol with probiotic fed (EF+LP) mice with control fed (PF) mice are shown. As can be seen from Fig. 4.2, the relative study of $\sigma(<IPR>)$ of astrocyte brain cells increases when mice were fed with ethanol. In contrast, it significantly decreases when mice were fed subsequently with probiotics and ethanol at the same time. It is found that probiotics interact with the intestine, which indirectly affects the brain due to the Gut-Microbiome-Brain axis and may increase the molecular spatial structural disorder of astrocytes in the brain cells. Therefore, the $\sigma(<IPR>)$ of astrocyte cells of mice fed with probiotics only (PF+LP) is relatively higher compared to the PF. Although probiotics were believed to reduce intestinal dysbiosis and enhance the gut-brain interaction, the result shows that probiotics may be reactive to some specific components of gut cells and hence increase the mass density fluctuations of the astrocytes. In particular, the bar graphs show that the $\sigma(<IPR>)$ of astrocyte

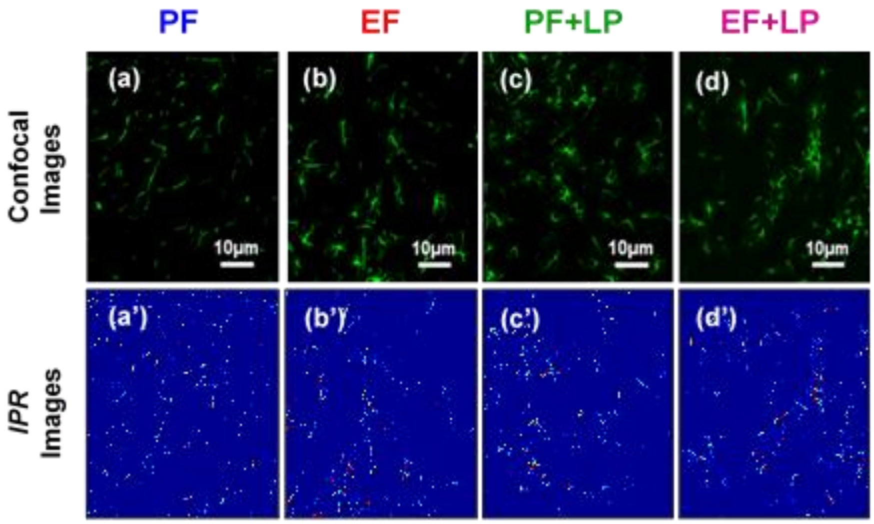

Figure 4.1 Confocal and IPR images of astrocytes.

Confocal and IPR images of astrocytes (PF, EF, PF+LP, EF+LP): (a)-(d) are the representative confocal images of control (PF), ethanol fed (EF), probiotics fed (PF+LP), and ethanol and probiotics fed (EF+LP) mice brain astrocytes cells while (a')-(d') are their corresponding *IPR* images respectively at length scale $L=0.8\mu m$ which are distinct. The *IPR* images show that the molecular specific mass density fluctuation in astrocytes increases in the presence of ethanol as well as probiotics, but when treated together, they decrease the density fluctuation due to alcohol damage.

cells of EF mice increased by 280% relative to PF. This increase in the L_d or $\sigma(<IPR>)$ implies that ethanol-induced intestinal dysbiosis, which is a valid approach to dissect the gut-brain interaction. This results in an adverse effect in the brain cells, especially in astrocytes, which perform a variety of tasks such as axon guidance, maintenance of redox potential, regulation in neurotransmitter and ion concentrations, synaptic support, blood flow control, removal of toxins, and debris from the cerebrospinal fluid, etc. [119]. Astrocytes, the most numerous cells within the CNS of the brain and can easily be exposed to alcohol. Therefore, chronic alcoholism may exacerbate neuronal dysfunction and advances mechanisms in potentiating or nullifying the pathway of neuropathologic injury [120]. However, the $\sigma(<IPR>)$ of astrocyte cells decreases by 100% relative to EF when the mice were fed with probiotics and ethanol at the same time. This decrease in the $\sigma(<IPR>)$ of astrocytes cell of EF+LP supports that probiotics in the presence of ethanol are highly efficient and blocked alcohol-induced gut barrier dysfunction and endotoxemia, which are indirectly good for brain cells and maintain proper brain functions.

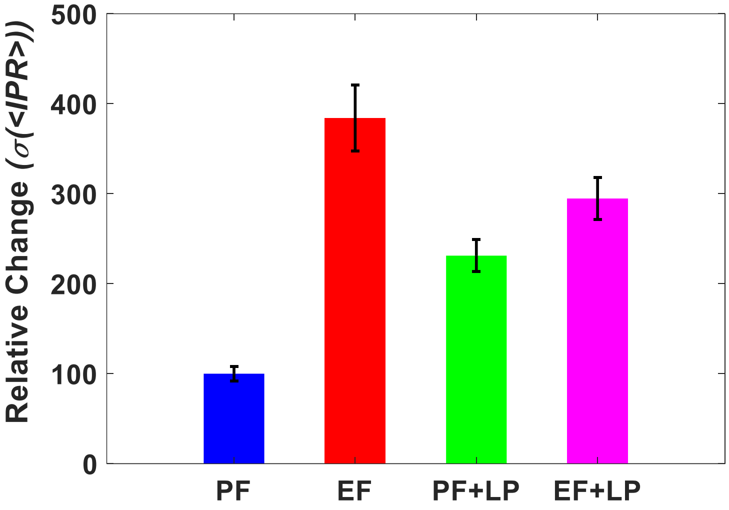

Figure 4.2 Bar graph representation of relative change in the disorder strength in astrocytes.

Bar graph for the relative values of molecular specific light localization property quantified as $\sigma(<IPR(L=0.8\mu m)>)$ or disorder strength $(<IPR>\sim L_d)$ of astrocytes cells (total n~100 cells: aroud~20 cells per micrographs, ~5 micrographs per mouse) of control (PF) mice compared to ethanol fed (EF), probiotic fed (PF+LP), and ethanol and probiotics fed (EF+LP) mice. The IPR analysis of astrocytes shows that the $\sigma(<IPR>)$ or $L_d \sim dn \times l_c$ of EF mice increased by 280% relative to control. Also, the L_d value of astrocyte cells of PF+LP mice is relatively higher compared to the control. This increase in mass density fluctuations indicates some effect of probiotics on the astrocytes alone. However, the L_d value of astrocytes cells of EF+LP mice decreases by 100% relative to EF mice which implies probiotics get stimulated with ethanol decreasing the mass density fluctuations that are beneficial for brain cells. Student's t-test obtained p-value for EF is 0.004, PF+LP is 0.03, and EF+LP is 0.001 compared to PF. ($P\text{-values} < 0.05$).

4.3.2 Structural alterations in microglia

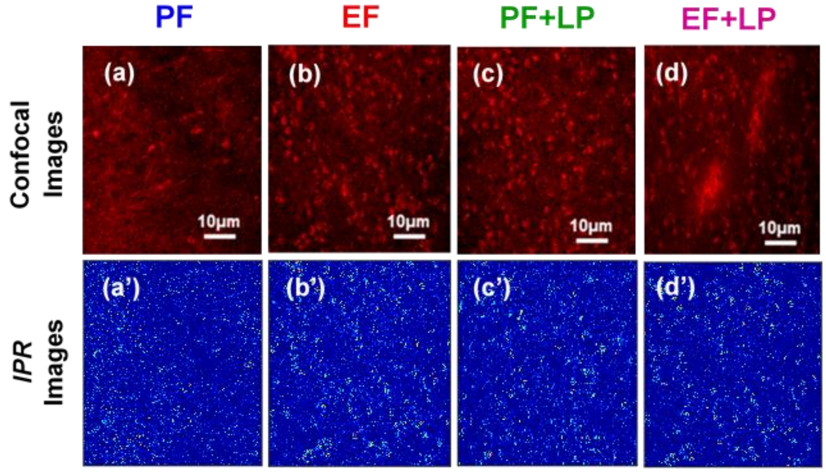

Figure 4.3 Confocal and IPR images of microglia

Confocal and IPR images of microglia (PF, EF, PF+LP, EF+LP): (a)-(d) are the representative confocal images of control (PF), ethanol fed (EF), probiotics fed (PF+LP), and ethanol and probiotics fed (EF+LP) of mice brain microglia cells while (a')-(d') are their respective *IPR* images at sample length $L=0.8\mu m$. The *IPR* images are distinct from the confocal images and show that the molecular-specific mass density fluctuations increase in the microglia brain cells in the presence of ethanol. Then the density fluctuation decreases when fed with ethanol and probiotics simultaneously.

Fig. 4.3. (a)-(d), shows the confocal image of microglia incubated with the anti-TMEM119 transmembrane protein antibody. Fig.3. (a')-(d') are their corresponding *IPR* images, respectively. Fig. 4.4, the bar graphs of relative change in the disorder strength (L_d) or $\sigma(<IPR>)$ of microglial cells of control fed (PF) mice with ethanol-fed (EF), probiotic-fed (LP), and ethanol and probiotic-fed (EF+LP) are shown. Fig. 4.3 represents the confocal images and *IPR* images of the microglia cells, where IPR images are highly distinct from confocal images. The bar graph presented in Fig. 4.4 indicates the effect of ethanol and probiotics in mice brain

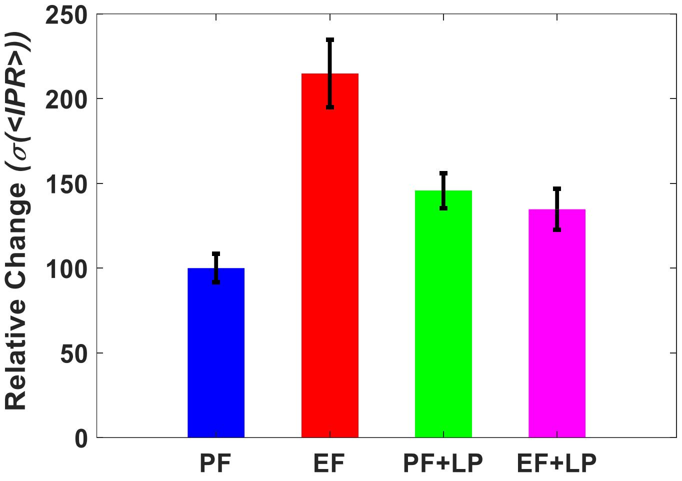

Figure 4.4 Bar graph representation of relative change in the disorder strength in Microglia.

Bar graph for the relative study of molecular specific light localization property quantified as $\sigma(<IPR(L=0.8\mu m)>)$ or disorder strength $(<IPR>\sim L_d)$ of microglia cells (total n~100 cells: around ~20 cells per micrographs and ~5 micrographs per mouse) of control (PF) mice compared to ethanol fed (EF), probiotic fed (PF+LP), and ethanol and probiotics fed (EF+LP) mice. The IPR analysis of microglia shows that the $\sigma(<IPR>)$ *or* L_d of EF mice increase by 120% in reference to PF mice. The L_d value of microglia cells of PF+LP mice is relatively higher than the control. This increase in mass density fluctuations represents some effect of probiotics in brain microglial cells. However, the L_d value of microglial cells of mice fed with EF+LP decreases by 100% relative to EF mice which implies ethanol stimulates probiotics resulting in a decrease in the mass density fluctuations that helps in soothing the brain cells. Student's t-test obtained p-value for EF is 0.009, PF+LP is 0.03, and EF+LP is 0.01 compared to PF. ($P\text{-values} <0.05$).

microglial cells based on the IPR analysis and shows a relative study induces changes in gut microbiota, and as a result of gut-brain interaction it may mitigate of mice for EF, PF+LP, and EF+LP with PF. The IPR analysis performed at the same sample length of all cases shows that the $\sigma(<IPR>)$ of EF mice increases by 120% relative to PF. This increase in the disorder strength of microglia brain cells of EF mice suggests that alcohol neuroinflammation, destroying the microglial cells or immune system of the brain. Microglia are considered as the macrophages of the CNS that clean up the cellular debris and participate in neuroinflammation to various intrinsic and extrinsic stimuli. In addition to well-established phagocytic function and innate immune function, microglia are involved in the development of CNS immunopathology [121]. It was founded that alcohol enhances immunomodulatory molecules such as corticosterone and endotoxin, which degrade the neuroimmune cells of the brain and selectively modulate the intracellular signal transductions of microglia [122]. Also, the IPR analysis shows that the $\sigma(<IPR>)$ of microglial cells of mice fed with only probiotics (PF+LP) is relatively higher than PF. This higher disorder strength might be due to probiotics interacting with mice gut cells/tissues differently which results in microglia cells being more aggressive with the increase in mass density fluctuations. Therefore, probiotics used to soothe and strengthen the cognitive function of the brain may sometimes be reactive to the neuroimmune system of the brain cells, but we have yet to study this in detail. On the other hand, the $\sigma(<IPR>)$ of microglial brain cells of mice fed with alcohol and probiotics simultaneously decreases by 100% relative to EF. This implies alcohol stimulates probiotics and blocked the ethanol-induced gut barrier dysfunction, endotoxemia, and liver damage resulting in increasing the efficacy of brain function and hence, reducing density fluctuations and in turn, decreasing the disorder strength (L_d) of microglia of brain cells. Therefore, this promising result suggests that probiotics with alcohol are good for brain cells and enhance the development of CNS immunopathology.

4.3.3 Structural alterations in chromatin

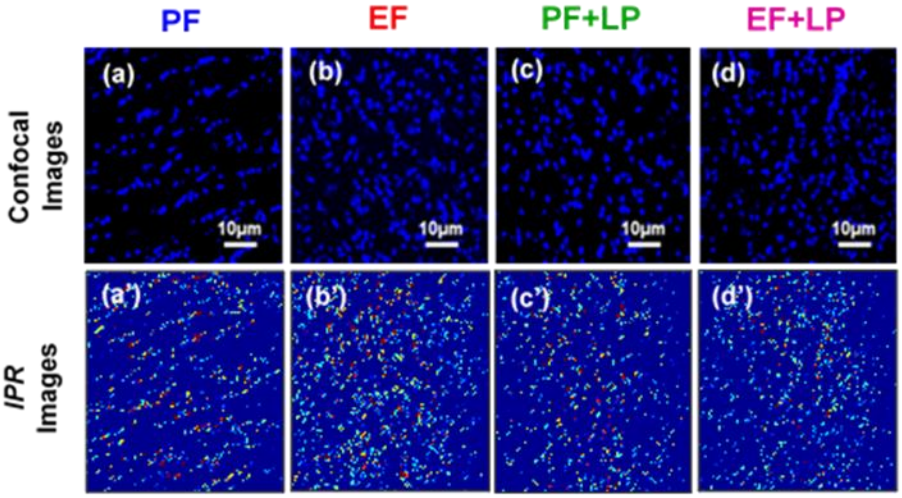

Figure 4.5 Confocal and IPR images of chromatin

Confocal and IPR images of chromatin of brain cells (PF, EF, PF+LP, EF+LP): (a)-(d) are the representative confocal images of control (PF), ethanol fed (EF), probiotics fed (PF+LP), and ethanol and probiotics fed (EF+LP) while (a')-(d') are their respective *IPR* images of chromatin of mice brain cells at the sample length $L=0.8\mu m$. The IPR images are distinct from the confocal images and show that the molecular specific mass density fluctuation increases in the chromatin of mice brain cell nuclei in the presence of ethanol which decreases when they were fed with alcohol and probiotics simultaneously.

Fig.4.5. (a)-(d) show the confocal images of brain cell nuclei incubated with DAPI, while Fig. 4.5. (a')-(d') are their corresponding *IPR* images, respectively. In Fig. 4.6, the bar graphs relative change in the disorder strength (L_d) or $\sigma(<IPR>)$ of nuclei in the brain cell of control (PF) mice with ethanol fed (EF), probiotic-fed (LP), and ethanol and probiotic-fed (EF+LP) are shown. The molecular-specific IPR analysis of DAPI stained confocal images of mice brain cell nuclei at sample length, $L=0.8\mu m$ indicates that the mass density fluctuations or $\sigma(<IPR>)$ of EF mice increases by 25% relative to PF. This is because of chronic alcohol-induced intestinal mucosal barrier dysfunction in the gut, which as a result induces an adverse effect in the brain

due to gut-brain interaction. This adverse effect is in some way related to an increase in submicron scale mass density fluctuation or the $\sigma(<IPR>)$ in the chromatin of EF mice brain cells. Hence, the rise in DNA mass density fluctuations of the chromatin due to alcohol is responsible for an increase in the degree of disorder strength (L_d). Persistent alterations to the chromatin structure are factors for epigenetics inheritance and can have a long-lasting influence on the activity and connectivity functions of the brain [123]. The $\sigma(<IPR>)$ of chromatin in the brain cell nuclei of mice fed with only probiotics (PF+LP) is relatively lower compared to the PF, indicating that probiotics are good for the mice digestive system that is correlated with soothing and well-functioning of the brain especially in chromatin of nuclei. Further, the $\sigma(<IPR>)$ value of chromatin in brain nuclei of mice fed with alcohol and probiotics at the same time decreases by 40% relative to PF. This decrease in the $\sigma(<IPR>)$ of the chromatin of mice cell nuclei fed with alcohol and probiotics at the same time is because probiotics in the presence of ethanol get highly stimulated and attenuate alcohol-induced intestinal mucosal barrier dysfunction, which is good for the chromatin of the brain cell nuclei and allow the brain to soothe and function better.

The molecular-specific structural quantification of probiotic's effect on alcoholic brain cells using the confocal image and IPR analyses shows that alcohol affects the digestive system, which indirectly damages the glial cells and the chromatin of the nuclei of the brain cells. We speculate that the gut-brain interaction associated with these findings involves endotoxin absorption due to intestinal barrier dysfunction and gut dysbiosis. The probiotic, *L. Plantarum* by itself caused a small increase in the degree in the disorder strength or $\sigma(<IPR>)$ of astrocytes and microglia cells while a decrease in the chromatin of the brain cells. However, the obtained result strongly supports that the probiotics *L. Plantarum* feeding very effectively blocked alcohol-induced changes in astrocytes and microglia.

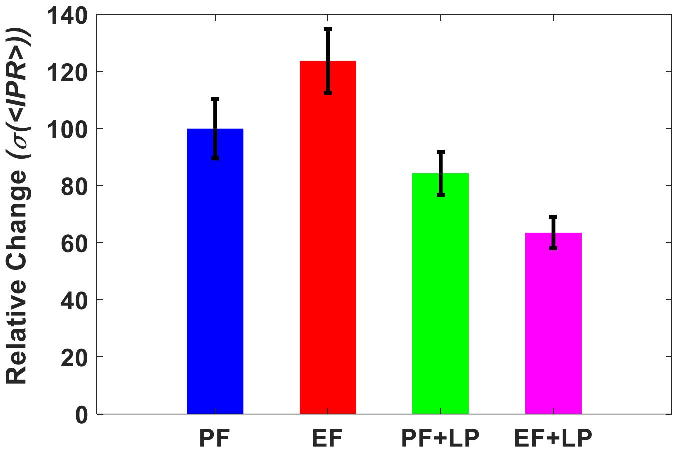

Figure 4.6 Bar graph representation of relative change in the disorder strength of chromatin.

Bar graph for the relative study of molecular specific light localization property quantified as $\sigma(<IPR(L=0.8\mu m)>)$ or disorder strength $(<IPR>\sim L_d)$ of chromatin in nuclei (total cells n~400, around ~80 cells per micrographs and ~5 micrographs per mouse) of control (PF) mice concerning to ethanol fed (EF), probiotic fed (PF+LP), and ethanol and probiotics fed (EF+LP) mice. The IPR analysis of chromatin of the mice brain cells shows that the $\sigma(<IPR>)$ or L_d of EF mice increases by 25% relative to control. The L_d value of chromatin in nuclei of mice fed with PF+LP is relatively lower compared to the control. This decrease in mass density fluctuations represents some effect of probiotics in chromatin of the brain cell nuclei. However, the L_d value of chromatin of mice brain cell nuclei fed with EF+LP decreases by 40% relative to PF mice due to the decrease in mass density fluctuations which implies probiotics in the presence of ethanol is more active and help in soothing the brain function. Student's t-test obtained p-value for EF is 0.01, PF+LP is 0.002, and EF+LP is 0.007 compared to PF. (*P-values* <0.05).

4.4 Conclusions

The molecular-specific light localization technique, IPR, is used to study the effect of probiotics in chronic alcoholism in glial cells, astrocytes, and microglia, and the chromatin of brain cell nuclei using a confocal image and a mouse model. Changes in the molecular specific structural disorder were probed for: (i) upregulation of type III intermediate protein spatial mass density in astrocytes, (ii) upregulation of transmembrane protein anti-TMEM119 spatial mass density in microglia, and (iii) rearrangements of DNA mass density in nuclei of neural cells. The submicron scale mass density fluctuations quantified as the *std* of average *IPR* or $\sigma(<IPR>)\sim L_d$ using a confocal image show an increase in disorder strength (L_d) of the molecular specific probing of astrocytes and microglia cells, as well as the chromatin of brain cell nuclei of alcohol-treated mice. This increase in the disorder strength or mass density fluctuations in brain glial cells and chromatin is due to gut-brain interaction confirms alcohol-induced gut barrier dysfunction, endotoxemia, and liver damage and eventually leads to neuroinflammation, especially in glial cells and the chromatin of brain cell nuclei due to gut-brain interaction. On the other hand, probiotics fed control mice have a small increment in the disorder strength of brain glial cells, which may be due to the interaction of probiotics, *L. Plantarum* in gut cells/tissues differently increasing mass density fluctuations. Therefore, the L_d value increases in the astrocytes and microglia cells when fed with only probiotics invite a detailed study to elucidate plausible reasons for an adverse effect of *L. Plantarum* in glial cells, although probiotics are considered reasonable and used to improve the cognitive function of the brain. Interestingly, a decrease in the L_d value in glial cells and the chromatin of brain cell nuclei fed with ethanol and probiotics simultaneously relative to control and ethanol fed mice indicate that *L. Plantarum* in the presence of alcohol gets highly stimulated and increase the efficacy and well-functioning of the brain. That means, these probiotics first increase the efficacy of the digestive system and as a result of gut-brain interaction, which indirectly helps in soothing the brain's physical structure and enhances the multifunctionality of the brain. Therefore, this almost reversible effect of probiotics when it is given with the alcohol on the brain cells/components could be one of the ways to mitigate neurological abnormalities in the brain cells due to alcohol or any other drug. As an illustration of the potential application of the recently developed mesoscopic physics-based molecular-specific IPR technique via confocal imaging, we have successfully quantified probiotic effects on glial cells and chromatin of the brain cell nuclei based on the structural abnormalities present in brain cells/tissues.

CHAPTER V

QUANTIFICATION OF NANOSCALE STRUCTURAL ALTERATIONS IN OVARIAN CANCER CELLS TO STUDY ANTI-CANCEROUS DRUG EFFECT USING TEM-IPR

This chapter is adapted from the author's published article with copyright permission from the publisher. Ref [57] P. Adhikari et. al., "Studying nanoscale structural alterations in cancer cells to evaluate ovarian cancer drug treatment, using transmission electron microscopy imaging," ***Physical Biology 17(3), 036005*** **(2020).**

Although, the main probing technique in this dissertation is optics/photonics that are within the diffraction limit (resolution ~200nm). However, it would be interesting to see the properties of the cell at nanoscale resolution, that can support the optical techniques. In this chapter, we have used TEM imaging to probe the structural disorder below 100nm and studies the effects of anti-cancerous drugs on ovarian cancer cells.

Anti-cancerous therapies are intended for the growth inhibition of cancer cells which are initially at the nanoscale level; however, it is challenging to detect the efficacy of such drugs in the early stages of treatment. A unique method to assess the impact of anti-cancerous drugs on cancerous cells/tissues is to probe the nanoscale structural alterations. For this, TEM imaging on thin cell sections is performed to obtain their nanoscale structures where we can probe up to 1nm structure. In this work, we apply the IPR technique in TEM imaging (TEM-IPR) to study the effect of different anti-cancerous drugs on ovarian tumorigenic cells, using their nanoscale structural alterations as a biomarker. Based on the degree of disorder strength the efficacy of the anti-cancerous drug and level of tumorigenicity are quantified. Hence the potential applications of the technique for cancer treatment and diagnosis are discussed.

5.1 Introduction

5.1.1 Why TEM imaging and probing nanoscale changes in cancer?

TEM imaging is a method where we can probe ~*1nm* resolution within the sample, and this has been used for imaging of cells at the nanoscale to see the inner structures of the cells, in general, qualitatively. It has been established that cancer progression is associated with the nanoscale structural alteration in a cell due to rearrangements of the building blocks of the cell such as DNA, RNA, and lipids. Therefore, TEM imaging with spatial nano-resolution is a good modality to look at the nanoscale cell structures and measure cancerous changes in cells at the nanoscales.

The structural alterations in cells have been characterized by visible-light microscopy techniques within the diffraction limit. For example, the newly developed spectroscopic microscopy technique has shown success in probing these alterations to some degree that are prominent in early carcinogenesis [16,17,58,124–126], and these nano morphologies are associated with the basic cellular building blocks. Therefore, TEM imaging is a good modality to probe cancerous changes in cells at the nanoscale level, very much beyond the diffraction limit of light. The details of the TEM schematics and application in scientific research are explained in Chapter I Section 1.2.1. Furthermore, the recently developed light wave localization technique, IPR using TEM imaging, has shown success in quantifying the degree of structural changes in one parameter, known as the degree of the structural disorder [22,23]. In particular, using the IPR method, a TEM image is used to construct a disordered 2D mass matrix, and from this, we generate a 2D refractive index matrix. Optical waves are then solved for their eigenvalues and eigenfunctions using the refractive index matrix with closed boundary conditions. The light localization properties are measured by the average inverse participation ratio, *<IPR>*, and standard deviation of the IPR, $\sigma(<IPR(L)>)_{cells}$, of the eigenfunctions of the light waves in these samples. It is shown that the degree of structural disorder is proportional to the *<IPR>* or $\sigma(<IPR(L)>)_{cells}$ [32,33]. Therefore, the *<IPR>* can be used as a measure of the degree of nanoscale structural disorder, and to monitor structural change in cells under diseases condition. The IPR method is a very versatile approach. The IPR method, using TEM imaging, has been recently generalized to study the structural changes in brain and colon cells in chronic alcoholism [127,128]. Furthermore, the IPR method also extended to study the molecular specific (DNA, histone, etc.) structural changes in cells by using molecular-specific fluorophores and confocal microscopy imaging [38,83].

5.1.2 Ovarian cancer study

Ovarian cancer (OC) ranks 5th in cancer-related deaths among women and accounts for more deaths than any other cancer of the female reproductive system. The American Cancer Society (ACS) estimated new cases of OC in the USA in 2019 would be 22,530, whereas estimated deaths would be 14,000. Most OC cases are diagnosed at a very late stage, of which 51% are diagnosed as stage III and 29% are diagnosed as stage IV [129]. The exact cause that triggers OC is not clearly understood but there are several risk factors such as fertility therapy, late pregnancy, family history, hormone therapy after menopause, etc. are associated with the development of OC. Metabolic alterations, suppression of tumor suppressor genes, and oncogenic activations are also considered as triggering factors for OC initiation and progression of the disease [130,131]. Although initially sensitive to chemotherapy treatment, however, the majority of OC patients develop chemoresistance. 10 years survival rate for most patients of all stages of OC is ~30%. Development of chemoresistance, widespread disease during the time of diagnosis, and tumor recurrence are the major challenges in the therapeutics of ovarian cancer [132].

In this study, we are focusing on analyzing the impact of novel anti-cancerous drug treatment in the tumor forming OC cell line *in vitro*. HSulf-1 knockdown OV202 cells are selected for this study for their aggressive tumor forming ability and high proliferation rate [133,134]. This method of analysis is aimed to understand the effect of anti-cancerous drugs on cells in the early phases of treatment. Here we propose a novel TEM-IPR approach to assess the impact of anti-cancerous drugs in cancerous cells by quantifying the degree of nanoscale structural disorder.

5.2 Methods

5.2.1 IPR technique using TEM images

TEM experiment has a resolution of ~*1nm* and can identify the nanoscale architectural alterations inside the cells which take place in normal cells when affected by cancer. These nanoscale alterations happen in the cells due to the rearrangement of the basic building blocks of the cells, such as DNA, RNA, lipids, macromolecules, etc. This results in mass density fluctuations in the cells. Using a thin slice of a cell (~*100nm*), the mass density variations can be probed by TEM imaging. The detail of the TEM schematic and imaging is presented in Chapter I Section 1.2.1. The IPR calculation is an efficient technique to measure and quantify the cancerous level of aggressiveness in a cell through its mass density fluctuations. A higher $<<IPR(L)>>$ or $\sigma(<IPR(L)>)$ value indicates an increasing amount of the nanoscale mass density fluctuations in cells. The IPR technique is described in detail in Chapter I Section 1.2.3 [22,23,32,33]. However, we will describe the IPR technique using TEM images in brief.

The refractive index of a thin cell slice at a point $n(x,y)$ can be written as $n(x,y) = n_o+dn(x,y)$, where n_o is the average refractive index and $dn(x,y)$ is the fluctuation of refractive index at (x,y) indicated voxel. In the thin sample, a voxel of area $dxdy$ at position (x,y) and thickness dz, the transmission TEM intensity: $I_{TEM}(x,y)=I_0-I_0\alpha d(z)$, where α is a transmission related constant depends on the mass of the voxel as shown in Chapter I Section 1.2.3. TEM image intensity at any voxel point (x,y) for a thin cell sample can be expressed as $I_{TEM}(x,y) = I_{0TEM} + dI_{TEM}(x,y)$, where I_{0TEM} is the average pixel intensity and $dI_{TEM}(x,y)$ is the fluctuation part of the pixel intensity. Here, the intensity fluctuation $I_{TEM}(x,y) < I_{0TEM}$ (average intensity), where $I_{0TEM}=<I(x,y)>_{(x,y)}$ and $dI_{TEM}(x,y)=I_{TEM}(x,y) - <I(x,y)>_{(x,y)}$ and $dn(x,y) < n_0$.

Therefore, the intensity of a TEM image is linearly proportional to the mass, M, and refractive index, n of the voxel as shown in Chapter I equation (1.10, 1.11), except I_{TEM} is the intensity of the TEM image. From this, we can calculate the optical potential of the voxel point as $\varepsilon_i(x,y)$ obtained in Chapter I equation (1.12) to generate an optical lattice.

Knowing the optical potential at every point, the Anderson disordered tight-binding model TBM Hamiltonian [28,30,118] can be obtained as in Chapter I equation (1.13) for the TEM closed system. For a sample size of length L in the TEM image, we have $L\times L$ sample area in the TEM image. We calculate the average IPR at length L where $L=N_L\times dx$ ($dx=dy$). As there are $N=N_L\times N_L$ numbers of lattice points, thus, there will be N eigenvalues, as well as the same number of eigenvectors. Finally, the average IPR value of the sample of length L or size $L\times L$ is defined as [22,23,32,33,46,47]:

$$< IPR >_N = \frac{1}{N}\sum_{i=1}^{N}\int_0^L\int_0^L E_i^4(x,y)dxdy, \tag{5.1}$$

where E_i denotes the *i*-th eigenfunction of the Hamiltonian, N is the total number of potential points on the refractive index matrix (i.e., $N=(L/dx)^2$). It has been shown that the ensemble-averaged IPR value (i.e., ensemble-averaged of similar type of cells): $<<IPR(L)>> = <<IPR(L)>_{L\times L}>$ *or* $\sigma(<IPR(L)>$, is proportional to the degree of structural disorder L_d. Then,

$$\langle IPR\rangle \equiv < IPR >_{ensemble} \sim L_d = dn \times l_c \,, \tag{5.2}$$

$$\sigma(< IPR >) \equiv \sigma(< IPR >)_{ensemble} \sim L_d = dn \times l_c \,. \tag{5.3}$$

Equation (5.1) presents the average value of one IPR pixel at length (L) that is constructed from the $L\times L$ TEM area or N pixels of the TEM image. Our statistical analysis involves calculating the average and standard deviation of the disorder strength of IPR values, i.e. L_d values over the cell samples for the length of a given sample. Using this structural disorder strength $<<IPR(L)>>$ *or* $\sigma(<IPR(L)>)$ or L_d as a biomarker, we study the structural properties of ovarian cancer cells with anti-cancerous drug treatments.

5.2.2 Sample preparation and TEM imaging

5.2.2.1 Ovarian normal and cancer cell lines

OV202 cell line is a low-passage primary ovarian cancer cell line established at the Mayo Clinic [133]. OV202 NTC (expressing HSulf-1) and Sh1 cells (HSulf-1 deficient) are developed by Dr. Shridhar’s group at Mayo Clinic and are described earlier elsewhere [134]. Subcutaneous injection of OV202 Sh1 cells resulted in tumor formation in nude mice, whereas HSulf-1 expressing OV202 NTC cells did not form tumors [133]. Both cells were grown in minimum essential medium alpha 1X (Cellgro) supplemented with *20%* fetal bovine serum (Biowest) and *1%* penicillin-streptomycin (Cellgro). All cells were grown in the presence of 1 µg/ml puromycin as a selection marker for the HSulf-1 shRNA cells were treated with 10 µl of AACOCF3 or

MAFP (cPLA2 inhibitors; Cayman chemicals) for 24 hours. Following this treatment, cells were washed twice with PBS and then fixed in Trump's fixative containing *4%* formaldehyde and *1%* glutaraldehyde in phosphate buffer pH ~7.3, post-fixed in *1.0%* OsO4, dehydrated with ethanol gradation, and transitioned into propylene oxide for infiltration and embedding into super epoxy resin.

5.2.2.2 TEM imaging

Cell samples were fixed in Trump's fixative (pH 7.2) at 4°C overnight, spun down and the supernatant removed. They were re-suspended in agarose which was cooled and solidified. The cells in agarose were then post-fixed in *1%* OsO4, dehydrated through a graded series of ethanol, and embedded in Spurr resin. *100nm* (or $0.1\mu m$) ultra-thin sections were mounted on 200-mesh copper grids, post-stained with lead citrate, and observed under a JEOL JEM-1400 transmission electron microscope at 80kV.

5.3 Results and discussions

The TEM images of the ovarian cancer cells are obtained as described in the above section. IPR analyses were performed for the samples on different length scales of TEM images. The IPR averaging of a sample length L, $<<IPR(L)>>$ over a single cell, then over the different cells, was performed for obtaining the ensemble averaging: $<<IPR(L)>>=<<IPR(L)>_{L\times L}>$. As discussed above, the $<<IPR(L)>>$ value for each TEM image was calculated and provides the degree of the structural disorder strength at a defined length scale L.

Fig. 5.1(a)-(d) are the representative grayscale TEM images of a thin section (~*100nm*) of a cell from the following ovarian control/cancer cell lines: (i) non-tumorous NTC, (ii) tumorous Sh1, (iii) Sh1 treated with drug AACOCF3 (Sh1-AACOCF3), and (iv) Sh1 treated with drug

MAPF (Sh1-MAFP). For each case (i.e. for a particular cell line) study, 8 different cells were taken from the cell line for averaging. Figure 5.1(a')-(d') are the corresponding $\sigma(<IPR(L)>)$ images of Fig. 5.1(a)-(d), at a length scale of $165nm$ and sample size of $165\times165nm^2$. It is reported that structural alteration in carcinogenesis happens around sample length $L\sim100nm$ or sample size $L\times L$ [127], which is around the basic building blocks of the cell. Therefore, we have taken a length scale of $165nm$ which is higher than $100nm$. For a better understanding of the IPR images at different length scales, we have also added IPR images at two different length scales (one $82nm<100nm$ and another $206nm>100$ and $165nm$), in the Supplementary Documents. As can be seen from Figure 5.1, $\sigma(<IPR(L)>)$ images represent different intensities of disorder patterns in the cell line which are distinct from conventional grayscale TEM images. In the IPR images, intensities patterns of higher fluctuations in the cells are represented by the red spots and lower intensities with blue. In the figure, it can be seen that the increasing fluctuation or $\sigma(<IPR(L)>)$ value increases from the less proliferating NTC cells to highly proliferating Sh1 cells and decreasing of the fluctuations or $\sigma(<IPR(L)>)$ values decrease with the treatment of two different anti-cancerous drugs, AACOCF3 and MAFP. The drug effect can be distinctly visualized in the IPR images.

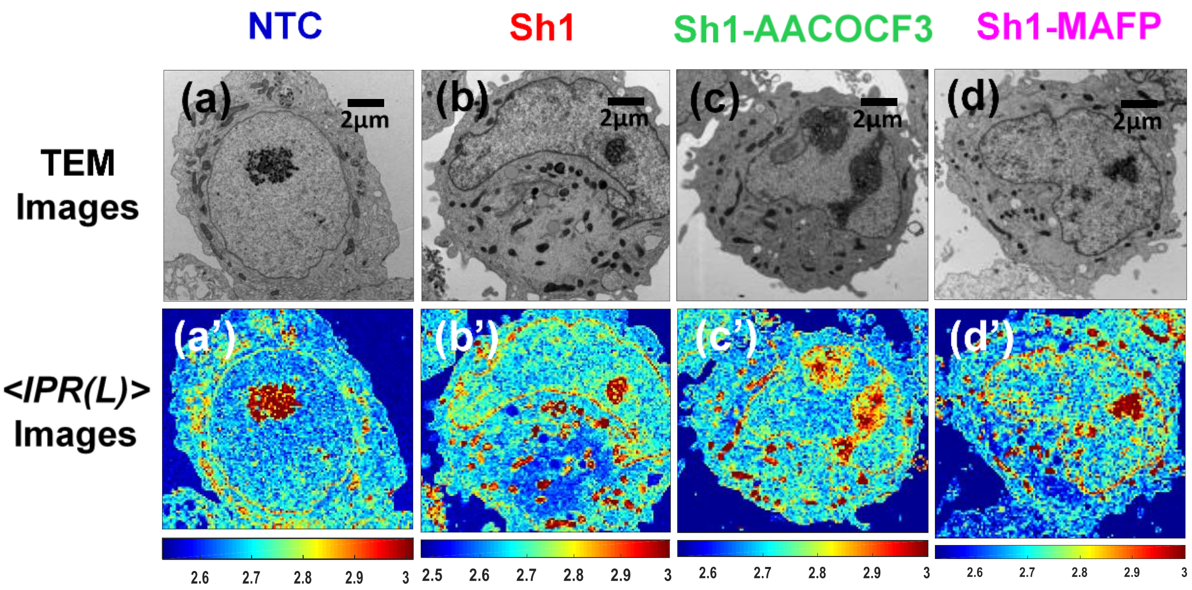

Figure 5.1 TEM and IPR images of anti-cancerous drugs treated ovarian cancer cells.

(a)-(d) are the TEM images and (a')-(d') are their respective IPR images at the sample length ($L\times L=165\times165nm^2$) from ovarian cells of the following: non-tumorous (OV202 NTC); tumorous (OV202 Sh1); AACOCF3 treated tumorous Sh1, Sh1-AACOCF3; and MAFP treated tumorous Sh1 Sh1-MAFP. IPR images are distinct from the TEM images.

TEM images and their corresponding IPR images for representative ovarian cancer cases (NTC, Sh1, Sh1-AACOCF3, and Sh1-MAFP) at two different sample lengths: one *82nm <100nm or 165nm* and another *206nm>100nm* or *165nm,* are presented for the better clarification. It has been reported that structural changes are significant around *100nm* and in this particular experiment as seen from Fig. 5.2 prominent changes start around *150nm*. Therefore, we have taken sample length *165nm* to study the anti-cancerous drug effect in ovarian cancer cells. Here, from the presented IPR image at different length scales it can be seen that IPR images show more fluctuations above ~*100nm* and lower for smaller length scales.

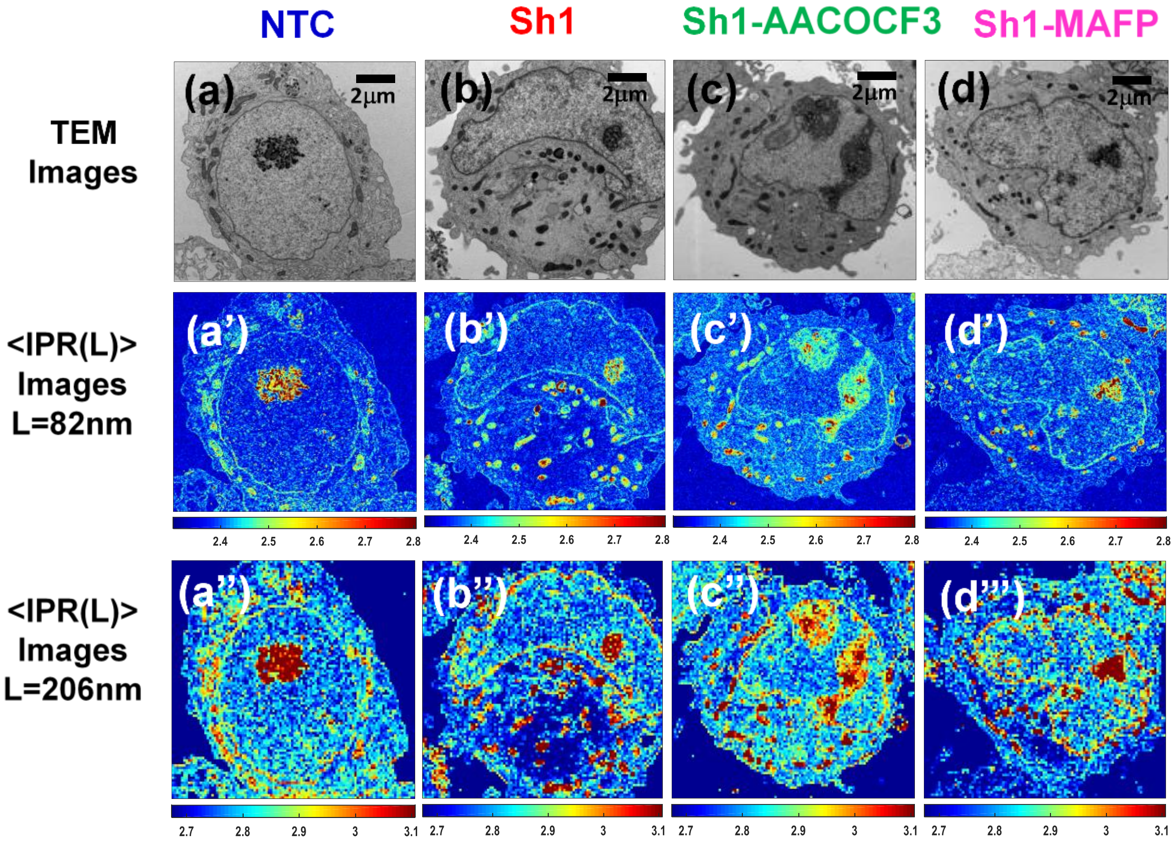

Figure 5.2 TEM and IPR images of ovarian cancer cells at different length scales.

(a)-(d) are the TEM images, while (a')-(d'), and (a'')-(b'') are their respective IPR images at the sample length *(L)* [$L\times L=82\times 82nm^2$, *and* $L\times L=206\times 206nm^2$] below and above the presented IPR image at sample length, $L = 165nm$ respectively from ovarian cells of the following: non-tumorous (OV202 NTC); tumorous (OV202 Sh1); AACOCF3 treated tumorous Sh1, Sh-AACOCF3; and MAFP treated tumorous Sh1 Sh1-MAFP. IPR images are distinct from the TEM images.

Fig. 5.3 shows the length (L) dependent fluctuations with the sample size ($L\times L$). We plotted, variations of the standard deviation $\sigma(<IPR(L)>)$ vs L with the increase of sample lengths: $L = 41, 82, 123, 165, 206, 247, 288$ *nm*. As the deviation started appearing in the mean and STD of $<IPR(L)>_{L\times L}$, at $L=100nm$, therefore we have plotted the $\sigma(<IPR(L)>)$ vs L, systematically well below and above 100nm. These lengths are for the cells from the following cell lines: non-tumorigenic (OV202 NTC); tumorigenic (OV202 Sh1); AACOCF3 treated tumorigenic Sh1 (Sh1-AACOCF3); and MAFP treated tumorous Sh1 (Sh1-MAFP). As can be seen from the figure that the deviation in the degree of nano-fluctuations between non-tumorigenic cells NCT and tumorigenic cells Sh1 started becoming prominent around the length scale *~100nm*. Interestingly, the degree of nano-fluctuations of anti-cancerous drugs treated Sh1 tumorigenic cells reverse to that of the non-tumorigenic NTC cells. This confirms the efficacy of these two anti-cancerous drugs.

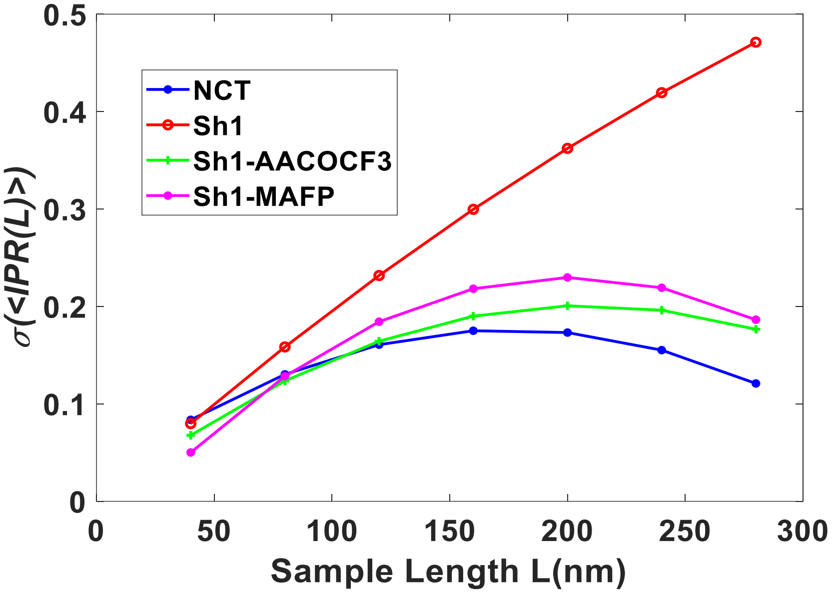

Figure 5.3 Sample length scale (L) dependence of σ*(<IPR(L)>)*.

Variations of the standard deviation σ*(<IPR(L)>)* with the increase of sample length *L*, for cell lines non-tumorigenic (OV202 NTC); tumorigenic (OV202 Sh1); AACOCF3 treated tumorigenic Sh1 (Sh1-AACOCF3); and MAFP treated tumorous Sh1 (Sh1-MAFP). It can be seen that the deviation between NTC and Sh1 started to become prominent around the sample length/length scale *~100nm*. Interestingly, the drug-treated Sh1 tumorigenic cells' fluctuation degrees reverse to the non-tumorigenic cells.

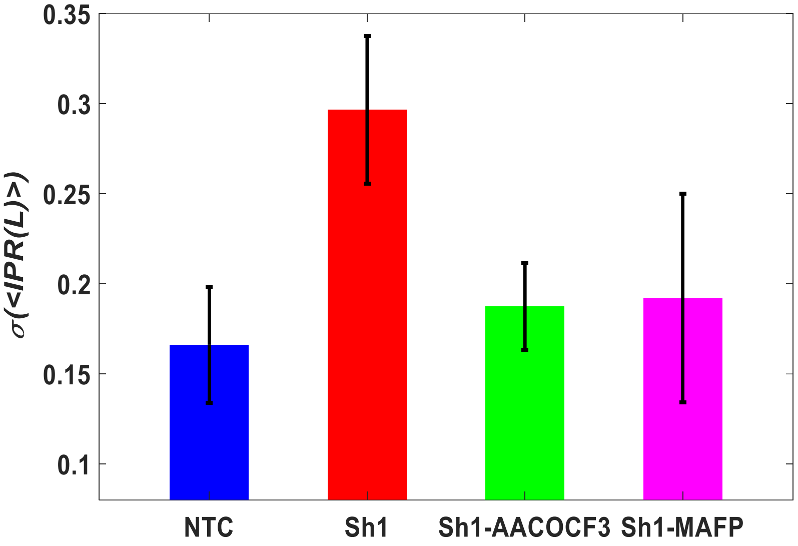

Figure 5.4 Bar graph representation of anti-cancerous drug-treated ovarian cancer cells

Bar graph representation of the standard deviation of the degree of structural disorder strength L_d $\sim\sigma(<IPR(L)>)$ calculated from the TEM images for: non-tumorous (NTC), tumorous (Sh1), AACOCF3 treated tumorous cells Sh1-AACOCF3, and MAFP treated tumorous cells Sh1-MAFP. For the normal cells, IPR analysis was performed at the sample size $165\times165nm^2$. The result shows L_d value increases from non-tumorous to tumorous cells, then it decreases when these tumorous cells are further treated with anti-cancerous drugs AACOCF3 and MAFP, interestingly the L_d value returns almost back to the same value of the non-tumorous cells (p-values $< .05$). This may imply that anti-cancerous drugs are working well in ovarian cancer treatment.

Figure 5.4 presents the bar graphs of the standard deviation of calculated $\sigma(<IPR>)$ or (L_d) value, of the ovarian cells at the fixed-length scale of *165nm*. The variations are similar at lower sample length scales *>165nm*, however, we have chosen *165nm* to show a prominent difference. Statistically, the standard deviation is the more reliable marker than the average, as it only depends on the width of the distribution, irrespective of the mean position. The result shows the standard deviation of the degree of structural disorder $\sigma(<IPR>)$ value increased by 70% from NTC to Sh1 cells. Furthermore, when Sh1 cells were treated with 2 different anti-cancerous drugs, AACOCF3 and MAFP, the $\sigma(<IPR>)$ values decreased by around 58% for AACOCF3 and 54% for MAFP, relative to the $\sigma(<IPR>)$ value of the Sh1 tumorous cells. In particular, with the treatment of the anti-cancerous drug, the structural biomarker parameter $\sigma(<IPR>)$ or L_d value decreased nearly back to the normal value. The normalcy detection of these anti-cancerous drug-treated cancerous cells may require further investigations using different modalities. It has been earlier shown that AACOCF3 is a better anti-cancerous agent producing more anti-cancerous effects in OC cells compared to MAFP [135]. It can be seen in Fig. 5.4 that similar trend of bar graphs which show a reduction in the degree of structural disorder $\sigma(<IPR>)$ value for AACOCF3 (58%) > MAFP (54%), consistent with the known qualities of the drugs, in this length scale. Hence, the quantitative analysis technique, called IPR, quantifies the nanoscale structural disorder $\sigma(<IPR>)$ or L_d, as an important biomarker to study the structural alterations at the nanoscale level and has the potential to detect the effect of anti-cancerous drugs in carcinogenesis ovarian cancer.

5.4 Conclusions

The nanoscale mass-density fluctuations are quantified with the progression of ovarian carcinogenesis, as well as the effects of two anti-cancerous drugs on non-tumor forming OV202NTC and tumor forming OV202Sh1 cells are studied using the TEM imaging and IPR technique. TEM experiment has a resolution of ~1nm and can identify the nanoscale architectural alterations inside the cells which take place in normal cells due to the rearrangement of the very basic building blocks of the cells, such as DNA, RNA, lipids, macromolecules, etc.

This results in nanoscale mass density fluctuations in the cells which can be probe using TEM imaging. The nanoscale fluctuations are quantified by the STD value of the $<IPR(L)>_{L\times L}$, $\sigma(<IPR(L)>)_{cell}$, performed over similar types of cells or ensembles of the samples. Results show an increase in the nanoscale fluctuations or $\sigma(<IPR(L)>)$ value from non-tumorous NTC to tumorous Sh1 cells. The $\sigma(<IPR(L)>)$ values for two different drugs treated tumorous cells, Sh1-AACOCF3 and Sh1-MAFP, have reduced value from tumorous cells Sh1 and the reduced values are nearly the same to the NTC non-tumorous cells. Earlier IPR analysis of a different cell line has verified the increase of nanoscale structural disorder with the progression of cancer [22,23]. Based on the results presented, we investigate the potential applications of the IPR technique in measuring and quantifying the effectiveness of different anti-cancerous drugs on ovarian cancer treatment. This quantification of the effectiveness of anti-cancerous drugs in ovarian cancer treatment could enhance better drug treatment modalities at their earliest and helps to control the deadly ovarian cancer. Although this study is based on ovarian cancer cells, however, the technique can be applied to the varieties of cancers to assess the effectiveness of different anti-cancerous drugs in treatment.

Our technique is based on the linear transmission of the TEM intensity through thin cell samples as described in the Method. The TEM intensity transmits well till *~500nm* of thin cell samples, the technique works until that thickness of the samples. Because of the thin sample, this method can be applied to heterogeneous cell samples.

A cell is around 5 microns thick, and the TEM sample thickness is around *100nm*, therefore, 50 TEM slices per cell can be generated. Thus, it is important to consider ensemble averaging correctly by choosing similar types of TEM micrographs. For each cell, TEM micrographs are chosen around the middle of the cell by observing the maximum size of the

nucleus. The maximum changes in a cancerous cell can be captured by considering the largest portion of the cell or nucleus. Not considering proper ensemble averaging, results may vary.
At present, the super-resolution optical microscopy techniques have achieved an order of *5-10nm* resolutions targeting particular types of molecules in a cell [136–138]. However, in the case of TEM imaging, we can target whole cells or nuclei with ~*1nm* resolution. This nanoscale resolution brings advantages of the TEM imaging for the quantification of structural disorder and its alterations at submicron to nanoscales in the nucleus/cell, in progressive carcinogenesis, or any other cell abnormalities. It would be interesting to compare the results of TEM-IPR analysis with the super-resolution microscopy in progressive carcinogenesis or abnormalities of a cell, in a near future.

CHAPTER VI

CONCLUSIONS AND FUTURE WORK

The elastic light scattering signal from cells/tissues can be recorded after propagating through the cells/tissues which carries tremendous information useful for cancer diagnosis and to study drug effects in cancer treatment or any other abnormalities. The 1D backscattered signals are sensitive to refractive index fluctuations at any length scale including way below the wavelength range. Furthermore, we have studied molecular-specific light localization techniques using TEM and confocal imaging, a powerful method to quantify molecular-specific changes in the mass density of refractive index fluctuation in cells/tissues. In this dissertation, using both PWS (open scattering) and IPR (close scattering) techniques, we probe the structural alteration of the cells/tissues and quantify the degree of structural disorder to study cancer stages, drug effects in cancer treatment, and chronic alcoholic brain abnormalities.

With the addition of finer focusing using a highly sensitive 3D motorized scanning stage in the developed PWS technique (resolution ~40nm), we have shown that these backscattered signals from cells/tissues are sensitive to refractive index fluctuations below the wavelength within the diffraction limit and can distinguish the stages of progressive cancer in TMA. The result also demonstrates that the use of low NA illumination prevents interference between the 1D adjacent channels, increasing the sensitivity of the technique to nanoscale refractive index fluctuations. Likewise, the PWS quantification of 3D structure tumor developed from cancer cells 2D structure reflects the unique ability of PWS to study the anti-cancerous drug effect in cancer treatment. On the other hand, we quantify refractive index or mass density fluctuations in a closed weakly disordered heterogeneous optical system based on light localization technique using confocal and TEM imaging. In the case of carcinogenesis or any other abnormalities, DNA molecules inside the cells undergo structural alteration due to the mass density variation and rearrangements which result in the light wave eigenfunction localization. This results in nano to microscale structural alteration which can be detected based on a molecular specific light localization technique using a confocal image as demonstrated by quantifying probiotic effect in alcoholic brain cells. Our results also show that the TEM micrograph can be effectively used to quantify the molecular specific mass density fluctuations in terms of the degree of disorder strength using the IPR technique to detect carcinogenesis and drug effect in cancer treatment.

In this chapter, a summary of the developed spectroscopic systems, in a bid to elucidate the promising applications of these techniques are reported. In addition to this near-future studies and recommendations using these techniques are presented.

6.1 PWS study conclusions

The developed finer focusing mesoscopic physics-based imaging technique, PWS can scatter precise scattering volume to detect minute structural changes in terms of the refractive index fluctuations below the sub-diffraction length scale, within the diffraction limit. In this dissertation, the finer focusing PWS technique was successfully used to quantify the degree of disorder strength (L_d) and distinguished the stages of cancer in commercially available paraffin-embedded deadly cancer TMAs. This result could help to standardized cancer diagnostic modalities and use these samples to study the drug effect in cancer treatment. With the validation of added finer focusing, our results demonstrate that PWS was able to differentiate different stages of cancer, especially for paraffin-embedded pancreatic, breast, colon, and prostate cancer tissues. The PWS result shows that for each TMA cancer tissue, the degree of disorder strength increases significantly with an increase in cancer stages for each cancer type supporting the fact that mass density fluctuations or refractive index fluctuations increase in progressive cancer. Lastly, the flexibility provided by the highly sensitive PWS technique and commercially available TMA samples to distinguish the cancer stages opens a broad path to explore for generalizing the structural changes in progressive cancer and drug effect for effective cancer treatment/diagnosis.

In addition to this, the structural properties of tumors developed by the xenografting of drug-sensitive and drug-resistive prostate cancer (PC) cell lines were quantified using the finer focusing PWS technique. The results indicate that tumor tissues (3D model) grown by xenografting PC cells (2D model) resistant toward docetaxel have a higher degree of disorder strength (L_d) than drug-sensitive PC cells. Cancerous cells that survived through drug exposure are more aggressive and develop different morphological structures resulting in higher mass density fluctuation due to the rearrangement of macromolecules, large pore sizes, changes in cytoskeleton nanoarchitecture. This result further concludes that xenografted tumors from the drug-sensitive and drug-resistant PC cell lines maintain the same type of structural properties when grown to 3D structures supporting a strong correlation in structural properties of cells grown on 2D glass slide structure surfaces. Therefore, the PWS study of xenografted tumor 3D structures that replicate the structural properties of cancer cells could be a reliable, easy, and quantitative approach to diagnose chemo-resistance for the future. This promising result seeks an application to monitor the effect of chemotherapy drugs on a different level of tumorigenicity by both *in-vitro* and *in-vivo* analysis.

6.2 Future work in PWS and its applications

The PWS microscopic setup developed in this work is highly sensitive, fast, and cost-effective. The results obtained from the engineered PWS technique may have profound biological and medical implications. In the fields of cancer biology and medicine, the PWS technique could help us to understand the structural properties of cancerous cells/tissues as well as chemotherapy or anti-cancerous drug effects in cancerous cells/tissues at the nanoscale level which need to be explored in detail. Monitoring the growth of cancerous cells/tissues with or without anti-cancerous drugs using the PWS technique and xenograft model for different types of cancer could play a crucial role in cancer control in the coming days. The quantification of structural changes in cells/tissues due to abnormalities such as radiation exposure, alcohol, stress, etc. might also be interesting to study next with PWS. At this point, it may not be possible to identify which specific structure is responsible for an increase in the degree of disorder strength (L_d) and associated with molecular mechanism, however, we can have some insight into how these nanoscale structural changes are associated with cancer progression and anti-cancerous drug treatments. And the improvement in the construction of the disorder map or L_d map with the reduced noise performance in the short interval of time could provide an opportunity to visualize which part is specifically affected by the diseases. Further, the flexibility provided by the spectroscopic technique using commercially available TMA samples to standardize the early cancer diagnostic and study the drug effect in cancerous treatment opens exploration for generalizing the structural change in progressive cancer for effective cancer treatment. With these promising applications of PWS in biomedical implications, we want to move forward with the PWS technique from clinical research to clinical trials especially to study drug-sensitive and drug-resistive different cancer treatment cases.

In addition to this, we can work on the PWS instrumentation to increase the sensitivity of the system and make it more compatible with the in-hospital application. For this, we can use a highly sensitive and compatible liquid crystal tunable filter with less than 1nm resolution and replace the existing CCD camera with a low cooling effect and high quantum efficiency (QE) CCD camera. Also, we can replace the existing 3D motorized scanning stage with a highly sensitive stage for precise focusing within the working distance of the low NA objective. To make this technique compatible with both *in-vitro* and *in-vivo* diagnostic we can replace the light source and combination of lenses as mentioned in Chapter I Section 1.1.1 with optical fibers and develop the system in a portable microscopic setup, that can be used *in-vivo*. We are planning to modify the existing BX61 bright field microscope replacing the existing light source with an optical fiber-based halogen lamp (100W) light source and mounting an LCTF filter coupled with a Retiga 3 CCD camera on the top of a microscope to capture the spectroscopic images. That means, we want to validate the possibility of using a spectrum of the averaged spatial information measuring the backscattered signal through an optical fiber. This will modify the table-top PWS system to a compact real-time diagnosis microscopic system. These changes can help to develop this system as a commercial product for early, effective, and real-time diagnosis of cancer or any other abnormalities in cells/tissue for the future.

6.3 IPR study conclusions

We have developed the novel approach based on mesoscopic physics-based light localization properties, IPR technique to quantify the nano to submicron scale mass density or refractive index fluctuations in a weakly disordered medium using TEM and Confocal imaging. The main advantage of the Confocal-IPR technique is that we can probe and quantify a molecular-specific spatial mass density structural change. In this work, we mainly use the

Confocal-IPR and TEM-IPR techniques to probe nanoscale mass density fluctuations in the cells/tissues to study cancer, drug effects, or and brain abnormalities using a mouse model. First, the confocal-IPR technique was used to study the effect of probiotics in chronic alcoholic brain cells/components targeting it with different dyes/proteins. Interestingly, the IPR result shows that the statistical parameter standard deviation of the average IPR, $\sigma(<IPR(L)>)$ or the disorder strength (L_d) increase in chronic alcohol-treated glial cells and chromatin of mice brain tissues while decreasing gradually when treated with probiotics (*L. Plantarum*) simultaneously. Here, an increase in the molecular specific degree of disorder strength (L_d) of chronic alcoholic mice brain glial cells, and chromatin might be due to the adverse effect of alcohol in brain cells which initially shows effects on the submicron scale quantified by the Confocal-IPR technique. Whereas alcoholic brains see an improved cognitive function in the presence of probiotics, *L. Plantarum*, which may help in soothing the brain cell's structure resulting in decreasing the disorder strength (L_d). In conclusion, the reversible effect of probiotics in alcoholic brain cells/components could be a useful way to mitigate abnormalities in the brain due to alcohol, stress, or any other sedative drugs that need to be explored using this molecular specific light localization technique.

Further, using TEM imaging we can target whole cells or nuclei with *~1nm* resolution which facilitates the real view of the cell structures at the nanoscale which cannot be performed by a standard optical microscope. Thus, with the TEM-IPR technique, the nanoscale mass-density or refractive index fluctuations in ovarian cancerous cells, as well as anti-cancerous drug effects on non-tumor forming OV202NTC and tumor forming OV202Sh1 cells, are quantified. Results show an increase in the standard deviation of mass density fluctuations or $\sigma(<IPR(L)>)_{cells}$ value from non-tumorous NTC to tumorous Sh1 cells while the

$\sigma(<IPR(L)>)_{cells}$ for two different drugs treated tumorous ovarian cells, Sh1-AACOCF3 and Sh1-MAFP, reduces from tumorous cells Sh1 nearly the same to the NTC non-tumorous cells. This quantification of the effectiveness of anti-cancerous drugs in ovarian cancer treatment using TEM-IPR could enhance better drug treatment modalities at its earliest. Although this study is based on ovarian cancer, however, the technique can be applied to the different cancerous cells to quantify the effectiveness of different anti-cancerous drugs in cancer treatment. Also, this method shows the effectiveness of the developed IPR method at the nanoscale level. Therefore, the proposed model is completely based on quantitative analysis and could be the most reliable method to study the drug effect in cancer treatment in the future.

6.4 Future work in IPR and its applications

The proposed novel approach of mesoscopic physics-based molecular specific light localization technique, IPR, using the TEM and confocal images can quantify the nano to submicron scale mass density fluctuations and provides numerical means to distinguish cancer, drug-effect in cancer treatment, or brain abnormalities. The complication in sample preparation and huge instrumentation setup of TEM which can probe samples up to ~1nm shows a potential application for the future to quantify the structural properties of different types of cancerous cells and the efficacy of drug effect in cancer treatment combining with IPR technique. Also, a further improved molecular mass density specific IPR map with a reduced noise could help us locate the most affected region in cells with cancer or any other abnormalities. This quantitative IPR technique will be more useful to the pathologist who uses stained cells/tissues for cancer screening, grade classification, and study drug-effect visualizing constructed IPR images.

The IPR technique is universal to probe the structural disorder. Initially, it was used for cancer diagnosis, however, now we have extended and used it to probe brain abnormalities due to stress, Alzheimer's, or alcohol using confocal imaging. The novel approach of studying probiotics' effect in the alcoholic brain where probiotics are used to soothe and increase the cognitive function of the brain can be quantified using a confocal-IPR technique for different types of commercially available probiotics to understand their effect on the brain cells/tissues. This will help to select the right probiotics at their earliest to enhance the cognitive function of the alcoholic brain before being too late for treatment, at this clinical research moment. Based on the results obtained for alcoholic brain tissue, we can elaborate our study using the confocal-IPR technique to study the structural change in brain cells/tissues at the nanoscale level due to stress, depression, and Alzheimer's in a mouse model. Recently developed super-resolution microscopy has a significant interest in imaging nanoarchitecture which can reach the sensitivity up to 5 nm. In the near future, we want to develop an algorithm based on mesoscopic physics-based light localization technique to quantify the structural properties in cells/tissues using super-resolution microscopy images and compare the obtained result with the existing TEM-IPR and confocal-IPR results. We believe that this might help us to better understand the structural properties in cells/tissue at the nanoscale level.

In summary, this research presents a key finding that the quantification of spatial structural disorder of the weakly disordered medium such as cells/tissues based on mesoscopic light transportation and light localization approaches are a promising technique to characterize early carcinogenesis, drug-effect, or brain abnormalities. Of course, the main goal of this research will direct the improvements in these spectroscopic techniques to use them in a clinical setting in a hospital, and further with large-scale clinical trials. At this point, it demands further extensive studies in larger sample sizes and clinical trials to achieve the goal of cancer diagnosis and treatment in the future.

REFERENCES

1. V. Backman, M. B. Wallace, L. T. Perelman, J. T. Arendt, R. Gurjar, M. G. Müller, Q. Zhang, G. Zonios, E. Kline, T. McGillican, S. Shapshay, T. Valdez, K. Badizadegan, J. M. Crawford, M. Fitzmaurice, S. Kabani, H. S. Levin, M. Seiler, R. R. Dasari, I. Itzkan, J. Van Dam, and M. S. Feld, "Detection of preinvasive cancer cells," Nature **406**, 35–36 (2000).

2. S. L. Jacques, J. C. Ramella-Roman, and K. Lee, "Imaging skin pathology with polarized light," J Biomed Opt **7**, 329–340 (2002).

3. Y. L. Kim, Yang Liu, R. K. Wali, H. K. Roy, M. J. Goldberg, A. K. Kromin, Kun Chen, and V. Backman, "Simultaneous measurement of angular and spectral properties of light scattering for characterization of tissue microarchitecture and its alteration in early precancer," IEEE Journal of Selected Topics in Quantum Electronics **9**, 243–256 (2003).

4. Q. Liu and N. Ramanujam, "Experimental proof of the feasibility of using an angled fiber-optic probe for depth-sensitive fluorescence spectroscopy of turbid media," Opt. Lett., OL **29**, 2034–2036 (2004).

5. J. R. Mourant, I. J. Bigio, J. Boyer, R. L. Conn, T. Johnson, and T. Shimada, "Spectroscopic diagnosis of bladder cancer with elastic light scattering," Lasers in Surgery and Medicine **17**, 350–357 (1995).

6. L. T. Perelman, V. Backman, M. Wallace, G. Zonios, R. Manoharan, A. Nusrat, S. Shields, M. Seiler, C. Lima, T. Hamano, I. Itzkan, J. Van Dam, J. M. Crawford, and M. S. Feld, "Observation of Periodic Fine Structure in Reflectance from Biological Tissue: A New Technique for Measuring Nuclear Size Distribution," Phys. Rev. Lett. **80**, 627–630 (1998).

7. D. L. Conover, B. M. Fenton, T. H. Foster, and E. L. Hull, "An evaluation of near infrared spectroscopy and cryospectrophotometry estimates of haemoglobin oxygen saturation in a rodent mammary tumour model," Phys Med Biol **45**, 2685–2700 (2000).

8. M. G. Nichols, E. L. Hull, and T. H. Foster, "Design and testing of a white-light, steady-state diffuse reflectance spectrometer for determination of optical properties of highly scattering systems," Appl. Opt., AO **36**, 93–104 (1997).

9. S. G. Demos and R. R. Alfano, "Optical polarization imaging," Appl. Opt., AO **36**, 150–155 (1997).

10. A. Wax, C. Yang, V. Backman, K. Badizadegan, C. W. Boone, R. R. Dasari, and M. S. Feld, "Cellular organization and substructure measured using angle-resolved low-coherence interferometry.," Biophys J **82**, 2256–2264 (2002).

11. Xu Li, A. Taflove, and V. Backman, "Recent progress in exact and reduced-order modeling of light-scattering properties of complex structures," IEEE Journal of Selected Topics in Quantum Electronics **11**, 759–765 (2005).

12. Y. L. Kim, Y. Liu, V. M. Turzhitsky, H. K. R. M.d, R. K. Wali, H. Subramanian, P. Pradhan, and V. Backman, "Low-coherence enhanced backscattering: review of principles and applications for colon cancer screening," JBO **11**, 041125 (2006).

13. Y. Liu, R. E. Brand, V. Turzhitsky, Y. L. Kim, H. K. Roy, N. Hasabou, C. Sturgis, D. Shah, C. Hall, and V. Backman, "Optical Markers in Duodenal Mucosa Predict the Presence of Pancreatic Cancer," Clin Cancer Res **13**, 4392–4399 (2007).

14. R. S. Gurjar, V. Backman, L. T. Perelman, I. Georgakoudi, K. Badizadegan, I. Itzkan, R. R. Dasari, and M. S. Feld, "Imaging human epithelial properties with polarized light-scattering spectroscopy," Nature Medicine **7**, 1245–1248 (2001).

15. H. Subramanian, H. K. Roy, P. Pradhan, M. J. Goldberg, J. Muldoon, R. E. Brand, C. Sturgis, T. Hensing, D. Ray, A. Bogojevic, J. Mohammed, J.-S. Chang, and V. Backman, "Nanoscale cellular changes in field carcinogenesis detected by partial wave spectroscopy," Cancer Res **69**, 5357–5363 (2009).

16. H. Subramanian, P. Pradhan, Y. Liu, I. R. Capoglu, X. Li, J. D. Rogers, A. Heifetz, D. Kunte, H. K. Roy, A. Taflove, and V. Backman, "Optical methodology for detecting histologically unapparent nanoscale consequences of genetic alterations in biological cells," PNAS **105**, 20118–20123 (2008).

17. H. Subramanian, P. Pradhan, Y. Liu, I. R. Capoglu, J. D. Rogers, H. K. Roy, R. E. Brand, and V. Backman, "Partial wave microscopic spectroscopy detects sub-wavelength refractive index fluctuations: an application to cancer diagnosis," Opt Lett **34**, 518–520 (2009).

18. P. Adhikari, P. K. Shukla, H. M. Ghimire, M. Hasan, P. Sahay, H. Almabadi, V. Tripathi, O. Skalli, R. Rao, and P. Pradhan, "TEM study of chronic alcoholism effects on early carcinogenesis by probing the nanoscale structural alterations of cell nuclei," Phys. Biol. **18**, 026001 (2021).

19. P. Pradhan and N. Kumar, "Localization of light in coherently amplifying random media," Phys. Rev. B **50**, 9644–9647 (1994).

20. S. B. Haley and P. Erdös, "Wave propagation in one-dimensional disordered structures," Phys. Rev. B **45**, 8572–8584 (1992).

21. R. Rammal and B. Douçot, "Invariant imbedding approach to localization. I. General framework and basic equations," Journal de Physique **48**, 509–526 (1987).

22. P. Pradhan, D. Damania, H. M. Joshi, V. Turzhitsky, H. Subramanian, H. K. Roy, A. Taflove, V. P. Dravid, and V. Backman, "Quantification of nanoscale density fluctuations using electron microscopy: Light-localization properties of biological cells," Appl. Phys. Lett. **97**, 243704 (2010).

23. P. Pradhan, D. Damania, H. M. Joshi, V. Turzhitsky, H. Subramanian, H. K. Roy, A. Taflove, V. P. Dravid, and V. Backman, "Quantification of nanoscale density fluctuations by electron microscopy: probing cellular alterations in early carcinogenesis," Phys. Biol. **8**, 026012 (2011).

24. P. W. Anderson, D. J. Thouless, E. Abrahams, and D. S. Fisher, "New method for a scaling theory of localization," Phys. Rev. B **22**, 3519–3526 (1980).

25. A. A. Abrikosov and I. A. Ryzhkin, "Conductivity of quasi-one-dimensional metal systems," Advances in Physics **27**, 147–230 (1978).

26. N. Kumar, "Resistance fluctuation in a one-dimensional conductor with static disorder," Phys. Rev. B **31**, 5513–5515 (1985).

27. P. W. Anderson, "Absence of Diffusion in Certain Random Lattices," Phys. Rev. **109**, 1492–1505 (1958).

28. P. A. Lee and T. V. Ramakrishnan, "Disordered electronic systems," Rev. Mod. Phys. **57**, 287–337 (1985).

29. E. Abrahams, P. W. Anderson, D. C. Licciardello, and T. V. Ramakrishnan, "Scaling Theory of Localization: Absence of Quantum Diffusion in Two Dimensions," Phys. Rev. Lett. **42**, 673–676 (1979).

30. B. Kramer and A. MacKinnon, "Localization: theory and experiment," Rep. Prog. Phys. **56**, 1469–1564 (1993).

31. N. F. Mott and W. D. Twose, "The theory of impurity conduction," Advances in Physics **10**, 107–163 (1961).

32. P. Pradhan and S. Sridhar, "Correlations due to Localization in Quantum Eigenfunctions of Disordered Microwave Cavities," Phys. Rev. Lett. **85**, 2360–2363 (2000).

33. P. Pradhan and S. Sridhar, "From chaos to disorder: Statistics of the eigenfunctions of microwave cavities," Pramana - J Phys **58**, 333–341 (2002).

34. T. Schwartz, G. Bartal, S. Fishman, and M. Segev, "Transport and Anderson localization in disordered two-dimensional photonic lattices," Nature **446**, 52–55 (2007).

35. J. M. Schmitt and G. Kumar, "Turbulent nature of refractive-index variations in biological tissue," Opt. Lett., OL **21**, 1310–1312 (1996).

36. C. J. R. Sheppard, "Fractal model of light scattering in biological tissue and cells," Opt. Lett., OL **32**, 142–144 (2007).

37. J. S. Kim, P. Pradhan, V. Backman, and I. Szleifer, "The influence of chromosome density variations on the increase in nuclear disorder strength in carcinogenesis," Phys. Biol. **8**, 015004 (2011).

38. P. Sahay, H. M. Almabadi, H. M. Ghimire, O. Skalli, and P. Pradhan, "Light localization properties of weakly disordered optical media using confocal microscopy: application to cancer detection," Opt. Express, OE **25**, 15428–15440 (2017).

39. S. John, "Localization of Light," Physics Today **44**, 32 (2008).

40. D. M. Shotton, "Confocal scanning optical microscopy and its applications for biological specimens," Journal of Cell Science **94**, 175–206 (1989).

41. P. Kask, K. Palo, D. Ullmann, and K. Gall, "Fluorescence-intensity distribution analysis and its application in biomolecular detection technology," PNAS **96**, 13756–13761 (1999).

42. B. Matsumoto, *Cell Biological Applications of Confocal Microscopy*, 2nd ed. (Elsevier, 2003).

43. D. B. Williams and C. B. Carter, *Transmission Electron Microscopy: A Textbook for Materials Science*, 2nd ed. (Springer US, 2009).

44. L. Reimer, *Scanning Electron Microscopy: Physics of Image Formation and Microanalysis*, 2nd ed., Springer Series in Optical Sciences (Springer-Verlag, 1998).

45. J. Liu, "Scanning transmission electron microscopy and its application to the study of nanoparticles and nanoparticle systems," Journal of Electron Microscopy **54**, 251–278 (2005).

46. V. N. Prigodin and B. L. Altshuler, "Long-Range Spatial Correlations of Eigenfunctions in Quantum Disordered Systems," Phys. Rev. Lett. **80**, 1944–1947 (1998).

47. N. C. Murphy, R. Wortis, and W. A. Atkinson, "Generalized inverse participation ratio as a possible measure of localization for interacting systems," Phys. Rev. B **83**, 184206 (2011).

48. L. Cherkezyan, I. Capoglu, H. Subramanian, J. D. Rogers, D. Damania, A. Taflove, and V. Backman, "Interferometric spectroscopy of scattered light can quantify the statistics of subdiffractional refractive-index fluctuations," Phys Rev Lett **111**, 033903 (2013).

49. D. Lu and Z. Liu, "Hyperlenses and metalenses for far-field super-resolution imaging," Nature Communications **3**, 1205 (2012).

50. A. Sentenac, P. C. Chaumet, and K. Belkebir, "Beyond the Rayleigh Criterion: Grating Assisted Far-Field Optical Diffraction Tomography," Phys. Rev. Lett. **97**, 243901 (2006).

51. S. W. Hell, "Far-Field Optical Nanoscopy," Science **316**, 1153–1158 (2007).

52. B. Huang, W. Wang, M. Bates, and X. Zhuang, "Three-Dimensional Super-Resolution Imaging by Stochastic Optical Reconstruction Microscopy," Science **319**, 810–813 (2008).

53. X. Huang and M. A. El-Sayed, "Gold nanoparticles: Optical properties and implementations in cancer diagnosis and photothermal therapy," Journal of Advanced Research **1**, 13–28 (2010).

54. D. Damania, H. K. Roy, H. Subramanian, D. S. Weinberg, D. K. Rex, M. J. Goldberg, J. Muldoon, L. Cherkezyan, Y. Zhu, L. K. Bianchi, D. Shah, P. Pradhan, M. Borkar, H. Lynch, and V. Backman, "Nanocytology of Rectal Colonocytes to Assess Risk of Colon Cancer Based on Field Cancerization," Cancer Res **72**, 2720–2727 (2012).

55. D. P. Slaughter, H. W. Southwick, and W. Smejkal, "“Field cancerization” in oral stratified squamous epithelium. Clinical implications of multicentric origin," Cancer **6**, 963–968 (1953).

56. J. A. O’Shaughnessy, G. J. Kelloff, G. B. Gordon, A. J. Dannenberg, W. K. Hong, C. J. Fabian, C. C. Sigman, M. M. Bertagnolli, S. P. Stratton, S. Lam, W. G. Nelson, F. L. Meyskens, D. S. Alberts, M. Follen, A. K. Rustgi, V. Papadimitrakopoulou, P. T. Scardino, A. F. Gazdar, L. W. Wattenberg, M. B. Sporn, W. A. Sakr, S. M. Lippman, and D. D. V. Hoff, "Treatment and Prevention of Intraepithelial Neoplasia: An Important Target for Accelerated New Agent Development: Recommendations of the American Association for Cancer Research Task Force on the Treatment and Prevention of Intraepithelial Neoplasia," Clin Cancer Res **8**, 314–346 (2002).

57. L. Wu and X. Qu, "Cancer biomarker detection: recent achievements and challenges," Chemical Society Reviews **44**, 2963–2997 (2015).

58. P. Adhikari, P. K. B. Nagesh, F. Alharthi, S. C. Chauhan, M. Jaggi, M. M. Yallapu, M. M. Yallapu, P. Pradhan, and P. Pradhan, "Optical detection of the structural properties of tumor tissue generated by xenografting of drug-sensitive and drug-resistant cancer cells using partial wave spectroscopy (PWS)," Biomed. Opt. Express, BOE **10**, 6422–6431 (2019).

59. H. M. Almabadi, P. K. B. Nagesh, P. Sahay, S. Bhandari, E. C. Eckstein, M. Jaggi, S. C. Chauhan, M. M. Yallapu, and P. Pradhan, "Optical study of chemotherapy efficiency in cancer treatment via intracellular structural disorder analysis using partial wave spectroscopy," J Biophotonics **11**, e201800056 (2018).

60. S. Bhandari, P. K. Shukla, H. M. Almabadi, P. Sahay, R. Rao, and P. Pradhan, "Optical study of stress hormone-induced nanoscale structural alteration in brain using partial wave spectroscopic microscopy," Journal of Biophotonics **12**, e201800002 (2019).

61. P. Adhikari, P. K. Shukla, F. Alharthi, B. Regmi, R. Rao, and P. Pradhan, "Optical probing of nanostructural alterations of brain tissues by partial wave spectroscopy in chronic alcoholism," in *Conference on Lasers and Electro-Optics (2020), Paper AM3I.4* (Optical Society of America, 2020), p. AM3I.4.

62. P. Adhikari, M. Hasan, V. Sridhar, D. Roy, and P. Pradhan, "Studying nanoscale structural alterations in cancer cells to evaluate ovarian cancer drug treatment, using transmission electron microscopy imaging," Phys. Biol. **17**, 036005 (2020).

63. P. Adhikari, P. K. Shukla, M. Hasan, F. Alharthi, B. Regmi, R. Rao, and P. Pradhan, "Photonics study of probiotic treatment on brain cells exposed to chronic alcoholism using molecular specific nuclear light localization properties via confocal imaging," arXiv:1912.11777 [physics] (2019).

64. P. Adhikari, P. K. Shukla, R. Rao, and P. Pradhan, "Quantification of light localization properties to study the effect of probiotic on chronic alcoholic brain cells via confocal imaging," in *Imaging, Manipulation, and Analysis of Biomolecules, Cells, and Tissues XIX* (International Society for Optics and Photonics, 2021), Vol. 11647, p. 1164716.

65. M. Takikita, J.-Y. Chung, and S. M. Hewitt, "Tissue microarrays enabling high-throughput molecular pathology," Current Opinion in Biotechnology **18**, 318–325 (2007).

66. L. Bubendorf, A. Nocito, H. Moch, and G. Sauter, "Tissue microarray (TMA) technology: miniaturized pathology archives for high-throughput in situ studies," The Journal of Pathology **195**, 72–79 (2001).

67. P. Adhikari, F. Alharthi, and P. Pradhan, "Partial Wave Spectroscopy Detection of Cancer Stages using Tissue Microarrays (TMA) Samples," in *Frontiers in Optics + Laser Science APS/DLS (2019), Paper JW4A.89* (Optical Society of America, 2019), p. JW4A.89.

68. B. Sengupta, P. Adhikari, E. Mallet, R. Havner, and P. Pradhan, "Spectroscopic Study on Pseudomonas Aeruginosa Biofilm in the Presence of the Aptamer-DNA Scaffolded Silver Nanoclusters," Molecules **25**, 3631 (2020).

69. G. Sauter, R. Simon, and K. Hillan, "Tissue microarrays in drug discovery," Nature Reviews Drug Discovery **2**, 962–972 (2003).

70. A. McGuigan, P. Kelly, R. C. Turkington, C. Jones, H. G. Coleman, and R. S. McCain, "Pancreatic cancer: A review of clinical diagnosis, epidemiology, treatment and outcomes," World J Gastroenterol **24**, 4846–4861 (2018).

71. Y.-S. Sun, Z. Zhao, Z.-N. Yang, F. Xu, H.-J. Lu, Z.-Y. Zhu, W. Shi, J. Jiang, P.-P. Yao, and H.-P. Zhu, "Risk Factors and Preventions of Breast Cancer," Int J Biol Sci **13**, 1387–1397 (2017).

72. E. J. Kuipers, T. Rösch, and M. Bretthauer, "Colorectal cancer screening—optimizing current strategies and new directions," Nature Reviews Clinical Oncology **10**, 130–142 (2013).

73. S. Killeen, M. Mannion, A. Devaney, and D. C. Winter, "Complete mesocolic resection and extended lymphadenectomy for colon cancer: a systematic review," Colorectal Disease **16**, 577–594 (2014).

74. J. Cuzick, M. A. Thorat, G. Andriole, O. W. Brawley, P. H. Brown, Z. Culig, R. A. Eeles, L. G. Ford, F. C. Hamdy, L. Holmberg, D. Ilic, T. J. Key, C. L. Vecchia, H. Lilja, M. Marberger, F. L. Meyskens, L. M. Minasian, C. Parker, H. L. Parnes, S. Perner, H. Rittenhouse, J. Schalken, H.-P. Schmid, B. J. Schmitz-Dräger, F. H. Schröder, A. Stenzl, B. Tombal, T. J. Wilt, and A. Wolk, "Prevention and early detection of prostate cancer," The Lancet Oncology **15**, e484–e492 (2014).

75. M. S. Litwin and H.-J. Tan, "The Diagnosis and Treatment of Prostate Cancer: A Review," JAMA **317**, 2532–2542 (2017).

76. P. Adhikari, A. P. Binu, S. Bhandari, S. Khan, M. Jaggi, S. C. Chauhan, and P. Pradhan, "Optical detection of fractal dimensions of MUC13 stained pancreatic tissues for cancer diagnostics," arXiv:1812.10883 [physics] (2018).

77. S. Bhandari, S. Choudannavar, E. R. Avery, P. Sahay, and P. Pradhan, "Detection of colon cancer stages via fractal dimension analysis of optical transmission imaging of tissue microarrays (TMA)," Biomed. Phys. Eng. Express **4**, 065020 (2018).

78. P. Wang, R. K. Bista, W. E. Khalbuss, W. Qiu, S. Uttam, K. Staton, L. Zhang, T. A. Brentnall, R. E. Brand, and Y. Liu, "Nanoscale nuclear architecture for cancer diagnosis beyond pathology via spatial-domain low-coherence quantitative phase microscopy," J Biomed Opt **15**, 066028 (2010).

79. J. A. Nickerson, "Nuclear dreams: The malignant alteration of nuclear architecture," Journal of Cellular Biochemistry **70**, 172–180 (1998).

80. D. Zink, A. H. Fischer, and J. A. Nickerson, "Nuclear structure in cancer cells," Nat Rev Cancer **4**, 677–687 (2004).

81. B. R. Konety and R. H. Getzenberg, "Nuclear structural proteins as biomarkers of cancer," Journal of Cellular Biochemistry **75**, 183–191 (1999).

82. D. Damania, H. Subramanian, A. K. Tiwari, Y. Stypula, D. Kunte, P. Pradhan, H. K. Roy, and V. Backman, "Role of cytoskeleton in controlling the disorder strength of cellular nanoscale architecture," Biophys. J. **99**, 989–996 (2010).

83. P. Sahay, A. Ganju, H. M. Almabadi, H. M. Ghimire, M. M. Yallapu, O. Skalli, M. Jaggi, S. C. Chauhan, and P. Pradhan, "Quantification of photonic localization properties of targeted nuclear mass density variations: Application in cancer-stage detection," Journal of Biophotonics **11**, e201700257 (2018).

84. Freeman, Tami, "Photonic technique eases cancer staging," https://physicsworld.com/a/photonic-technique-eases-cancer-staging/.

85. B. Nijboer, "How to Reduce Stress at the Nanoscale Level," https://www.advancedsciencenews.com/how-to-reduce-stress-at-the-nanoscale-level/.

86. J. S. de Bono, S. Oudard, M. Ozguroglu, S. Hansen, J.-P. Machiels, I. Kocak, G. Gravis, I. Bodrogi, M. J. Mackenzie, L. Shen, M. Roessner, S. Gupta, A. O. Sartor, and TROPIC Investigators, "Prednisone plus cabazitaxel or mitoxantrone for metastatic castration-resistant prostate cancer progressing after docetaxel treatment: a randomised open-label trial," Lancet **376**, 1147–1154 (2010).

87. I. F. Tannock, D. Osoba, M. R. Stockler, D. S. Ernst, A. J. Neville, M. J. Moore, G. R. Armitage, J. J. Wilson, P. M. Venner, C. M. Coppin, and K. C. Murphy, "Chemotherapy with mitoxantrone plus prednisone or prednisone alone for symptomatic hormone-resistant prostate cancer: a Canadian randomized trial with palliative end points.," JCO **14**, 1756–1764 (1996).

88. A. Yagoda and D. Petrylak, "Cytotoxic chemotherapy for advanced hormone-resistant prostate cancer," Cancer **71**, 1098–1109 (1993).

89. J.-P. Gillet, A. M. Calcagno, S. Varma, M. Marino, L. J. Green, M. I. Vora, C. Patel, J. N. Orina, T. A. Eliseeva, V. Singal, R. Padmanabhan, B. Davidson, R. Ganapathi, A. K. Sood, B. R. Rueda, S. V. Ambudkar, and M. M. Gottesman, "Redefining the relevance of established cancer cell lines to the study of mechanisms of clinical anti-cancer drug resistance," PNAS **108**, 18708–18713 (2011).

90. S. Sumanasuriya and J. D. Bono, "Treatment of Advanced Prostate Cancer—A Review of Current Therapies and Future Promise," Cold Spring Harb Perspect Med **8**, a030635 (2018).

91. C. L. Morton and P. J. Houghton, "Establishment of human tumor xenografts in immunodeficient mice," Nat Protoc **2**, 247–250 (2007).

92. Y. Ma, Z. Lin, J. K. Fallon, Q. Zhao, D. Liu, Y. Wang, and F. Liu, "New mouse xenograft model modulated by tumor-associated fibroblasts for human multi-drug resistance in cancer," Oncology Reports **34**, 2699–2705 (2015).

93. W. M. van Weerden and J. C. Romijn, "Use of nude mouse xenograft models in prostate cancer research," The Prostate **43**, 263–271 (2000).

94. B. N. P. Kumar, N. Puvvada, S. Rajput, S. Sarkar, S. K. Das, L. Emdad, D. Sarkar, P. Venkatesan, I. Pal, G. Dey, S. Konar, K. R. Brunt, R. R. Rao, A. Mazumdar, S. C. Kundu, A. Pathak, P. B. Fisher, and M. Mandal, "Sequential release of drugs from hollow manganese ferrite nanocarriers for breast cancer therapy," J. Mater. Chem. B **3**, 90–101 (2014).

95. G. Housman, S. Byler, S. Heerboth, K. Lapinska, M. Longacre, N. Snyder, and S. Sarkar, "Drug resistance in cancer: an overview," Cancers (Basel) **6**, 1769–1792 (2014).

96. M. Michael and M. m. Doherty, "Tumoral Drug Metabolism: Overview and Its Implications for Cancer Therapy," JCO **23**, 205–229 (2005).

97. W. Zhang, Y. Meng, N. Liu, X.-F. Wen, and T. Yang, "Insights into Chemoresistance of Prostate Cancer," Int. J. Biol. Sci. **11**, 1160–1170 (2015).

98. A. Persidis, "Cancer multidrug resistance," Nat Biotechnol **17**, 94–95 (1999).

99. L. Mashouri, H. Yousefi, A. R. Aref, A. mohammad Ahadi, F. Molaei, and S. K. Alahari, "Exosomes: composition, biogenesis, and mechanisms in cancer metastasis and drug resistance," Mol Cancer **18**, 75 (2019).

100. M. Hasan, P. K. Shukla, P. K. Shukla, S. Nanda, P. Adhikari, R. Rao, P. Pradhan, and P. Pradhan, "Photonic probing of structural alterations in DNA specific mass density fluctuations in nuclei due to total body irradiation (TBI) via confocal imaging," OSA Continuum, OSAC **4**, 569–578 (2021).

101. P. Adhikari and P. Pradhan, "Optical detection of cancer stages via partial wave spectroscopy (PWS) using tissue microarrays (TMA) samples," arXiv:2012.14194 [physics] (2020).

102. P. Adhikari, P. K. Shukla, S. Bhandari, A. S. Meena, B. Regmi, F. Alharthi, P. Sahay, R. Rao, and P. Pradhan, "Optical probing of pups brain tissue and molecular specific nuclear nano-structural alterations due to fetal alcoholism via dual spectroscopic approach," arXiv:1912.11593 [physics] (2019).

103. S. Leclercq, P. D. Cani, A. M. Neyrinck, P. Stärkel, F. Jamar, M. Mikolajczak, N. M. Delzenne, and P. de Timary, "Role of intestinal permeability and inflammation in the biological and behavioral control of alcohol-dependent subjects," Brain Behav Immun **26**, 911–918 (2012).

104. A. Rodriguez-Gonzalez and L. Orio, "Microbiota and Alcohol Use Disorder: Are Psychobiotics a Novel Therapeutic Strategy?," Curr Pharm Des **26**, 2426–2437 (2020).

105. M. A. Ron, "Brain damage in chronic alcoholism: a neuropathological, neuroradiological and psychological review," Psychological Medicine **7**, 103–112 (1977).

106. C. Harper and I. Matsumoto, "Ethanol and brain damage," Curr Opin Pharmacol **5**, 73–78 (2005).

107. A. Topiwala and K. P. Ebmeier, "Effects of drinking on late-life brain and cognition," Evidence-Based Mental Health **21**, 12–15 (2018).

108. R. D. Fields, A. Araque, H. Johansen-Berg, S.-S. Lim, G. Lynch, K.-A. Nave, M. Nedergaard, R. Perez, T. Sejnowski, and H. Wake, "Glial Biology in Learning and Cognition," Neuroscientist **20**, 426–431 (2014).

109. S. Hunot and E. C. Hirsch, "Neuroinflammatory processes in Parkinson's disease," Annals of Neurology **53**, S49–S60 (2003).

110. S.-M. Lucas, N. J. Rothwell, and R. M. Gibson, "The role of inflammation in CNS injury and disease," British Journal of Pharmacology **147**, S232–S240 (2006).

111. B. J. Crenshaw, S. Kumar, C. R. Bell, L. B. Jones, S. D. Williams, S. N. Saldanha, S. Joshi, R. Sahu, B. Sims, and Q. L. Matthews, "Alcohol Modulates the Biogenesis and Composition of Microglia-Derived Exosomes," Biology **8**, 25 (2019).

112. C. Park, E. Brietzke, J. D. Rosenblat, N. Musial, H. Zuckerman, R.-M. Ragguett, Z. Pan, C. Rong, D. Fus, and R. S. McIntyre, "Probiotics for the treatment of depressive symptoms: An anti-inflammatory mechanism?," Brain, Behavior, and Immunity **73**, 115–124 (2018).

113. L. Desbonnet, L. Garrett, G. Clarke, J. Bienenstock, and T. G. Dinan, "The probiotic Bifidobacteria infantis: An assessment of potential antidepressant properties in the rat," Journal of Psychiatric Research **43**, 164–174 (2008).

114. P. K. Shukla, A. S. Meena, and R. Rao, "Prevention and mitigation of alcohol-induced neuroinflammation by Lactobacillus plantarum by an EGF receptor-dependent mechanism," Nutritional Neuroscience **0**, 1–13 (2020).

115. P. K. Shukla, A. S. Meena, B. Manda, M. Gomes-Solecki, P. Dietrich, I. Dragatsis, and R. Rao, "Lactobacillus plantarum prevents and mitigates alcohol-induced disruption of colonic epithelial tight junctions, endotoxemia, and liver damage by an EGF receptor-dependent mechanism," FASEB J fj201800351R (2018).

116. J. Beuthan, O. Minet, J. Helfmann, M. Herrig, and G. Müller, "The spatial variation of the refractive index in biological cells," Phys Med Biol **41**, 369–382 (1996).

117. P. Pradhan, D. Damania, H. M. Joshi, V. Turzhitsky, H. Subramanian, H. K. Roy, A. Taflove, V. P. Dravid, and V. Backman, "Quantification of nanoscale density fluctuations using electron microscopy: Light-localization properties of biological cells," Appl. Phys. Lett. **97**, 243704 (2010).

118. E. Abrahams, P. W. Anderson, D. C. Licciardello, and T. V. Ramakrishnan, "Scaling Theory of Localization: Absence of Quantum Diffusion in Two Dimensions," Phys. Rev. Lett. **42**, 673–676 (1979).

119. M. Sidoryk-Wegrzynowicz, M. Wegrzynowicz, E. Lee, A. B. Bowman, and M. Aschner, "Role of Astrocytes in Brain Function and Disease," Toxicol Pathol **39**, 115–123 (2011).

120. M. Aschner, U. Sonnewald, and K. H. Tan, "Astrocyte Modulation of Neurotoxic Injury," Brain Pathology **12**, 475–481 (2002).

121. F. Aloisi, "Immune function of microglia," Glia **36**, 165–179 (2001).

122. K. Suk, "Microglial signal transduction as a target of alcohol action in the brain," Curr Neurovasc Res **4**, 131–142 (2007).

123. C. Dulac, "Brain function and chromatin plasticity," Nature **465**, 728–735 (2010).

124. D. Damania, H. K. Roy, D. Kunte, J. A. Hurteau, H. Subramanian, L. Cherkezyan, N. Krosnjar, M. Shah, and V. Backman, "Insights into the field carcinogenesis of ovarian cancer based on the nanocytology of endocervical and endometrial epithelial cells," International Journal of Cancer **133**, 1143–1152 (2013).

125. J. E. Chandler, Y. Stypula-Cyrus, L. Almassalha, G. Bauer, L. Bowen, H. Subramanian, I. Szleifer, and V. Backman, "Colocalization of cellular nanostructure using confocal fluorescence and partial wave spectroscopy," Journal of Biophotonics **10**, 377–384 (2017).

126. G. M. Bauer, Y. Stypula-Cyrus, H. Subramanian, L. Cherkezyan, P. Viswanathan, D. Zhang, R. Iyengar, S. Bagalkar, J. Derbas, T. Graff, S. Gladstein, L. M. Almassalha, J. E. Chandler, H. K. Roy, and V. Backman, "The transformation of the nuclear nanoarchitecture in human field carcinogenesis," Future Science OA **3**, FSO206 (2017).

127. P. Sahay, P. K. Shukla, H. M. Ghimire, H. M. Almabadi, V. Tripathi, S. K. Mohanty, R. Rao, and P. Pradhan, "Quantitative analysis of nanoscale intranuclear structural alterations in hippocampal cells in chronic alcoholism via transmission electron microscopy imaging," Phys Biol **14**, 026001 (2017).

128. H. M. Ghimire, P. Shukla, P. Sahay, H. Almabadi, V. Tripathi, O. Skalli, R. K. Rao, and P. Pradhan, "Nanoscale intracellular mass-density alteration as a signature of the effect of alcohol on early carcinogenesis: A transmission electron microscopy (TEM) study," arXiv:1512.08593 [physics] (2015).

129. L. A. Torre, B. Trabert, C. E. DeSantis, K. D. Miller, G. Samimi, C. D. Runowicz, M. M. Gaudet, A. Jemal, and R. L. Siegel, "Ovarian cancer statistics, 2018," CA: A Cancer Journal for Clinicians **68**, 284–296 (2018).

130. L. Galluzzi, L. Senovilla, I. Vitale, J. Michels, I. Martins, O. Kepp, M. Castedo, and G. Kroemer, "Molecular mechanisms of cisplatin resistance," Oncogene **31**, 1869–1883 (2012).

131. R. B. Richardson, "p53 mutations associated with aging-related rise in cancer incidence rates," Cell Cycle **12**, 2468–2478 (2013).

132. S.-S. Li, J. Ma, and A. S. T. Wong, "Chemoresistance in ovarian cancer: exploiting cancer stem cell metabolism," Journal of Gynecologic Oncology **29**, (2017).

133. J. Staub, J. Chien, Y. Pan, X. Qian, K. Narita, G. Aletti, M. Scheerer, L. R. Roberts, J. Molina, and V. Shridhar, "Epigenetic silencing of HSulf-1 in ovarian cancer:implications in chemoresistance," Oncogene **26**, 4969–4978 (2007).

134. D. Roy, S. Mondal, C. Wang, X. He, A. Khurana, S. Giri, R. Hoffmann, D.-B. Jung, S. H. Kim, E. N. Chini, J. C. Periera, C. D. Folmes, A. Mariani, S. C. Dowdy, J. N. Bakkum-Gamez, S. M. Riska, A. L. Oberg, E. D. Karoly, L. N. Bell, J. Chien, and V. Shridhar, "Loss of HSulf-1 promotes altered lipid metabolism in ovarian cancer," Cancer & Metabolism **2**, 13 (2014).

135. D. Roy, S. Mondal, A. Khurana, D.-B. Jung, R. Hoffmann, X. He, E. Kalogera, T. Dierks, E. Hammond, K. Dredge, and V. Shridhar, "Loss of HSulf-1: The Missing Link between Autophagy and Lipid Droplets in Ovarian Cancer," Sci Rep **7**, 1–13 (2017).

136. B. Huang, M. Bates, and X. Zhuang, "Super-Resolution Fluorescence Microscopy," Annu. Rev. Biochem. **78**, 993–1016 (2009).

137. M. V. Sednev, V. N. Belov, and S. W. Hell, "Fluorescent dyes with large Stokes shifts for super-resolution optical microscopy of biological objects: a review," Methods Appl. Fluoresc. **3**, 042004 (2015).

138. A. Szczurek, L. Klewes, J. Xing, A. Gourram, U. Birk, H. Knecht, J. W. Dobrucki, S. Mai, and C. Cremer, "Imaging chromatin nanostructure with binding-activated localization microscopy based on DNA structure fluctuations," Nucleic Acids Res **45**, e56–e56 (2017).

APPENDIX A

COPYRIGHT PERMISSION FROM THE PUBLISHERS TO REUSE THE CONTENTS IN THE DISSERTATION

A.1 Copy right permission from OSA

Dear Prakash Adhikari,

Thank you for contacting The Optical Society (OSA).
For the use of material from Prakash Adhikari, Prashanth K. B. Nagesh, Fatemah Alharthi, Subhash C. Chauhan, Meena Jaggi, Murali M. Yallapu, and Prabhakar Pradhan, "Optical detection of the structural properties of tumor tissue generated by xenografting of drug-sensitive and drug-resistant cancer cells using partial wave spectroscopy (PWS)," Biomed. Opt. Express 10, 6422-6431 (2019):

> Because you are the author of the source paper from which you wish to reproduce material, OSA considers your requested use of its copyrighted materials to be permissible within the author rights granted in the Copyright Transfer Agreement submitted by the requester on acceptance for publication of his/her manuscript. It is requested that a complete citation of the original material be included in any publication. This permission assumes that the material was not reproduced from another source when published in the original publication.
>
> If the entire article is being included, it is permissible to use the **version of record**.

While your publisher should be able to provide additional guidance, OSA prefers the below citation formats:

> For citations in figure captions:
>
> [Reprinted/Adapted] with permission from [ref #] © The Optical Society. (Please include the full citation in your reference list)
>
> For images without captions:
>
> Journal Vol. #, first page (year published) An example: Opt. Express 19, 2720 (2011)

Please let me know if you have any questions.

Kind Regards,
Hannah Greenwood

Hannah Greenwood
April 26, 2021

Authorized Agent, The Optical Society

The Optical Society (OSA)
2010 Massachusetts Ave., NW
Washington, DC 20036 USA
www.osa.org

A.2 Copy right permission from IOP

Dear Prakash Adhikari,

Thank you for your email and for taking the time to seek this permission.

When you transferred the copyright in your article to IOP, we granted back to you certain rights, including the right to include all or part of the Final Published Version of the article within any thesis or dissertation. Please note you may need to obtain separate permission for any third-party content you included within your article.

Please include citation details, "© IOP Publishing. Reproduced with permission. All rights reserved" and for online use, a link to the Version of Record.

The only restriction is that if, at a later date, you wanted your thesis/dissertation to be published commercially or made publicly available, further permission would be required.

I wish you the best of luck with the completion of your thesis/dissertation.

Kind regards,

Sophie
Copyright & Permissions Team
Sophie Brittain - Rights & Permissions Assistant
Cameron Wood - Legal & Rights Adviser

Contact Details

E-mail: permissions@ioppublishing.org

For further information about copyright and how to request permission: https://publishingsupport.iopscience.iop.org/copyright-journals/

See also: https://publishingsupport.iopscience.iop.org/

Please see our Author Rights Policy https://publishingsupport.iopscience.iop.org/author-rights-policies/

Please note: We do not provide signed permission forms as a separate attachment. Please print this email and provide it to your publisher as proof of permission. **Please note**: Any statements made by IOP Publishing to the effect that authors do not need to get permission to use any content where IOP Publishing is not the publisher is not intended to constitute any sort of legal advice. Authors must make their own decisions as to the suitability of the content they are using and whether they require permission for it to be published within their article.

APPENDIX B

MATLAB CODE FOR CALCULATION OF THE DEGREE OF THE DISORDER STRENGTH FOR PWS AND IPR TECHNIQUES

B.1 PWS program to calculate disorder strength (L_d)

```
clear all
x_max=1460; %maximum pixel cover in x-axis
y_max=1920; %maximum pixel cover in y-axis
fname = 'Name_of_file';
info = imfinfo(fname);
num_images = numel(info);
for k = 1:num_images % total number of wavelength cover
     A = imread(fname, k, 'Info', info);
     for j=1:y_max
    B(1:x_max,j,k)=A(1:x_max,j); % xyz matric with x,y pixel size of
camera and z wavelength
    k %[k j] %[k,i,j, A(j,i)];
     end
end

for i=1:1460
for j=1:1920
      kmin=1;
      kmax=150;
      xBB=kmin:kmax;
      yBB1=BB(i,j,kmin:kmax);
      yBB2=squeeze(yBB1);
      yBB4=yBB2';

     [b,a] = butter(15,0.5);  % 6th order polynomial
     yBB=filter(b,a,yBB4);   % finally extracted reflection data

      yBB=double(yBB4);
      pfBB=polyfit(xBB,yBB,3);
      yfBB=polyval(pfBB,xBB);
      s1=yBB-yfBB;
      s_srt=sort(s1);
      s_up= mean(s_srt(1:7));
      s2=s1+ abs(s_up);
       %s2=s1; %
      %s2=s1+ pfBB(1) + 0.000001;
      %s2=s1./max(s1);
      %s2=(smooth(s2))';

      BBrms(i,j)=rms(s2);

      qmin=kmin+500; % Starting wavelength to cover in nm
```

```
        qmax=kmax+500; % Ending wavelength to cover in nm
        q=qmin:qmax; %wavelength region covered
        kd=(2*pi./q)*1000;  % k vector
        kd1=floor(length(kd)/2); %mid length of wave vector
        kdm=kd(kd1); %mid value of wave vector
        n0=1.38;  %refractive index


        xcr=xcorr(s2);
        y_v=log(xcr(150:154)/xcr(150));
        x_v=(1:5)*0.01915;
        xx_v=x_v.*x_v;
        ck=polyfit(xx_v,y_v,1);
        CKm(i,j)=ck(2);
        % Structural Disorder to be calculated
        LD(i,j) = abs(((n0^2)*rms(s2)*ck(2))/((2*kdm^2)));
end
end
%save DU145_t
figure(401)
subplot(2,2,1)
%imagesc(BB(1:690-400,1:250-100,1))
imagesc(BB(:,:,1))
subplot(2,2,2)
imagesc(BBrms)
subplot(2,2,3)
imagesc((CKm))
subplot(2,2,4)
imagesc(LD)
```

B.2 IPR program to calculate <IPR> using confocal images

```
clear all
t=1;
e=1;
m=4; %sample box size                       % input
n=m*m;
n_i_max=250; %total # of boxes in row       % input
n_j_max=250; %total # of boxes in column    % input
k=0;
nf=250;   % histogram division
for n_az=1:6
    n_ct=0;

if n_az==1
az =imread('name_of_files.tif');      % change the name of the img
*****************
end
if n_az==2
az =imread('d2a.tif');    %input       % change the name of the img
*****************
end
if n_az==3
az =imread('d3a.tif');    %input       % change the name of the img
*****************
end
if n_az==4
az =imread('d4a.tif');    %input       % change the name of the img
*****************
end
if n_az==5
az =imread('d5a.tif');    %input       % change the name of the img
*****************
end
if n_az==6
az =imread('d6a.tif');    %input       % change the name of the img
*****************
end
az = double(az);
az = double(az(1:1000, 1:1000));   % input   (careful about the color)
h2=az(1:1000,1:1000);             % dimension of the image   % input
h1=(255-h2);
for n_i=1:n_i_max
for n_j=1:n_j_max
```

```
[n_az n_ct+1]
k2=0;
for i2=1:m
for j2=1:m
k2=k2+1;
hu(k2)= h1(i2+(n_i-1)*m , j2+(n_j-1)*m);
end
end
hu_sum = sum(hu);
if(hu_sum==0)
    hu_sum=1;
end
hu_N = (hu/hu_sum)*1*length(hu);
hu_N=4*hu_N;                          % amplification factor   % input
for ii=1:n
 d1(ii,ii)=hu_N(ii);
end
for i=1:n
for j=1:n
 a(i,j)=0;
end
end %n
for k=1:n
   a(k,k)=d1(k,k);
end%if
for k=1:n
     if((k-m)>0)
     a(k,k-m)=t;
     a(k-m,k)=t;
      end

      if((k+m)<=n)
     a(k,k+m)=t;
     a(k+m,k)=t;
      end

      if((k-1)>0)
     a(k-1,k)=t;
     a(k,k-1)=t;
      end

      if((k+1)<=n)
     a(k+1,k)=t;
     a(k,k+1)=t;
      end
```

```
end %k

[v,d]=eig(a);
ipr_egfr(1,1:n) = sum(v.^4);
[n1,x1]=hist(ipr_egfr*n,nf);
%[n2,x2]=hist(ipr_ht29*n,nf);
%[n3,x3]=hist(ipr_csk*n,nf);
n1_s=sum(n1*(x1(4)-x1(3)));
n1=n1/n1_s;
%n2_s=sum(n2*(x2(4)-x2(3)));
%n2=n2/n2_s;
%n3_s=sum(n3*(x3(4)-x3(3)));
%n3=n3/n3_s;
x1av = sum(n1.*x1*(x1(4)-x1(3)));
%x2av = sum(n2.*x2*(x2(4)-x2(3)))
%x3av = sum(n3.*x3*(x3(4)-x3(3)))
 %figure(2)
 %plot(x1,n1,'-*b')%, x2,n2,'-*m',x3,n3,'-*r')
% axis([ 1.5 5 0 1000])
n_ct=n_ct+1;
d_sline(n_ct)=x1av;            % all ipr values in one array
d_ipr(n_i,n_j)=x1av;           % ipr matrix
[nn,xx]=hist(d_sline,200);
%n_ct
end
end
figure(100+n_az)
subplot(2,2,1)
imagesc(h1);
colormap(gray);
subplot(2,2,2)
imagesc(d_ipr);
colormap(jet);
subplot(2,2,3)
hist(d_sline,200);
subplot(2,2,4)
plot(xx,nn);
if n_az==1
save name_of_files.dat d_sline -ascii       % input saved file
**************************
end
if n_az==2
save d2a.dat d_sline -ascii       % input saved file
**************************
```

```
end
if n_az==3
save d3a.dat d_sline -ascii       % input saved file
**************************
end
if n_az==4
save d4a.dat d_sline -ascii       % input saved file
**************************
end
if n_az==5
save d5a.dat d_sline -ascii       % input saved file
**************************
end
if n_az==6
save d6a.dat d_sline -ascii       % input saved file
**************************
end
figure, imagesc(d_ipr); colormap(jet)
end
```

B.3 IPR program to calculate <IPR> using TEM images

```
clear all
n_sample=1;
m=20; %number of grids
n_ij_max=148; %(1000/40)
n_ct=0;
t=1;
e=1;
n=m*m;
k=0;
nf=250;
%amp=3; %smplificstion modified
for n_az=1:n_sample

if n_az==1
az =imread('name_of_file.tif');
end
% if n_az==2
% az=imread('control_11.tif');
% end
% if n_az==3
% az=imread('control_16.tif');
```

```
% end
% if n_az==4
% az=imread('control_18.tif');
% end
% if n_az==5
% az=imread('5.tif');
% end
az =double(az);
h1=az;
for n_i=1:n_ij_max
 for n_j=1:n_ij_max

[n_az n_ct+1]
k2=0;
for i2=1:m
for j2=1:m
k2=k2+1;
hu(k2)= h1(i2+(n_i-1)*m , j2+(n_j-1)*m);
end
end
hu_sum = sum(hu);
if(hu_sum==0)
    hu_sum=1
end
hu_N = (hu/hu_sum)*1*length(hu);
for ii=1:n
 d1(ii,ii)=hu_N(ii);
end
for i=1:n
for j=1:n
 a(i,j)=0;
end
end %n
for k=1:n
    a(k,k)=d1(k,k);
    %a(k,k)=amp*d1(k,k); % amplification modified
end%if
for k=1:n
     if((k-m)>0)
     a(k,k-m)=t;
     a(k-m,k)=t;
      end

      if((k+m)<=n)
     a(k,k+m)=t;
```

```
     a(k+m,k)=t;
      end

      if((k-1)>0)
     a(k-1,k)=t;
     a(k,k-1)=t;
      end

      if((k+1)<=n)
     a(k+1,k)=t;
     a(k,k+1)=t;
      end
end %k

[v,d]=eig(a);
ipr_egfr(n_az,:) = sum(v.^4);
[n1,x1]=hist(ipr_egfr*n,nf);
%[n2,x2]=hist(ipr_ht29*n,nf);
%[n3,x3]=hist(ipr_csk*n,nf);
n1_s=sum(n1*(x1(4)-x1(3)));
n1=n1/n1_s;
%n2_s=sum(n2*(x2(4)-x2(3)));
%n2=n2/n2_s;
x1av = sum(n1.*x1*(x1(4)-x1(3)));
%x2av = sum(n2.*x2*(x2(4)-x2(3)))
n_ct=n_ct+1;
d_sline(n_ct)=x1av;
d_ipr(n_i,n_j)=x1av;
%n_ct
end
end

end
save c1a
save c1a.dat d_sline -ascii
figure(101), hist(d_sline,nf);
figure(102), imagesc(d_ipr);
```